METAL AND METALOXIDE NANOSTRUCTURES ON AND IN PLANT VIRUSES

THÈSE N^O 3620 (2006)

PRÉSENTÉE LE 12 OCTOBRE 2006

À LA FACULTÉ DES SCIENCES DES BASE

Laboratoire de science à l'échelle nanométrique

PROGRAMME DOCTORAL EN PHYSIQUE

ÉCOLE POLYTECHNIQUE FÉDÉRALE DE LAUSANNE

POUR L'OBTENTION DU GRADE DE DOCTEUR ÈS SCIENCES

PAR

Sinan BALCI

M.Sc. in Chemistry, Bilkent University, Ankara, Turquie
de nationalité turque

acceptée sur proposition du jury:

Prof. R. Schaller, président du jury
Prof. K. Kern, directeur de thèse
Prof. G. Dietler, rapporteur
Prof. R. Spolenak, rapporteur
Dr A. Bittner, rapporteur

EPFL

ÉCOLE POLYTECHNIQUE
FÉDÉRALE DE LAUSANNE

Suisse
2006

Abstract

Tobacco Mosaic Virus (TMV) is composed of 2130 identical coat protein subunits following the right-handed helix of an accompanying RNA strand to produce a 300 nm hollow cylinder with an outer diameter of 18 nm and a 4 nm wide central channel. In this work, TMV is used as a bionanotemplate for the synthesis of interesting nanomaterials. When the TMV is activated with a catalyst (Pd (II)), nickel, copper, and cobalt nanowires can be grown within the central channel of the virion. In the same way alloy nanowires (cobalt-iron) are produced inside the central channel. Due to the non-galvanic protocol, the deposition method is called electroless deposition (ELD). Apart from the deposition of metals (Ni, Co, Cu, CoFe alloy), zinc oxide, a large band gap semiconductor, is deposited on the exterior surface of the virus. The chemical compositions of the nanomaterials are revealed at the nanoscale by energy-filtering transmission electron microscopy.

Various physical properties of some of the synthesized nanomaterials are measured: Electrical transport measurements on the TMV rods, contacted by gold electrodes, indicate that the TMV rods show insulating behavior at room temperature. High-resolution transmission electron microscopy images of individual nickel nanowires show the crystalline bulk phase, confined to a 3 nm wide wire, with (111) planes perpendicular to the wire axis. Cathodoluminescence measurements from individual zinc oxide rods exhibit ultraviolet emission with a photon energy of around ~3.4 eV, which is equal to the band gap of the bulk material. Furthermore, 6 nm diameter gold nanoparticles (Au-nps) are selectively attached to the ends of the TMV particles, and they are enlarged by

electroless deposition of gold. The RNA strand plays an important role in the selective attachment of the Au-nps.

It is possible to print and align TMV particles on a variety of surfaces by the microcontact printing method. Several micrometer long end-to-end assembled TMV rods can be placed close to the edges within the recessed regions of polydimethysiloxane stamp structures. The reason for the selective assembly of the virions is the dewetting of the inking solvent (water) on the stamp surface. By printing, the virion pattern is transferred to solid surfaces. Alternatively, TMV particles can be selectively assembled on flat rectangular submicrometer patches with amine groups, which are generated by electron beam lithography.

The experimental results show that TMV can be a model system for new bionanotemplates with huge potential in nanoscale science and possibly technology.

Zusammenfassung

Das Tabakmosaikvirus (TMV) besteht aus 2130 identischen Hüllproteineinheiten, die helikal um eine rechtshändige RNA-Helix angeordnet sind. Das Virus ist demnach ein 300 nm langer Hohlzylinder mit einem äußeren Durchmesser von 18 nm und einem 4 nm weiten Innenkanal. In dieser Arbeit wird TMV als Biotemplat für die Synthese einiger interessanter Nanostrukturen verwendet. Wenn TMV mit einem Katalysator wie Pd(II) aktiviert wird, können Nickel-, Kupfer- und Kobalt-Nanodrähte im Innenkanal erzeugt werden. Auf die gleiche Weise können auch Nanodrähte aus Legierungen wie Kobalt-Eisen im Viruspartikel herstellen. Aufgrund der nicht-galvanischen Vorgehenweise wird der Prozes, stromlose Abscheidung genant. Abgesehen von der Abscheidung von Metallen (Ni, Co, Cu, CoFe), wurde auch Zinkoxid, ein Halbleiter mit großer Bandlücke, auf der äußeren Hülle von Virionen erzeugt. Die chemische Zusammensetzung der Materialien wurde im Nanomaßstab mittels energiefilternder Transmissions-Elektronenmikroskopie vermessen.

Unterschiedliche physikalische Eigenschaften der Materialien konnten bestimmt werden: Elektrische Transportmessungen der TMV-Zylinder, die von Goldelektroden kontaktiert wurden, haben gezeigt, dass die Zylinder bei Raumtemperatur isolatoren sind. Hochauflösende Transmissions-Elektronenmikroskopie an einzelnen Nickeldrähten hat gezeigt, dass das Nickel kristallin ist und seine (111)-Flächen senkrecht zur Drahtachse stehen. Kathodolumineszenz-Messungen an einzelnen auf TMV aufgewachsenen Zinkoxid-Stäbchen zeigten Ultraviolett-Emission mit einer Photonenenergie von ~3.4 eV, was im wesentlichen der Bandlücke von ZnO

entspricht. Außerdem wurden Goldcluster von 6 nm Durchmesser selektiv an die Enden der TMV gebunden. Sie könnten durch stromlose Abscheidung von Gold gezielt vergrößert werden. Offenbar spielt die RNA eine entscheidende Rolle bei der selektiven Anbindung der Goldpartikel.

TMV-Partikel können auf eine Reihe von Oberflächen durch die Mikrokontaktdruck-Methode übertragen und auch ausgerichtet werden. Einige Mikrometer lange endständig aggregierte TMV-Zylinder bilden sich an den Kanten der Reliefstruktur eines Polydimethysiloxan-Stempels. Die Ursache der Anordnung und Ausrichtung der Virionen liegt in Entnetzungsvorgängen des Wassers auf der Stempeloberfläche. Die Anordnung der Virionen findet sich auch nach der Übertragung (Stempeln) auf den festen Oberflächen. Es ist ebenfalls möglich, TMV-Partikel selektiv auf flachen, rechteckigen, amin-terminierten Bereichen zu adsorbieren, welche durch Elektronenstrahl-Lithographie hergestellt werden.

Die experimentellen Resultate zeigen deutlich, dass TMV ein Modellsystem für neuartige Bionanotemplate sein kann, die ein hohes Potenzial in der Nanoforschung und möglicherweise auch Nanotechnologie haben.

Schlüsselbegriffe: Tabakmosaikvirus, stromlose Abscheidung, Nanodrähten, Egergiefilterungs-Tranmissionselektronenmikroskopie, Mikrokontaktdruck.

Contents

CHAPTER 1

Introduction

Nanotechnology aims to manipulate and control materials at the nanometer level (1-100 nm). The possibility of generating chemical functionality in the nanometer range (nanochemistry) is necessary for applications in the fields of future electronic devices and high-density data storage (nanoelectronics and photonics). For example, the size of features on integrated circuits has rapidly decreased due to the improvements of materials for the optical lithographic structuring (top-down approach), and also analytical techniques. However, fabrication of structures with feature sizes below 100 nm by optical patterning techniques remains problematic. This is mainly due to the ambient absorption of ultraviolet radiation by the materials and the expensive instrumentation required. An alternative to the top-down approach is a so-called bottom-up approach, based on enlarging small structures in controlled ways such as self-assembly of subunits [Whitesides91]. Using this approach, very small nanostructures (<10 nm) can be fabricated, which otherwise are difficult or impossible to obtain by using other means.

The research described in this thesis is focused on the mineralization of tobacco mosaic virus (TMV), characterization of the synthesized nanomaterials, printing and alignment of TMV, and measurement of the interesting physical properties of the synthesized nanomaterials. The first part of the thesis is focused on the synthesis of a variety of metal nanostructures using the method of

electroless deposition (ELD). After mineralization of the TMV particles with a suitable route, a variety of nanomaterials are synthesized within the central channel, on the outer surface as well as at the ends of the TMV particles. Besides that, chemical compositions of the mineralized virions are analyzed on the nanometer scale using energy-filtering transmission electron microscopy (EFTEM). The second part of the thesis describes the zinc oxide (metal oxide) nanostructures after mineralization of TMV. Chemical composition of the metal oxide deposited on the outer surface of the TMV is explored. Moreover, cathodeluminescence from the synthesized zinc oxide rods is presented. In the last part of the thesis, by using microcontact-printing method, it is shown that TMV particles can be organized on various surfaces, for example on polymers, silicon oxide, and mica surfaces. Here, an important aspect is the combination of top-down organization and bottom-up self-assembly of the TMV (by dewetting), which results in nanostructures created by microscale polymer structures.

In nature, several organisms employ many constructs in the nanoscale. The rapidly growing field of nanotechnology tries to mimic the information-handling, materials-building, and responsive-sensing capabilities of biological systems at the nanometer scale. A prospective bottom-up approach involves the use of biological molecules as templates for arranging and synthesizing nanomaterials. Rod- or tube-like biological molecules such as DNA [Mertig02], tobacco mosaic virus (TMV) [Knez04,Shenton99], bacteriophages [Mao04], microtubules [Mertig98] are well defined in their chemical composition and structure. Such molecules are used as templates for the nucleation of nanoscale inorganic structures. For instance, Keren and co-workers have demonstrated a new type of lithographic technique for growing molecular scale electronic devices with DNA molecules as templates [Keren02]. By sequence-specific molecular-lithography, metal coatings, at the chosen locations on the strands of DNA, can be placed [Keren02]. This technique uses the RecA protein as a protecting resist like polymethylmetacrylate (PMMA), which is used in electron beam lithography processes. Another attractive template for the synthesis and organization of nanomaterials is TMV, which has a length of 300 nm and a diameter of 18 nm with an inner channel of 4 nm. This

dimension makes the virus a very attractive template for the synthesis and organization of nanomaterials [Knez04]. A pioneering work, published in 1939 by Kausche and co-workers, showed that gold colloids (nanoparticles) could be deposited on the external surface of TMV particles [Kausche39]; however, the aim was certainly not the synthesis of new nanomaterials, but rather understanding how the gold particles were arranged to yield the characteristic red color used for the detection of viruses and other pathogens. 60 years later, after 1999, several research groups have used TMV as a template for the synthesis of various nanomaterials such as nanowires and nanoparticles [Shenton99,Knez04,Dujardin03]. Recently, chemical modification of the TMV has been achieved, which is expected to increase its use in the synthesis of nanomaterials and other applications in nanoscience [Schlick05]. Besides that genetic modifications can have a good impact on the nanomaterials synthesis. Lee and co-workers claimed that they improved metal cluster deposition on the outer surface of mutated virions (cysteine residues -thiol group containing amino acid- on the outer surface of the virion) [Lee05].

The chemical composition of nanomaterials can be revealed with several techniques such as energy-filtering transmission electron microscopy (EFTEM) and energy dispersive X-ray (EDX) [Williams96]. EFTEM and EDX are complementary techniques, in which EFTEM is very sensitive for chemical analysis of low atomic number elements and EDX is very sensitive for elements with heavier atomic weight. EFTEM uses the spectroscopic information provided by the energy-loss spectrum of the materials in a spatially resolved manner in order to obtain elemental maps, which elucidate the spatial (lateral) distribution of any feature in the electron-energy loss spectrum. The method uses the characteristic inner-shell energy-loss edges of the elements for mapping the elemental distribution over very small areas. EFTEM is an ideal tool to study the chemical composition of nanoscale materials since its resolution can be better than 1 nm [Verbeeck04]; it has been frequently used for analysing the chemical composition of nanomaterials [Reiss04]. For instance, relevant to the work explained here, Grobert and co-workers have used EFTEM in order to determine nickel and iron deposited inside the carbon nanotubes [Grobert01]. In this work, mainly

EFTEM is used as an analysis tool for the chemical compositional analysis of materials synthesized with TMV as a bionanotemplate. In some cases, EDX in conjunction with conventional TEM attachment is used.

Patterning and aligning functional molecules, nanoparticles, and biomolecules in a regular array or with micrometer and nanometer scale control over surfaces have attracted great interest because of its relevance to many areas of science and technology [Xia98,Piner99]. In this manner, the interactions between the organized materials can be easily controlled in a very simple way. An attractive method for structuring surfaces is microcontact printing (μCP) method because of its simplicity, cheapness, rapidity, and a high spatial resolution down to a few tens of nanometers [Xia98,Biebuyck97]. μCP prints or rather contact-transfers molecules onto surfaces of interest such as gold or silicon oxide, using an elastomeric stamp whose surface has itself been patterned in an appropriate relief structure. Various biomolecules (dendrimers, DNA) and nanomaterials have successfully been printed using the μCP method [Bernard00,Nakao03,Wu02]. For example, Nakao and co-workers reproducibly created highly aligned DNA nanowires on various substrates by firstly aligning DNA nanowires on a stamp surface and then directly printing them on various surfaces [Nakao03]. In this thesis, mainly μCP has been used as a patterning method.

Nanometer-scale structures are of great interest as potential building blocks for future electronic and photonic devices. Due to the confinement of electron and hole wave functions upon decrease of the size of the material (after a critical size), the electronic and optical properties change drastically, differing much from those of the bulk material [Alivisatos96]. The changes in electrical, optical, and magnetic properties of the materials upon decrease of the size have been realized in various materials. For example, the band gap of a semiconductor such as CdS can be tuned from its bulk value of 2.5 eV to about 4.5 eV for ~2 nm sized clusters [Alivisatos96]. The influence of the size reduction on the magnetism of CoRh has been explored by Zitoun and co-workers [Zitoun02]. A strong enhancement of the magnetization, up to twice the value of the bulk alloy has been reported in ~1.65 nm CoRh nanoclusters [Zitoun02]. In addition, conductance measurements on metallic

contacts formed between two macroscopic wires have shown well-defined quantization (quantum mechanical conductance) in air but also for many environmental conditions and situations [Krämer95]. Therefore, measurements of the physical properties of the nanomaterials obtained after mineralization of the TMV particles are important for observing properties different from their bulk counterparts.

Chapter 2 gives a very short introduction about the history, the structural and biophysical properties, and the place of TMV in nanoscience.

Chapter 3 is intended to serve as a basic introduction to the experimental techniques used during this work. Special emphasis has been devoted to electroless deposition, transmission electron microscopy (TEM), microcontact printing, and atomic force microscopy. In addition, very simple introductions to electron beam lithography, and cathodoluminescence are given. Especially, electroless deposition, energy filtering transmission electron microscopy (EFTEM), and microcontact printing parts are vital in order to follow the discussions in Chapter 4 to Chapter 6.

Mineralization of TMV particles for metal nanostructures is depicted in Chapter 4. Synthesis of nickel, copper, and cobalt-iron alloy nanowires within the hollow channel, and size-enhancement of gold nanoparticles at the ends of the virions using a variety of electroless deposition methods are explained in detail. Emphasis is placed on explaining the mechanism of each process. High-resolution TEM of the nickel nanowire is presented. Besides that, chemical composition of all the synthesized metal nanostructures is analyzed on the nanometer scale. Primarily, EFTEM is used as a characterization tool. In this way, elemental maps of the synthesized materials are shown. EDX is used for the characterization of the size-enhanced gold nanoparticles at the ends of TMV particles. Furthermore, as a first step for contacting the nanowires inside the TMV, transport properties of the TMV rods contacted between the gold nanoelectrodes on a SiO_2 surface are reported.

In Chapter 5, mineralization of TMV for zinc oxide nanostructures is described. The mechanism of the electroless deposition of zinc oxide is explained in detail. The chemical composition of the deposited material on the outer surface of the TMV, investigated by using EFTEM, is explained in

this chapter. Furthermore, cathodoluminescence emission from the ZnO rods on a TEM grid surface is explained.

Chapter 6 is dedicated to printing and alignment of TMV particles on various surfaces, mainly using the microcontact-printing method. In this chapter, top-down and bottom-up approaches are merged in order to obtain ordered assemblies of TMV particles. Furthermore, parallel assemblies of the TMV particles on a TEM grid and the selective assembly of the virus particles on 3-aminopropyltriethoxysilane (APTES) templates, generated by using electron beam lithography, are discussed in detail.

CHAPTER 2

Tobacco Mosaic Virus

This chapter is intended to serve as a basic introduction to the Tobacco Mosaic Virus (TMV), namely its history, structure and biophysical properties, and place in nanoscience. Understanding the basic units of the TMV is crucial in order to use it in nanoscience as a bionanotemplate for the synthesis of interesting nanomaterials to be used in future nanotechnologies.

2.1 Short History of TMV

The tobacco mosaic virus (TMV) is one of the simplest viruses known and it was the first virus to be discovered [Klug99,Bos99]. TMV, an RNA virus that causes mosaic disease in tobacco and similar effects in other plants by showing characteristic patterns of yellow-green coloring with different shades (mottling and discoloration), has frequently been used as an experimental subject. In plants, the tobacco mosaic virus leads to severe crop losses in many regions around the world. It has been known to infect tobacco, tomato, pepper, and a number of ornamental flowers. There are many different strains of TMV in nature. Its ready availability has made it convenient for biochemical and structural studies, in addition to the fact that it does not infect animals. TMV has also provided a system for the development and application of new techniques in X-ray analysis and

electron microscopy [Klug99]. An example of a complex self-assembling biological nanostructure that has been examined in detail is TMV in which self-assembly strategy uses chemical or physical forces operating at the nanoscale to assemble basic protein subunits into larger structures (virus particles). Indeed, many of the concepts of biological self-assembly are derived from the studies of the TMV [Whitesides91].

TMV has been known for more than 100 years, dating back to Martinus Beijerinck's description as 'an infectious substance that was filterable with filter paper and could move through an agar medium' [Klug99,Scholthof04,Bos99]. This property provided a direct comparison with bacteria, which were not filterable with filter paper and remained fixed in the agar medium. Beijerinck expressed a firm belief in the existence of an autonomous sub-microscopic (that is subcellular) form of life. This is where an entirely new concept emerged. Therefore, the prevailing theory that all 'viruses are microbes' was altered to 'a virus is not a microbe' after Beijerinck's work. Most people accept Beijerinck's work as the beginning of 'virology', the study of viruses and their properties. However, most of the early understanding of the properties of viruses comes from the studies of TMV by W. M. Stanley and his colleagues [Klug99]. W. M. Stanley was awarded the Nobel prize in chemistry 1946 for his work in which he succeeded in isolating 'a crystalline protein possessing the properties of tobacco mosaic virus' for electron microscopy and he also showed that it remains active even after crystallization. The work of Stanley has also resulted in the emergence of a new field, 'molecular biology'. TMV is also the first virus of which the particles have been seen with an electron microscope (by Kausche and Ruska in 1939) [Bos99]. In 1955, Heinz Frankel-Conrat and Robley Williams demonstrated that RNA and coat protein of TMV self assemble to the virus, indicating that this is the most stable structure (the one with the lowest free energy) [Klug99]. TMV has been accepted as a preferred didactic and a symbolic model to illustrate the essential features that define a virus. Since then, TMV became known as the virus of choice for basic studies in plant biology, virology, medical virology, structural biology, biochemistry, and genetics. The huge scientific literature about the TMV and its choice for many pioneering investigations in structural

molecular biology, X-ray diffraction, virus assembly and disassembly, etc., are fundamental due to the large quantities of the virus that can be obtained, as well as the fact that it does not infect mammals (harmless for people). After growing a few infected tobacco plants in a greenhouse and some laboratory procedures (centrifugation, incubation, etc.), several grams of the virus can be extracted so that TMV can be treated almost as an organic chemical, rather than an infective agent or a virus. However, the use as well-defined template requires careful procedures (e.g. to avoid cross infections with other virus strands), so the overall amount used was < 5 g.

2.2 Structural and Biophysical Properties of TMV

TMV is the type member of the tobamovirus group (RNA viruses infecting plants), rod-shaped particle 300 nm long and 18 nm wide with a central channel of 4 nm length (see Figure 2.1). It is a rigid-rod shaped composite structure of protein and RNA. Moreover, the virus particle, known as a virion as well, is extraordinarily stable and can be manipulated under a variety of conditions. Each TMV particle contains 2130 identical protein subunits (each consisting of 158 amino acids) of molecular weight 17.5 kD, which form a right-handed helix of pitch 2.3 nm with 16$1/3$ protein subunits per turn [Klug99,Namba89,Culver02,Lu96]. A single strand RNA of 6395 nucleotides representing the 5% particle weight is the backbone and follows the helical arrangement (see Figure 2.1) of the protein subunits. The RNA is located a few nanometers away from the inner surface of the virion and is protected from the action of cellular enzymes by the coat protein. There are three nucleotides bound to each protein subunit (a structural building block). The amino acid sequence of the protein subunit was determined and confirmed by the complete genetic sequence of the viral genome (RNA).
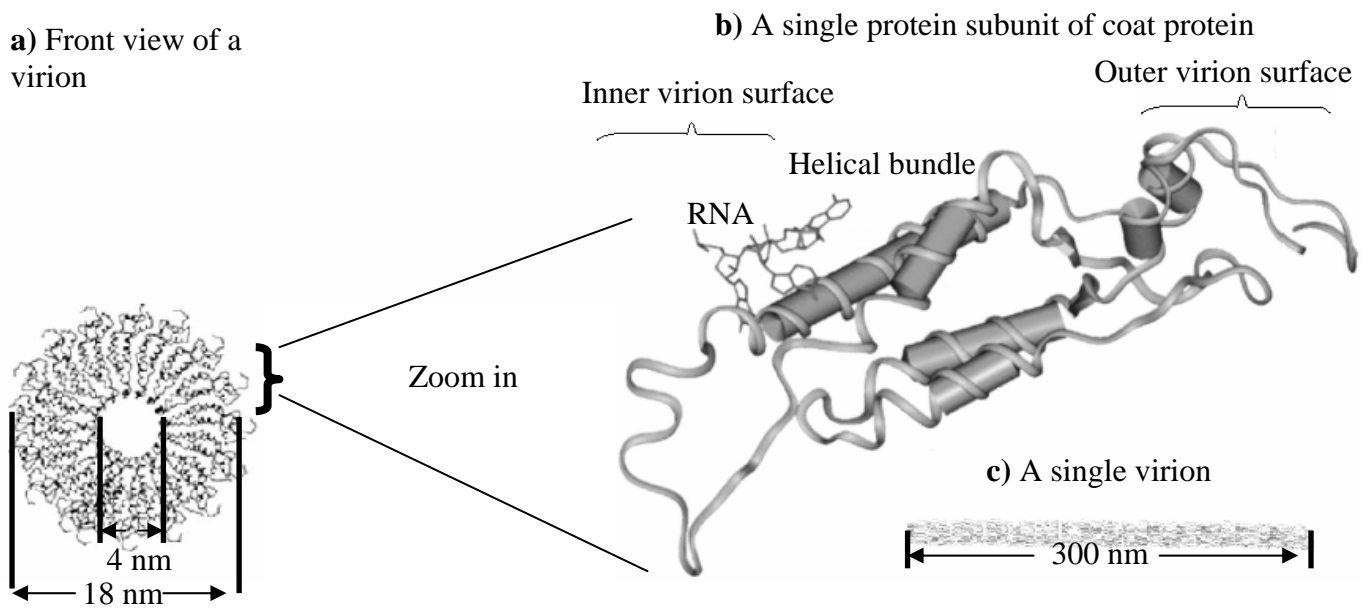
a) Front view of a virion

b) A single protein subunit of coat protein

Inner virion surface

Outer virion surface

Helical bundle

RNA

Zoom in

c) A single virion

4 nm

18 nm

300 nm

Figure 2.1: Schematic representation of the tobacco mosaic virus with its basic components. **(a)** The front view of the virion 18 nm in diameter with the inner channel of 4 nm wide. **(b)** Structure of a single virion coat protein subunit showing the regions of the protein subunit in the inner and outer virion surface. RNA interacts with the protein subunit a few nanometers away from the inner virion surface. **(c)** A single TMV particle (a virion) in 300 nm in length (adapted from ref. [Culver02]). The drawings are not to the scale.

The TMV is one of the best-studied viruses. The structure of the TMV has been determined by fiber diffraction methods at 2.9 Å resolution [Namba89]. The structural details of the TMV provide some indications about the molecular basis of the virus assembly and disassembly although not all of the interactions between the protein subunits and the RNA are known in detail. A general description of the assembly process indicates that the RNA binds to the 20 S aggregates (34-protein subunit two-turn cylindrical disk aggregate) of the protein, and elongation of the viral rod proceeds step by step by addition of 20S aggregates [Namba89,Culver02]. Without RNA binding, the structure of the inner loop is distorted in order to allow access of the RNA to its binding site within the central cavity of protein subunits aggregate. However, RNA binding results in the structural ordering of the residues within the inner loop, encapsulating the nucleoprotein complex into a virion-like structure,

and allowing the self-assembly of the protein subunits to proceed. The TMV virion is highly stable and does not denature for extended periods of time in the environment. However, upon entry into a cell, the normally stable TMV particle destabilizes to initiate virus translation and replication. Viral disassembly is driven by electrostatic repulsions between the negative charges in two carboxyl-carboxylate pairs from glutamate and aspartate residues, located at the interface between the adjacent coat protein subunits, and a phosphate-carboxylate pair. Within the extracellular environment, the repulsive interactions made by the negatively charged carboxylate groups (aspartic and glutamic acid) would be stabilized by the presence of positively charged cations, such as Ca^{2+} [Culver02]. Therefore, the virus is very stable within the extracellular environments, for example on silicon oxide surfaces.
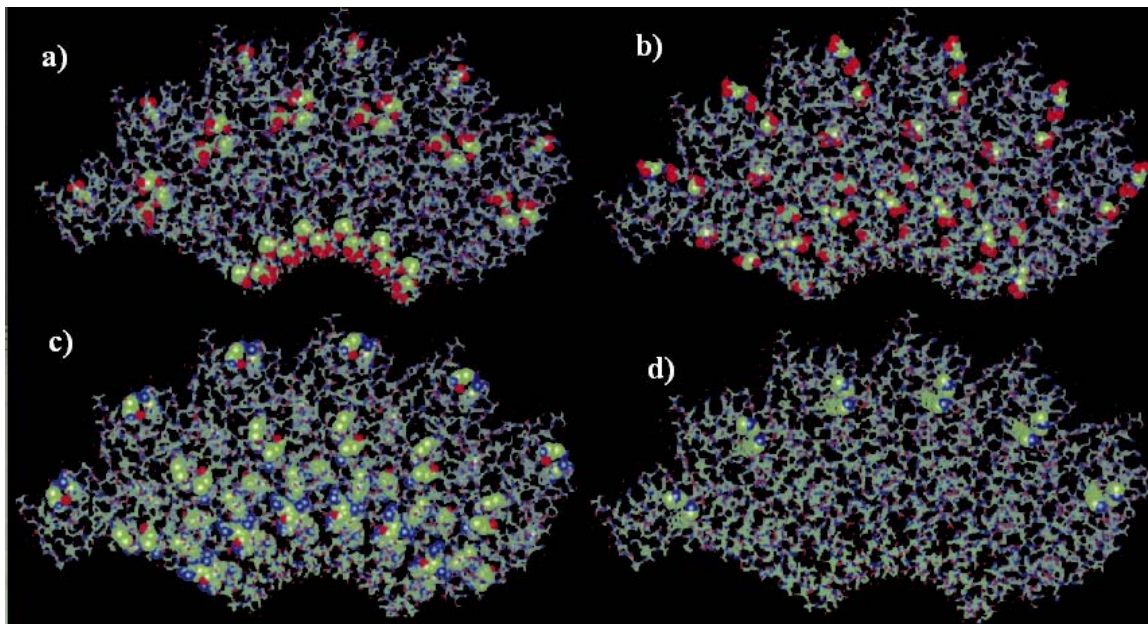
Figure 2.2: Computer-generated images of six TMV subunits arranged as in the native virion and viewed parallel to the helical axis. Top and bottom sections of each image show the amino acids exposed on the outer surface and internal channel wall, respectively. **(a)** Glutamic acid. **(b)** Aspartic acid. **(c)** Arginine. **(d)** Lysine. Note the high density of glutamic acid at the inner channel and the high density of arginine clustering around the RNA groove (adapted from ref. [Shenton99]).

Because of its specific surface functional groups on the outer surface as well as on the central channel surface, TMV has an isoelectric point at a pH value of about 3.5 determined by using electrophoretic measurements [Deggelmann94]. At the isoelectric point the surface potential of the particle and therefore the electrophoretic mobility is zero. The mobility at high pH values (>6) is nearly constant [Deggelmann94]. In this pH regime, the acidic surface groups are completely dissociated. At a pH value of 6 the mobility of the particles begins to decrease with decreasing pH value. An electrophoretic charge of about $1000e^-$ has been obtained meaning that TMV is negatively charged above its isoelectric point [Deggelmann94]. Outer and inner surface of the virion contain quite a large number of different amino acids (glutamic acid, aspartic acid, arginine and lysine), which determine the high surface specificity of the inner surface and the outer surface of the virion [Culver02], (see Figure 2.2). Each amino acid (totally 158 amino acids for each protein subunit) has a different isoelectric point, which determines the overall charge of the inner surface and the outer surface of the virion. For example, aspartic and glutamic acids have an isoelectric point of around 3-4 and arginine and lysine have an isoelectric point of 9-11, depending on the location of the amino acids. Dujardin et al. have mentioned that the exposed functional groups within the cavity are predominantly aspartic and glutamic acids [Dujardin03], (see Figure 2.2). Nevertheless, the outer surface contains a significant number of lysine and arginine, (see Figure 2.2). At the pH of 8, the carboxylic group of aspartic and glutamic acids will be negatively charged and the amino group of the lysine and arginine will be positively charged. Hence the inner surface is more negatively charged than the outer surface. Of course the amino acids are not the only species affecting the properties of the virions. In addition, the presence of RNA in the assembled virus greatly affects the properties of the assembly. The isoelectric point of the assembled virus is 3.5 instead of 4.3-4.6 in the isolated TMV protein subunit [Gallagher83]. The RNA is buried within the protein assembly of the virus and interacting with the protein through electrostatic interactions, hydrophobic interactions and hydrogen bonding between the RNA and the protein subunit (arginine and asparagine, see Figure 2.2). A carboxylate-phosphate interaction is predicted to form the TMV

structure to occur between aspartic acids (see also Figure 2.2b for aspartic acids close to the internal surface) of each protein subunit and an RNA phosphate group. Mutation experiments (aspartic acids to asparagine) showed that the length of the virions decreased from 300 ± 29 for wild type TMV to 254 ± 108 for the mutated TMV indicating that aspartic acids play an important role in preserving the virion structure [Lu96].

TMV can be precipitated from an aqueous solution in the presence of divalent metal ions (Cu^{2+}, Cd^{2+}, Pb^{2+}, Zn^{2+}, and Ni^{2+}) at a critical concentration, depending on the pH and ionic strength of the solution [Nedoluzhko01]. These aggregated virus precipitations formed ordered structures (long strips, up to several centimeters long, 50-100 μm wide) upon drying on a glass surface. However, no precipitation from the virus solution was observed with either Ca^{2+} or Mg^{2+}. The different behavior of the metal ions towards precipitation of the TMV particles has been attributed to the different values of the binding constants of these metal cations with the carboxylic acids. The binding constants of Ca^{2+}(1.9) and Mg^{2+}(2.2) with formic acid are much lower than those of Cu^{2+} (24), Cd^{2+}(14), Pb^{2+} (45), Zn^{2+} (5.4), and Ni^{2+} (4.7) [Nedoluzhko01]. Therefore, carboxylate-metal cations interactions play an important role in the formation of ordered patterns of TMV particles. Approximately 6 cadmium ions were found for each TMV protein subunit in the films prepared at the pH of 7. In addition, TMV particles can self-assemble end-to-end along their long axis depending on the experimental conditions used. This kind of self-assembly has been attributed to the complementary electrostatics and hydrophobic interactions between the ends of the helical structure [Shenton99,Lu96]. For example, mutation of glutamic acid on the inner surface of the virion (see also Figure 2.2a for glutamic acids close to the inner surface) with glutamine indicated that the length of the virus rods increased from 300 ± 29 for wild type TMV to 1450 ± 640 for mutated TMV [Lu96].

2.3 TMV in Nanoscience

Biologically derived materials are increasingly being utilized to impart novel functionalities at the micro- and nanoscale level. Rod- or tube-like biological molecules such as DNA [Braun98], tobacco mosaic virus (TMV) [Shenton99], bacteriophages [Mao04], protein tubes [Reches03] and protein fibers [Mertig98] are well defined in their chemical composition (also structure) and used as templates for the nucleation of nanoscale inorganic materials. For example, DNA has been exploited as a template for the construction of metal-coated nanowires and used in combination with carbon nanotubes to make field effect transistors [Braun98,Keren02]. TMV as a template for the nanofabrication is advantageous since (a) TMV particles have the unique structure being 300 nm long and 18 nm in diameter with a 4 nm axial channel; (b) TMV particles of the same type are identical in structure, shape, and dimension (monodisperse); (c) they are very stable both physically and chemically in a variety of chemical environments; (d) they can be coated with metals, silica, and semiconductor materials; (e) the physical, biological, and genetic properties of TMV have been well characterized (also not infecting animals-harmless for people). In addition, since TMV has been the model system for understanding the basic principles of virology and molecular biology it might be also a model system in nanoscience for the fabrication of nanomaterials and assembly of them on the outer as well as within the central channel surface of the TMV particles. These advantages make TMV a promising candidate for the application in nanoscience and nanotechnology.

For the first time Kausche et al. in 1939 have used TMV as a template for the deposition of gold colloids on TMV particles [Kausche39]. Later in 1999, Shenton et al. have reported the use of TMV to direct the deposition, and assembly of inorganic nanoparticles and microstructures on the outer surface of TMV particles [Shenton99]. They showed that TMV is a suitable template for reactions such as co-crystallization (CdS and PbS), oxidative hydrolysis (iron oxides), and sol-gel condensation (SiO_2). The internal and external surfaces of the protein consist of several repeated

patterns of charged amino acid residues, for example glutamate, aspartate, arginine, and lysine (see Figure 2.2). These functionalities offer a variety of nucleation sites for the surface controlled inorganic deposition within the internal channel and also on the outer surface of the TMV particles [Shenton99,Knez04]. More interesting is the deposition of materials within the central channel of the virus. Dujardin et al. have produced linear arrays of Ag nanoparticles specifically organized along the inner channel of the virion by incubating TMV with $AgNO_3$ in the dark at neutral pH followed by UV irradiation [Dujardin03]. It is important to note that these Ag nanoparticles prevented the stain (uranyl acetate) from penetrating further in the hollow channel of TMV, which has not been discussed in the original work [Dujardin03]. This result indicates that during mineralization of the virions, metal ions diffuse through the central channel instead of penetrating through the protein subunits. As mentioned above, the metal ions interact strongly with the carboxylate groups (glutamate and aspartate) present in the TMV coat protein. Interestingly, the inner surface has a high spatial density of glutamic acid residues, suggesting that nucleation within the 4 nm wide inner channel might be expected in most of the experimental conditions used for metallizations [Shenton99]. Recently nickel and cobalt nanowires ~3 nm diameter with lengths up to the micrometer range within the central channel of TMV rods have been synthesized by electroless deposition [Knez04].

In addition, diazonium (on the exterior surface) and carbodiimide coupling (on the interior surface) reactions have been used to modify specific surface-charged TMV amino acids thereby expanding dramatically the utility of TMV rods in the future for the organization of optically and magnetically interesting nanoparticles on the outer and the inner surface of the virion [Schlich05]. Recently, by atomic layer deposition, a gas phase deposition process, TMV particles have been decorated with TiO_2 and Al_2O_3 [Knez06]. The applied method has the ability of controlling the thickness of the deposited film in subangstrom range and is thus of high interest for nanoscale structuring. Genetic engineering of the wild type TMV particles has been also accomplished by different research groups [Demir03,Dujardin03,Yi05]. For instance, cysteine residues have been genetically

engineered onto the surface of TMV particles, which provide attachment sites for fluorescent markers or ligand-linker groups [Demir03,Yi05]. Consequently, TMV is a promising bionanotemplate for the synthesis of a variety of nanomaterials on its external and internal surfaces.

CHAPTER 3

Methods

This Chapter provides brief introductions to the techniques used during the course of this thesis work namely transmission electron microscopy (in Section 3.1), atomic force microscopy (in Section 3.2), electroless deposition (in Section 3.3), microcontact printing (in Section 3.4), electron beam lithography (in Section 3.5), and cathodoluminescence (in Section 3.6). Basic understanding of these methods is prerequisite in order to follow the discussions in Chapter 4 (Mineralization of TMV for Metal Nanostructures), Chapter5 (Mineralization of TMV for Zinc Oxide Nanostructures), and Chapter 6 (Printing and Aligning TMV Particles on Surfaces).

3.1 Transmission electron microscopy (TEM)

3.1.1 Brief Description of TEM

Transmission electron microscopy (TEM), first developed in the 1930's, is a fundamental technique used to characterize specimens in material science [Williams96]. Here the same acronym will be used to denote both the technique (microscopy) and the instrument (microscope). A TEM is very similar to an optical microscope (OM), in which radiation is emitted from a source and passed

through a condenser lens until it interacts with the sample at or near the objective lens. However, in contrast to OM, a TEM uses a focused beam of electrons instead of light in order to image the specimen and to gain information about its structure and composition. Advantage of the TEM: higher resolution because of the shorter wavelength. Instead of transparent lenses focusing the light in the OM, the TEM uses electromagnetic lenses. After interacting with the sample, the electrons travel through a series of additional magnetic lenses to a fluorescent viewing screen where the electrons create photons, allowing the user to observe an optical image with very high magnification (Figure 3.1). The darker areas of the image represent parts of the sample that allow only few or no electrons to pass, while the brighter areas correspond to parts with higher electron transmission. Note that an OM has a much simpler setup since optical lenses are quite easily produced and adjusted.
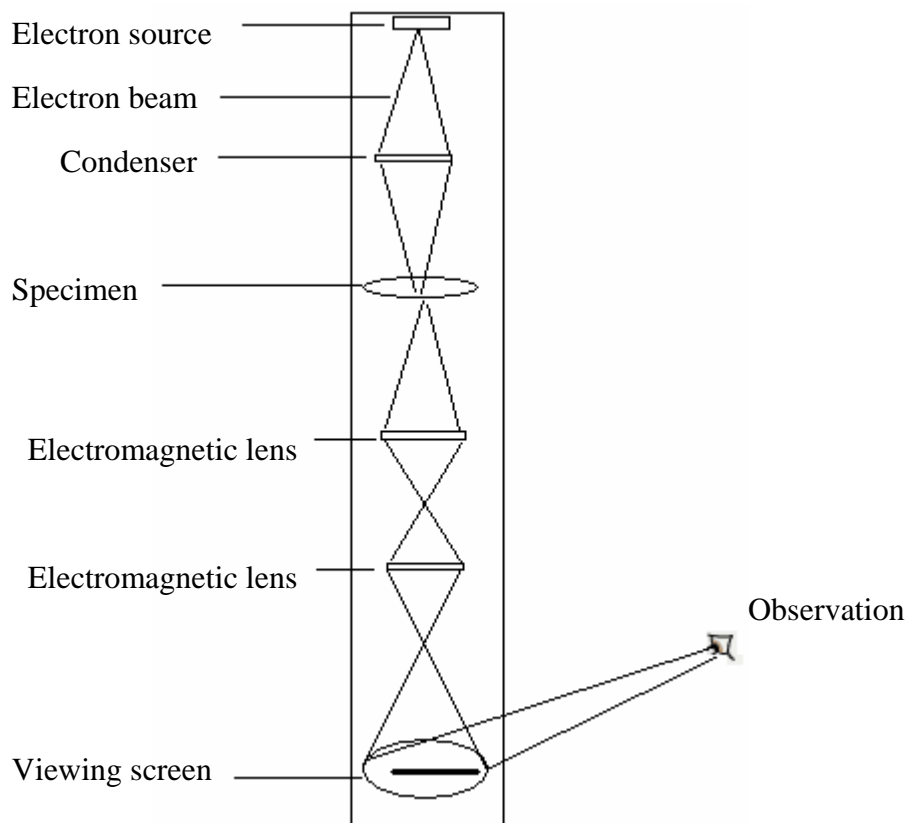
Figure 3.1: Schematic view of a typical transmission electron microscope with important components.

In TEM, electrons of very high energy (tens up to hundreds of eV), capable of removing one of the tightly bound inner-shell electrons from the attractive field of the nucleus, are used in the image formation. These electrons produce a wide range of secondary signals from the irradiated specimen. Figure 3.2 is a schematic view of an incident electron beam interacting with a sample and shows a variety of radiation emitted from the sample surface [Williams96]. The TEM offers a tremendous range of signals from which one can obtain images, diffraction patterns, and various kinds of spectra from the same small region of the specimen, the size of which ranges from a few nm^2 to a few μm^2.

Incident electron beam

X-rays

Visible light

Backscattered electrons

Secondary electrons

Absorbed electrons — Specimen —

Elastically scattered electrons

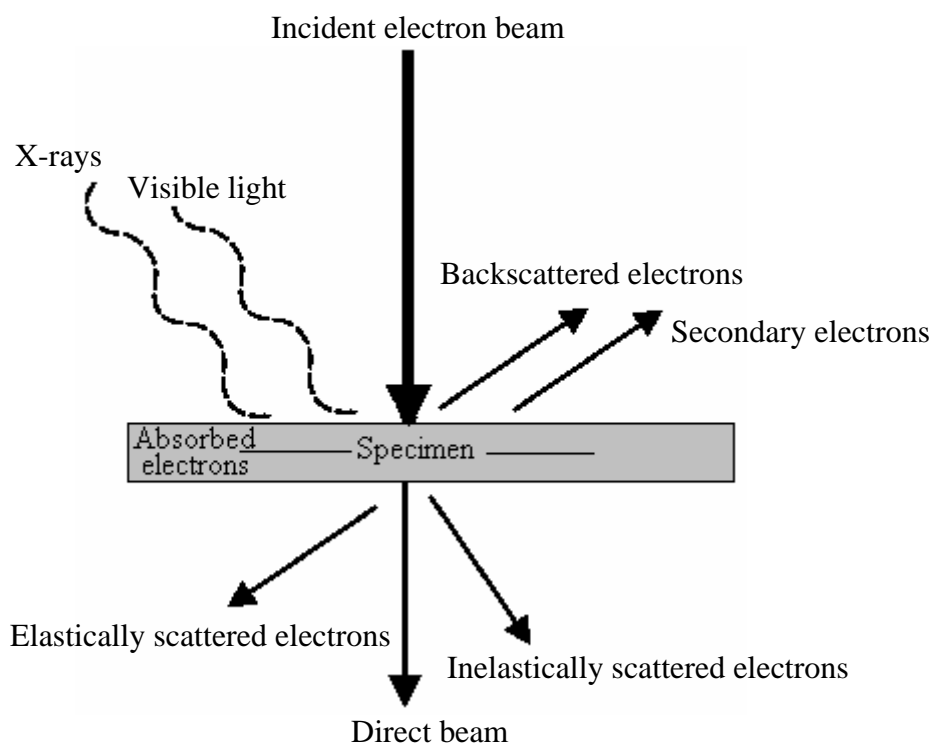Inelastically scattered electrons

Direct beam

Figure 3.2: Schematic representation of signals generated when a high-energy beam of electrons interacts with a thin specimen. Most of these signals can be detected in different types of TEM [Williams96].

In TEM, the elastically and inelastically scattered electrons are of primary interest. When the incident electron beam traverses a thin specimen, electrons scatter upon hitting the sample since they interact with either the nuclei of the atoms and/or the electron clouds. Incident electrons that

interact electrostatically with the sample and lose little or no energy are termed elastically scattered. These electrons are used for imaging and diffraction. Inelastically scattered electrons, losing energy as a result of interaction with the sample, are used for various types of spectroscopy such as electron energy-loss spectroscopy (EELS). EELS exploits the inelastically scattered electrons to learn about the chemical composition of a sample [Williams96]. X-rays emitted from the sample can be used in energy dispersive x-ray spectroscopy (EDX): The X-ray energy distribution shows maxima, characteristic for each element, and is therefore useful for determining the elemental composition of a specimen [Williams96].

Imaging in TEM is a consequence of contrast within a sample and image contrast arises because of the scattering of the incident beam by the specimen. The electron wave can change both its amplitude and phase as it traverses the specimen. Hence, there are two types of contrast in TEM, namely, phase contrast and amplitude contrast [Williams96]. The phase contrast is utilized mainly in high-resolution TEM imaging and is here of minor importance; it is based on the interference of electrons with different phases, creating fringes. There are two principal types of amplitude contrast, namely mass-thickness contrast and diffraction contrast. The mechanism of mass-thickness contrast is that high-Z (high atomic mass) regions of a specimen scatter more electrons than low-Z regions of the same thickness. Similarly, thicker regions will scatter more electrons than thinner regions of the same average Z. Therefore, high Z or thicker regions appear darker than other regions [Williams96]. Biological objects show only weak contrast since they consist mainly of low-Z elements (C, H, N, O). Consequently it is necessary to treat the preparations with special contrast enhancing chemicals (heavy metal ions, for example, uranyl acetate). Diffraction contrast arises from coherent elastic scattering: The incident electron wave interacts with the lattice planes (periodic atomic arrangement) of a crystal. Depending on the incident angle, the elastically scattered electron wave can add (in phase, appearing white), or - in other regions - cancel (out of phase, appearing dark) [Williams96].

3.1.2 Energy-filtering TEM

Energy-filtering transmission electron microscopy (EFTEM) has emerged as a powerful tool for the analysis and characterization of materials at the nanometer scale. Using electrons with an energy loss characteristic of an atomic core level, quantitative two-dimensional elemental distribution maps can be obtained relatively fast, with nanometer resolution and high chemical accuracy [Egerton96,Williams96]. In general, a resolution of 1 nm or better is attainable for realistic parameters and a wide range of energy losses [Verbeeck04].
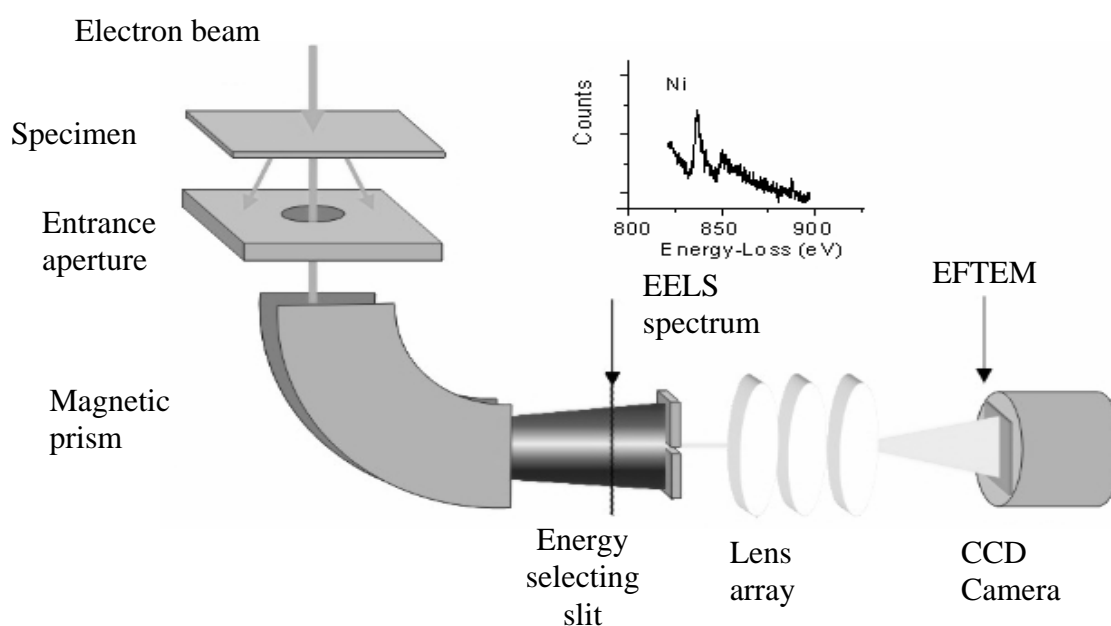

Figure 3.3: Schematic view of a gatan-imaging filter (GIF) attached to the TEM column behind the imaging lenses. From a polyenergetic electron beam, a monoenergetic electron beam is selected. A Ni energy loss spectrum is given as an example for the chemical sensitivity.

EFTEM uses the information (chemical information) obtained from localized electron energy loss to generate an image (chemical information together with spatial information). As shown in Figure 3.3, a spectrometer (here a gatan imaging filter) disperses the forward scattered electrons and selects the specified energy window with a slit [Williams96]. Instead of the gatan filter (a typical post-column type energy filter), a zeiss omega filter (in-column type energy filter) in the shape of the letter omega can be used. Another new version of the omega filter is the corrected omega type

energy filter (90° corners). Contrary to conventional TEM, where a polyenergetic electron beam forms the image, in EFTEM the image is formed exclusively by a monoenergetic electron beam.

Elemental mapping (see also Chapter 4 and 5) can be accomplished by first defining the ionization edge of a particular element in an overview (large area) energy loss spectrum. Then a series of EFTEM images are acquired with energies below ("pre-edge") and above ("post-edge") the ionization edge energy of the desired element (often two pre-edge and one post-edge images are recorded) [Verbeeck04,Williams96]. Note that these images have much lower intensities than conventional TEM images since only filtered (monoenergetic) electrons are used. From these three images, the EFTEM image, which shows only the contribution of the element, is calculated by using the so-called three-window method [Egerton96] (illustrated in Figure 3.4), which will be explained in the following.
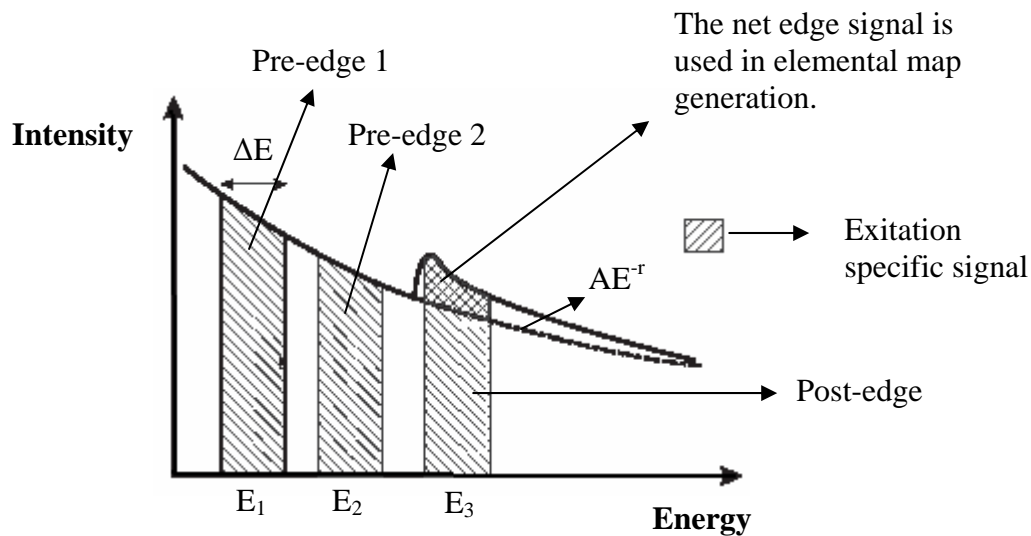

Figure 3.4: Schematic overview of the three-window technique. Background is estimated by using two pre-edge images to fit the background model AE^{-r}, in which A and r are constants in the function I (intensity)$= AE^{-r}$. Then elemental map is obtained by subtracting the background estimate from the post-edge image (adapted from ref. [Verbeeck04]).

For extracting elemental concentrations from EFTEM images, it is necessary to completely remove the background under an ionization edge in order to obtain the net edge signal (elemental map). The

resulting image is quantitative, so the intensity is proportional to the intensity in the loss spectrum under the selected absorption edge of a particular element [Egerton96]. The three-window method uses images acquired with electrons of three different energy regions in the loss spectrum. The software package extrapolates the background from two pre-edge images by using the background intensity AE^{-r} where the r value (pre-edge slope exponent) typically lies in the range between 2 and 6; A is a scaling constant, and E is the electron energy. Background subtraction (already calculated by using two pre-edge images) from the post-edge image leaves the core-loss signal remaining in the form of an elemental map. For example, the elemental map of nickel which has the $L_{2,3}$ edges at 854 eV can be calculated as follows: The slit width of the spectrometer is set to 40 eV, with the selected energy at the center of the slit. The first pre-edge image is acquired at 775 eV, which covers the energy range from 755 eV to 795 eV. The second pre-edge image is acquired at 820 eV, which covers the energy range from 800 eV to 840 eV. The post-edge image is acquired at 885 eV, which covers the energy range from 865 eV to 905 eV. With 60 seconds acquisition time, an elemental map can be obtained in 180 seconds (3x60 seconds-three images). Background subtraction generates the nickel elemental map. Caution must be taken when choosing the energy loss of the pre-edge images in order to ensure that the background model remains valid over the full background extrapolation region, and to avoid introducing artefacts from preceding edges.

3.2 Atomic force microscopy

The atomic force microscope (AFM), invented by Binnig and Rohrer in 1986, has provided new opportunities for studying surfaces with subnanometer resolution by scanning over them very lightly with a tip [Binnig86]. In addition to imaging of surfaces, AFM is also one of the foremost tools for the nanoscale manipulation of matter on surfaces [Takano99]. The AFM can reveal surfaces with atomic resolution [Albrecht87]. It can visualize different properties of materials such as friction, adhesion, elastic modulus, magnetic, electrostatic and chemical composition [Weisenhorn89,Takano99]. In this work, AFM is used as a characterization technique for the

surface topography. Here a simple introduction of AFM principles related to surface topographic imaging is given.

The AFM consists of a cantilever with a sharp tip at its end, typically composed of silicon or silicon nitride with tip sizes on the order of nanometers. The tip is brought close to or in contact with the sample surface (see Figure 3.5) and is then scanned over the surface. The total force between the tip and the sample (composed of attractive and repulsive components) leads to a deflection of the cantilever normal to the surface (in z direction) according to Hooke's law, in which the spring constant of the cantilever is known [Weisenhorn89]. Generally, the deflection of the cantilever is measured using a laser spot reflected from top of the cantilever into an array of photodiodes.
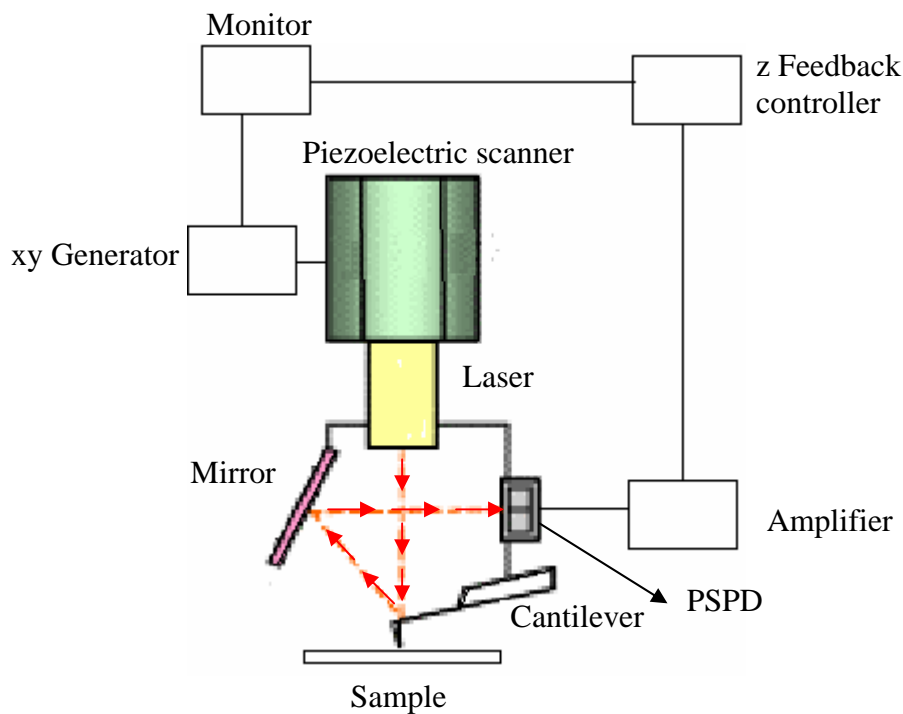

Figure 3.5: Components of a typical atomic force microscope.

Figure 3.6 shows an interatomic force vs. (z) distance curve, which illustrates the force between atoms on a cantilever tip and atoms on a sample surface vs. their separation. Three regions are labeled on the Figure 3.6, which are very important in order to understand the interaction of the tip atoms with the surface atoms. The first region indicates practically no interaction of the tip atoms with the surface atoms since the distance between them is too large. Hence no deflection of the

cantilever can be observed in this regime, and the total force is very close to zero. The second region is the noncontact regime (NC), ranging from a few nanometers to tens of nanometers, which represents the tip-to-sample spacing for non-contact (NC) AFM. The third region corresponds to the contact (C) regime, less than a few angstroms. In the contact regime, the interatomic forces are repulsive (the total force on the cantilever is positive), however in the non-contact regime they are attractive (the total force on the cantilever is negative), and largely a result of long-range van der Waals interactions.
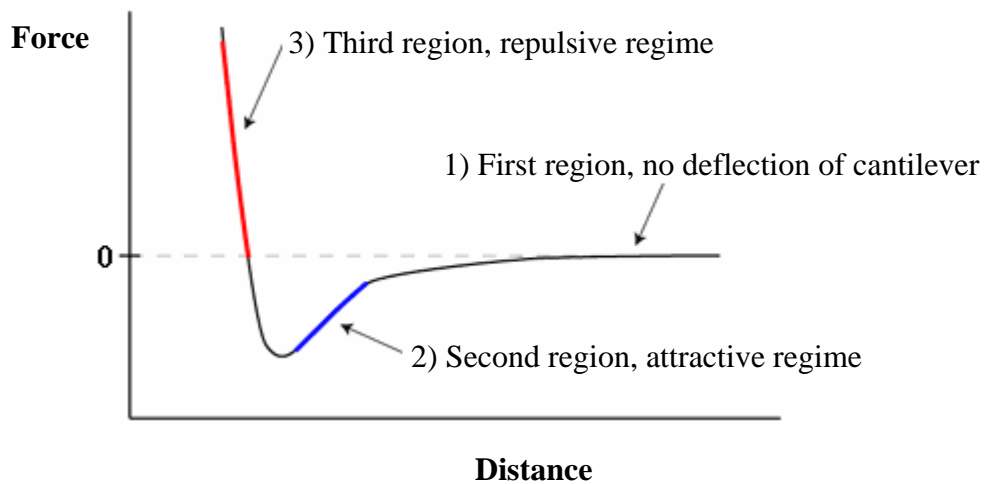
Figure 3.6: Interatomic force vs. distance curve.

In NC mode AFM, a stiff cantilever is oscillated near its resonant frequency (typically from 100 to 400 kHz) with an amplitude of a few to tens of nanometers, meaning that the tip is quite close to the sample, but not touching it. The forces between the tip and the sample are quite low, on the order of pN (10^{-12} N) [Weisenhorn89]. The sensitivity of this detection scheme provides very high vertical (z) resolution (often smaller than a nanometer), like in the case of contact AFM. The detection scheme is based on measuring the changes to the resonant frequency or amplitude of the cantilever. In this work, most of the time NC-AFM is used because it is advantageous for soft materials. The vertical forces are at least 1000 times smaller than in contact mode, which employs 10^{-9} N to 10^{-6} N. The data collected by the AFM can be represented in several forms such as topography, error signal images, and frictional force images, etc. Here, topography and error signal images were acquired

simultaneously. A topography image is the most common way of representing the features on the surface. Hence, the AFM tip follows the surface contour. In the error signal images, the images only represent the edges of the features in the topography images, because the cantilever deflection (deviation from the desired value) is used directly to generate the topographic data set.
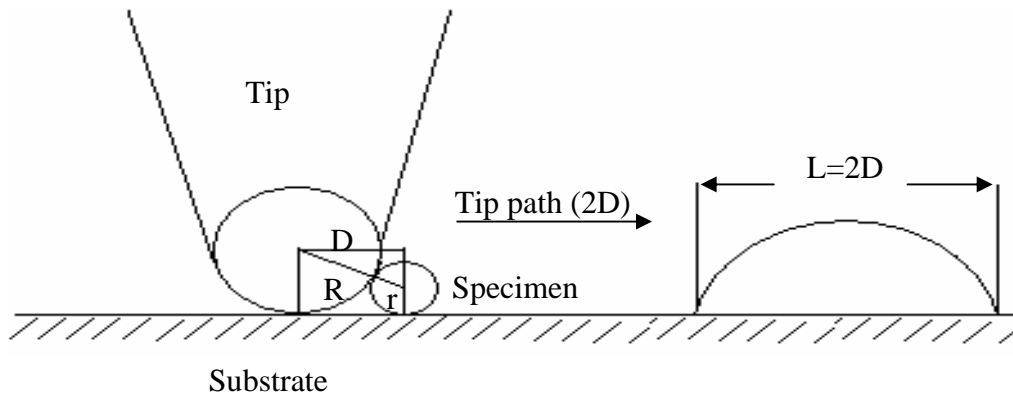

Figure 3.7: Schematic representation of tip geometry effect on soft specimen. The apparent width $L(=2D)$ is defined by the following expression: $L=4(Rr)^{1/2}$, in which R is the tip radius and r is the specimen radius.

When a probe tip is scanning over a flat sample surface which has a particle adsorbed on it, the apparent width of the particle is different from the actual width of the particle [Zenhausern92]. The apparent width (L) of the particle can be calculated only if the tip radius and the particle radius are known (Figure 3.7). For example, if the tip radius is 20 nm and the particle radius is 9 nm, the apparent width can be calculated as 54 nm. Therefore, AFM scanning will detect a width of 54 nm instead of 18 nm. Note that the height of the particle is correctly detected.

3.3 Electroless deposition

In general, metallization of surfaces can be achieved by three different methods, contact with liquid metal, vacuum processes and wet electrochemical processes. Liquid metals and vacuum techniques usually require elevated temperatures and complex instrumentations, whereas wet electrochemical

methods can be performed at room temperature and in an aqueous environment. In this case the deposition of the metal of interest onto surfaces occurs by reduction of metal ions. In the case of electrodeposition, electrons are provided by an external current source connected to the conductive substrate. Therefore, a conductive substrate is necessary in electrodeposition. The deposition can be controlled easily by an applied potential or current. For this reason, electrodeposition is very common in industry [Schlesinger00]. Of particular interest is electroless deposition (ELD) of metals and alloys, a very important process in modern technology, especially in the production of new materials for applications in electronics, wear and corrosion resistant materials, medical devices, battery technologies, automotive parts, and coating of non-conductive surfaces [Diamand95,Schlesinger00]. This process supplements and, in some cases, replaces electrodeposition for several practical reasons. Firstly, the solutions for electroless deposition have excellent throwing power (uniform deposition on a surface) and allow plating on materials of very complex shapes and plating through holes. Second, deposits obtained by electroless deposition can be denser (less porous) and can exhibit better properties for anticorrosion and electronics applications. Other important advantages of electroless deposition over electrodeposition include its applicability for metallization (mineralization) of non-conductive surfaces (e.g., glass, ceramics, proteins, polymers etc.) and the ability to selectively deposit thin metal films only on catalyst-covered areas of the substrate. Finally, for ELD processes, an external current source is not needed because electrons are supplied by a reducing agent present in the metallization solution [Schlesinger00]. This is a crucial advantage for the metallization of nanoobjects, which cannot be easily contacted, and often show no conductivity.

Electroless deposition processes can be divided into subclasses as autocatalytic, substrate-catalyzed, and galvanic displacement [Porter02]: When catalytic nuclei (e.g. palladium, semicircles) are dispersed on a noncatalytic substrate surface (Figure 3.8a), or when the catalytic surface is the (usually conductive) substrate itself (Figure 3.8b, semicircles have no meaning here), the metal ions M^+ can be reduced. The reducing agent Red delivers the electrons by being oxidized to Ox^+ at the

catalytically active surface. As illustrated in Figure 3.8c, in some cases, the surface acts as a source of electrons as a consequence of dissolution of surface atoms; hence the surface itself reduces the metal ions instead of a reducing agent present in the solution (galvanic displacement).
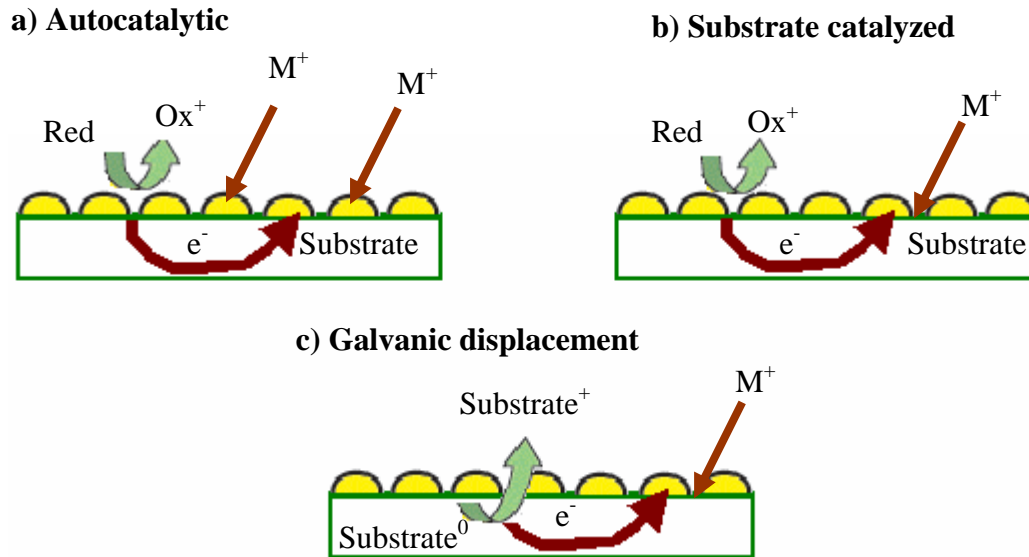
a) Autocatalytic

b) Substrate catalyzed

c) Galvanic displacement

Figure 3.8: Schematic representation of electroless deposition processes. **(a)** Autocatalytic: Reduced nobel metal centers (yellow) act as a catalyst for the reduction of metal ions (M^+) by a reducing agent, *Red*. **(b)** Substrate-catalyzed: The metal ion is reduced by a reducing agent with catalytic action of the substrate surface. **(c)** Galvanic displacement: The substrate, the source of electrons, reduces the metal ions, and partially dissolves (''substrate$^+$'' cations) [Schlesinger00].

Basically, an ELD bath contains the metal ions to be reduced at the substrate surface, a reducing agent, as a source of electrons necessary for the reduction of metal ions in the solution, a complexing agent, which suppresses or inhibits the spontaneous reduction of metal ions in the solution, and usually a buffering agent to maintain the pH of the deposition solution at the desired level. The homogeneous reaction between metal ions in the solution and the reducing agent must be suppressed to prevent growth of small metal or dust particles from growing into larger deposits (spontaneous decomposition). For this reason, the complexing agents are used in an ELD solution (a bath) [Diamand97]. In addition, many additives are used in small concentrations, again to prevent the bath from decomposition (stabilizers), but mainly to improve the deposit morphology. In
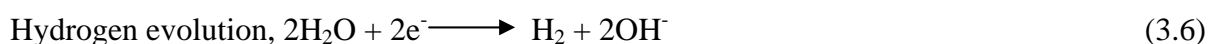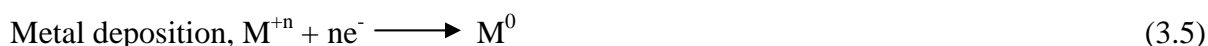
general these types of additives are catalyst poisons (inhibitors) and therefore present in extremely low concentrations, i.e. thiourea. They show strong (often irreversible) adsorption on metal surfaces, blocking surface sites that are required for electrocatalysis [Schlesinger00].

Electroless deposition can be understood easily with a universal electrochemical mechanism. Each process can be viewed as made up of a series of elementary anodic and cathodic reactions in which RH is the general reducing agent and M^{+n} is the metal ion [Schlesinger00], for example with $R=BH_2$, $M=Ni$, and $n=2$.
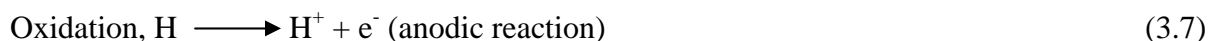
In alkaline media (anodic reactions):

Dehydrogenation, $RH \longrightarrow R + H$ $\qquad$ (3.1)

Oxidation, $R + OH^- \longrightarrow ROH + e^-$ $\qquad$ (3.2)

Recombination, $H + H \longrightarrow H_2$ $\qquad$ (3.3)

Oxidation, $H + OH^- \longrightarrow H_2O + e^-$ $\qquad$ (3.4)

In alkaline media (cathodic reactions):

Metal deposition, $M^{+n} + ne^- \longrightarrow M^0$ $\qquad$ (3.5)

Hydrogen evolution, $2H_2O + 2e^- \longrightarrow H_2 + 2OH^-$ $\qquad$ (3.6)

In acidic media:

Oxidation, $H \longrightarrow H^+ + e^-$ (anodic reaction) $\qquad$ (3.7)

Hydrogen evolution, $2H^+ + 2e^- \longrightarrow H_2$ (cathodic reaction) $\qquad$ (3.8)

One can often observe hydrogen evolution during electroless deposition, described by reactions (3.3), (3.6) and (3.8), which are considered as side reactions. The other reactions are two independent electrode reactions, cathodic branch (reaction 3.5) and anodic branch (reaction 3.2, 3.4, and 3.7). Therefore electroless deposition reaction can be considered to be the combination of both

branches, which must be charge-balanced, so that no electron source is required. This situation can be treated with the concept of the mixed potential theory (MPT). The basic reaction for metal deposition is the reduction of dissolved metal ions. At a catalytic substrate a reducing agent (for example, dimethylamine borane) can be oxidized, liberating electrons for the simultaneous metal ion reduction (see equations (3.1)-(3.8)). The deposited metal must also be a catalyst (autocatalysis); otherwise the metallization would cease once the original substrate is covered completely. In the MPT, the deposition process is considered in terms of two simultaneously occurring partial reactions, reduction of metal ions (cathodic branch, 3.5) and oxidation of the reducing agent (anodic branch, 3.2). Both reactions are generally considered to proceed independent of each other. Once the steady state condition is reached, the anodic and cathodic partial reactions proceed at the same rate (the same current density). In that stage the net current is zero, and the electrochemical potential of the growing surface is determined by both anodic and cathodic kinetics. Obviously, the standard electrode potential of the metal reduction must be larger (more positive) than that of the redox reaction of the reducing agent. This leads to a positive cell potential (E^0_{cell}), and therefore a spontaneous reaction (thermodynamically allowed, $\Delta G = -nFE^0 < 0$), not requiring any external electron source [Schlesinger00]. Without a catalytic surface, the spontaneous solution decomposition does not occur in ELD because the ELD reaction is kinetically inhibited – the MPT applies only in presence of the catalyst.

In spite of relatively intensive studies in recent years, more details such as further side reactions or quantification of rates are still not clearly understood. Attempts have been made to explain the mechanisms and kinetics of electroless deposition; however, a fully accepted model is not yet established [Schlesinger00].

3.4 Microcontact printing

Microcontact printing (μCP), a soft lithography technique, is a general method for forming patterns of a variety of materials on surfaces of solid substrates of interest through contact pattern transfer. Since the first report on μCP by Kumar et al., it has proven to be a very versatile technique for parallel generation of submicrometer-sized patterns [Kumar93]. In conventional microcontact printing, a soft elastomeric stamp with a relief structure is brought into intimate (conformal) contact with a substrate to transfer ink molecules from the stamp surface to the substrate surface [Xia98].
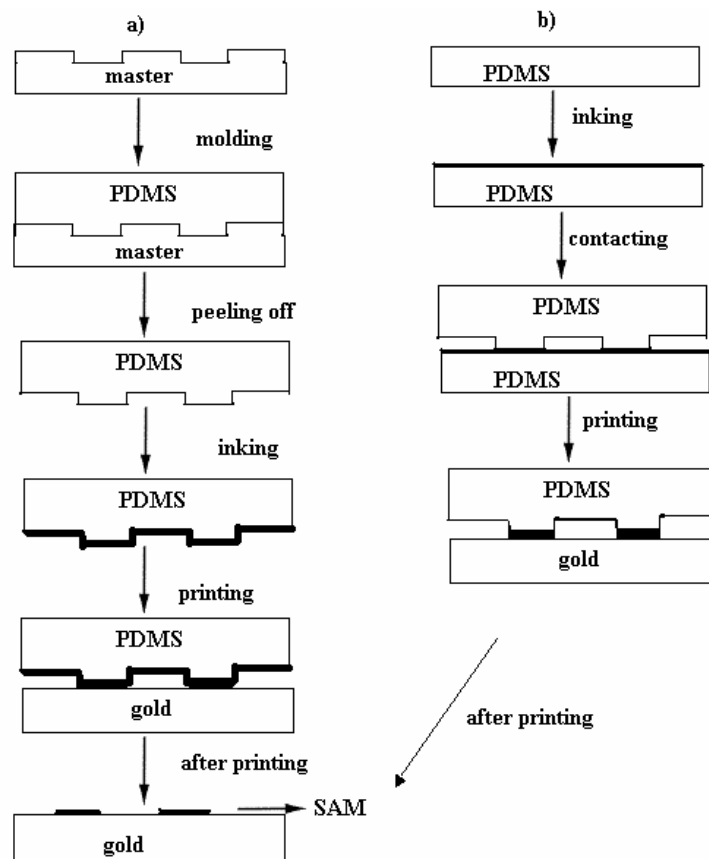

Figure 3.9: Schematic representations of two types of μCP techniques. μCP with a pattern of ordered SAMs on gold surface from printing of alkanethiols with **(a)** a conventional and **(b)** contact-inking with a flat inker stamp. Note that the structured PDMS stamp in (b) is produced like the stamp in (a) involving *molding* and *peeling off* steps.

µCP was first demonstrated for self-assembled monolayers (SAM) of alkanethiolates on gold surfaces [Kumar93,Xia98]. The procedure is remarkably simple (see Figure 3.9). The stamp is fabricated by casting poly(dimethylsiloxane) (PDMS) on a master with the desired pattern. In a typical experimental procedure a mixture of SLYGARD silicone elastomer 184 and a curing agent is poured onto the master. The elastomer is cured for several hours above 50 ^{0}C (up to >100 °C), thereby hardened by crosslinking of polymer chains, and then peeled from the master. The fabricated stamp replicates in reverse the relief of the patterns on the master simply by showing the recessed regions of the stamp corresponding to the raised regions of the master. Then the PDMS stamp is treated with alkanethiols (ink) in ethanol, dried, and brought into intimate contact (sometimes with slight pressure) with a gold substrate. The alkanethiols chemisorb spontaneously on the gold surface (sulfur atoms bind to the gold surface and this process is assumed to occur by loss of hydrogen) [Wilbur96]. In principle, the process can be extended to a huge variety of ink materials. However, the successful printing of the ink molecules depends on many factors, for instance solvent, surface properties of stamp and substrate, type of the ink, and also methods of inking.

Alternatively, inking a structureless stamp, which is cast from a plane surface, with alkanethiol solution, can produce similar patterns on gold surfaces (see Figure 3.9b). When the stamp is inked in this way, the flat stamp is inked selectively only in those places which are finally used in the printing process [Pompe99]. In this way, quite uniform stripes of silanes on silicon wafers were generated by eliminating the problem of capillary condensation of silanes in the wedges of the stamp during the stamping process [Pompe99].

Another way of surface patterning technique is edge transfer lithography (ETL) [Cherniavskaya02]. ETL combines aspects of µCP and dip pen nanolithography (DPN) (a scanning probe nanopatterning technique in which an AFM tip or 'stylus' is used to deliver molecules to a surface via a solvent meniscus [Piner99]) for the patterning of surfaces with a resolution far below µm (~60 nm). This method uses a micropatterned elastomeric stamp as a way to deliver ink along the edges

of the stamp features. Like the inking of the sides of the scanning probe stylus in ETL, the sides and recesses of the stamp's topography are selectively inked by using solvents that dewet on the stamp surface, leaving ink solution within the recesses only. This so-called discontinuous dewetting method can be used for simultaneous and rapid filling of large arrays of microwells, each with similar quantities of reagent. This method takes advantages of the difference in the interfacial free energies of the substrate (solid-vapor) and the liquid of interest (liquid-vapor), and of the controlled topography of the substrate. Liquid is allowed to drain off an array of microwells either by gravity or by pulling the array from a bulk solution. While the zero-dimensional tip of the DPN stylus serves as the transfer point for the ink to the substrate, essentially producing dots of the ink, in ETL the edges of the stamp act as one-dimensional transfer curves. For example, self-assembled monolayers (SAMs) and titanium dioxide nanoparticle materials were directly patterned on glass substrates at a resolution of a few tens of nm [Cherniavskaya02]. Such SAM patterns can be used as templates for the guided self-assembly of molecular and nanoparticle materials.

As obvious from all available techniques, the surface chemistry of substrate and stamps is crucially important. PDMS is the preferred stamp material in µCP [Xia98]. It has found many applications due to its unique properties, which arise mainly from the nature of the siloxane bond (Si-O) and the methyl groups [Hillborg98]. These properties include extremely low glass transition temperature (-123 °C), low surface energy, high permeability to gases, good insulating properties, and very good thermal stability. Moreover, many physical properties remain more or less unchanged over a wide range of temperatures. However, the mechanical properties of PDMS are usually very poor at room temperature, unless reinforced with silica and/or crosslinked. The degree of crosslinking determines the elastic modulus and thus the applicability for achieving the required conformal contact: If the modulus is too low, the stamp will become unstable, if it is too high, the stamp will contact the substrate only at a few spots (since nm scale flatness cannot be achieved over several mm length).

In order to develop useful properties, very high molecular weights are required. PDMS is offered as a kit, which contains a *base* and a *curing agent* (an organometallic crosslinker) [Campbell99]. The

PDMS components can be mixed in various mass ratios (curing agent to base ranging from 1:5 (harder) to 1:15 (softer)) to alter the level of cross-linking in the final polymer structure. Both components of the kit contain siloxane oligomers terminated with vinyl groups. In addition, the *curing agent* contains cross-linking siloxane oligomers containing at least three Si-H bonds each. The *base* contains a special platinum-based catalyst, which catalyzes the addition of the Si-H bond of cross-linking oligomers to the vinyl groups, forming $Si-CH_2-CH_2-Si$ linkages [Campbell99]. This process is referred to as hydrosilation of the double bonds. The multiple reaction sites on both, the base and crosslinking oligomers allow for three-dimensional crosslinking of the PDMS. One advantage of this type of addition reaction is that no waste products such as water are generated. Note that heating will accelerate the crosslinking reaction (see above).
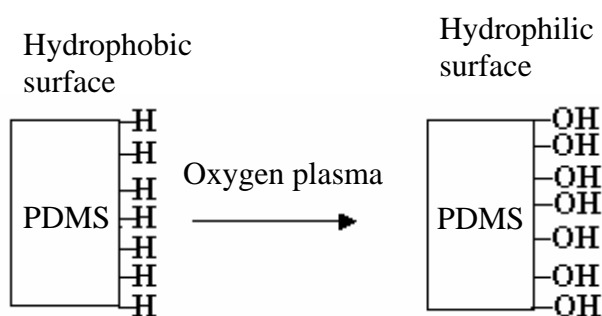

Figure 3.10: Modification of a PDMS surface by an oxygen plasma. The hydrophobic surface of the PDMS is converted to hydrophilic surface (oxidized).

Using a PDMS stamp has an important drawback in µCP. If the ink has a polar nature (alkanethiols are very little polar), it does not wet the PDMS stamp and therefore drying inked stamps leads to inhomogeneous patterns. Surface hydrophilization of PDMS is needed for successful inking. A simple way is to expose PDMS stamp surface to an O_2 plasma in order to oxidize the PDMS stamp surface (see Figure 3.10) [Xia98]. As a result, the surface is converted to a hydrophilic state, which corresponds to a glassy silica layer on the stamp. This layer has to be conserved by contact with water. Hillborg and coworkers were able to show the reason: By using X-ray photoelectron

spectroscopy they confirmed the formation of a hydrophilic silica-like surface layer (SiO_x-silicon bonded to more than two oxygen atoms), with a thickness of a few nanometers (3-10 nm) [Hillborg98]. After a relatively short period of time, typically from hours to a few days, the PDMS surface regains its initial hydrophobicity, a process often referred to as 'hydrophobic recovery'. It is widely accepted that migration of low molar mass oligomers of PDMS (short uncrosslinked PDMS chains) plays an important role in this gradual change of the surface properties [Hillborg98]. There are ways to overcome the problem: In order to preserve the hydrophilic character of the PDMS surface for a long time after O_2 plasma exposure, Donzel et al. functionalized the PDMS stamp surface by covalent linkage to modified poly(ethylene glycol) (PEG) [Donzel01], which is supposed to block the migration of low molar mass oligomers from the bulk to the surface of PDMS.

3.5 Electron Beam Lithography

Using a beam of electrons to generate patterns on a surface is known as electron beam lithography (EBL) [Runyan90]. EBL is one of the most promising nanolithographic technique used in nanofabrication and nanoscale research. A focused beam of electrons (generated by a scanning electron microscope (SEM)) is scanned in selected patterns (see below for details) on a substrate surface; in this way, material deposition on (or removal from) the substrate is achieved. In contrast, optical lithography uses light for the same purpose. EBL offers higher patterning resolution than optical lithography because of the shorter wavelength of the 20-50 keV electrons used in the pattern generation. Generally, the substrate must be coated with a resist that acts as mask for further modification, e.g. metal deposition from the gas phase. A very well known resist is poly(methylmetacrylate) (PMMA), spun on the substrate (see Figure 3.11), whose molecular weight is reduced by the electron irradiation wherever it impinges. This translates into a locally increased

solubility in an appropriate developing solution. The exposed region is thereby selectively removed [Runyan90].
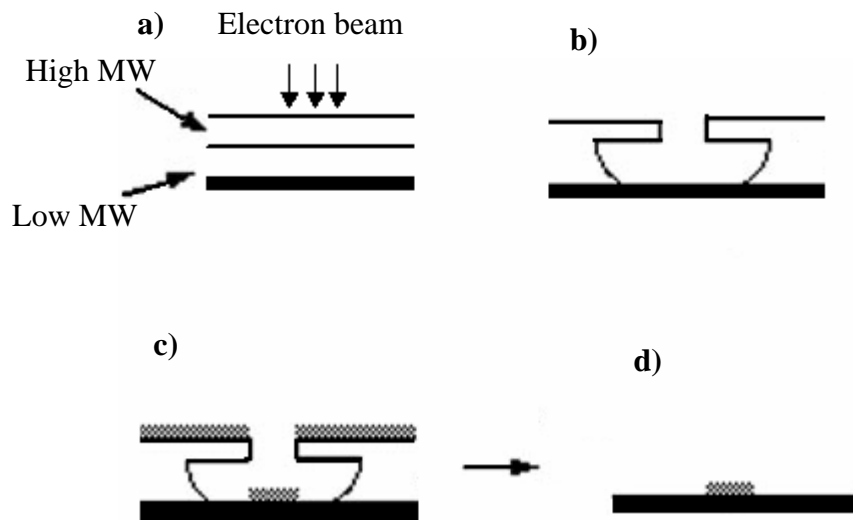

Figure 3.11: The steps for applying metal contacts to a SiO_2 surface (200 nm thick layer on a Si wafer) by EBL. **(a)** High molecular weight PMMA is spin coated on top of a slightly more sensitive bottom layer of low molecular weight PMMA (thickness~100-150 nm) and then exposed to the electron beam. **(b)** The PMMA is developed (locally dissolved) in methylisobutylketone (MIBK), giving a slight undercut. **(c)** Metal evaporation (Cr/Au or Cr/AuPd) on the developed structure. **(d)** 1-methyl-2-pyrrolidone is used to remove the entire PMMA layer (lift-off) [Runyan90].

In order to generate reliable patterns by EBL, layers with different molecular weights of PMMA can be used: The first layer (low molecular weight, contacting the substrate) has higher sensitivity to the electron beam, so during development a larger part of it is removed, producing a wider undercut in the exposed area. Therefore, in the later step (lift-off), the PMMA layers below the deposited metal layer can be easily removed by diffusion of solvent molecules from the exposed region to the PMMA layers (see Figure 3.11).

In the following, the contact structures will be explained in some detail. Figure 3.12 shows computer-generated electrode structures produced by the aforementioned electron beam lithography

processes. Note that the large electrode pads are used for (macroscopic) wire bonding, which provides a connection from the inner, small contacts to any external device (such as an electrical transport measurement circuit). A very thin metal (Cr or Ti) layer (~1-2 nm), evaporated just before exposure to Au or AuPd vapor, is used to increase the adhesion between the SiO_2 and the contact metal electrodes. The actual working area on the chip is the region shown in Figure 3.12b in which 8x8 coordinate markers are distributed.
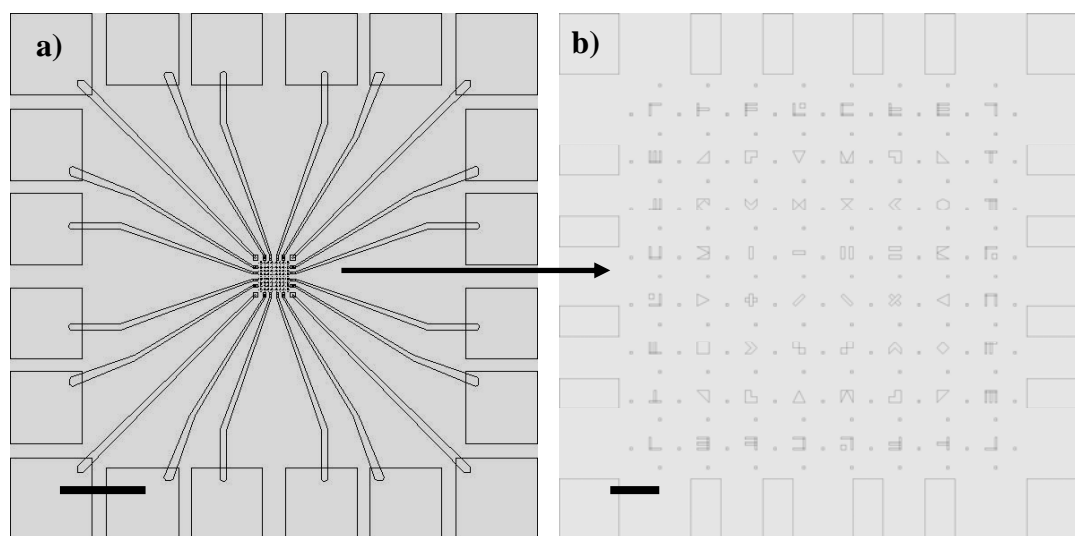

Figure 3.12: Computer-generated images of an electrode pattern for contacting TMV particles. **(a)** Large-scale view of pattern with 20 bonding pads (scale bar: 200 µm). **(b)** Zoom-in of the pattern in the central region (scale bar: 10 µm). The distance between two coordinate markers is 10 µm.

In order to contact nanoobjects (for example TMV particles), the objects can now adsorb in random distribution and orientation on the working surface (working area) of the specified chip (Figure 3.12b). Then the working surface is scanned with AFM in order to determine the coordinates of the adsorbed objects, measured relative to the coordinate markers. Patterns of the contacts were created with the software package called *Xfig*. The coordinates of the objects and of the contacts were transferred to the scanning electron microscope (SEM), which was used for electron beam exposure. Therefore, the beam only irradiates the regions predefined in the software package,

namely the contacts. The *Elphy* software package maintained the communication between the coordinates and the SEM by directing the electron beam.
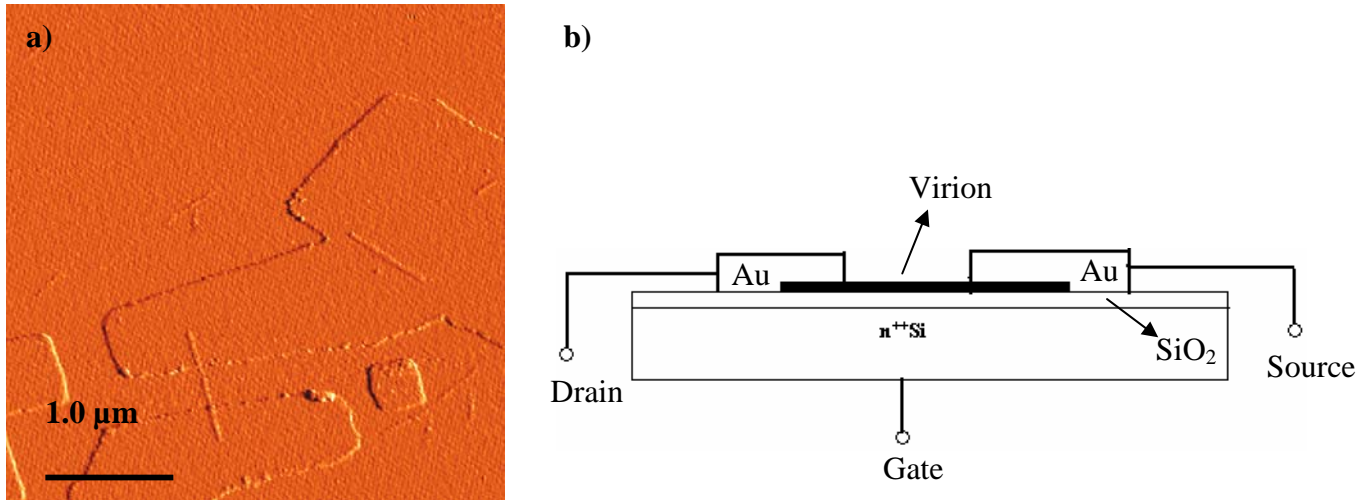

Figure 3.13: (a) AFM image (error mode) of a 900 nm long virion rod (3 TMV particles) embedded in two contacts on a SiO_2 surface. The electrodes are separated from each other by a ~500 nm wide gap. **(b)** Schematic illustration of the three-terminal metal-on-virion geometry used in the transport measurements.

During transport measurements on virions, only one configuration of the contacted virions has been used, Figure 3.13. Gold electrodes were created at the ends of TMV rods adsorbed on a SiO_2 chip surface, and employed for standard three-terminal measurements in the transistor configuration: One electrode (the drain) is biased with a voltage V_{ds}, and the current passing through the second electrode (the source) to ground is measured [Runyan90]. At the same time, the electrostatic potential at the TMV rod can be modulated by a third electrode (the back gate), which is 200 nm below the SiO_2 surface.

3.6 Cathodoluminescence

The band theory of solids dictates that materials can be classified according to their electron energy levels as insulators, metals, and semiconductors [Kasap00,Kittel53]. Insulators have a large forbidden gap between the energies of the valence electrons (forming the valence band (VB)) and the energy at which the electrons can move freely through the material (forming the conduction band (CB)). On the contrary, metals are unique as good conductors of electricity because of overlap between VB and CB; thereby VB electrons can move freely. In semiconductors VB and CB are separated by a gap of energy E_g (e.g. 1.1 eV for Si), Figure 3.14.

By irradiating a semiconductor with energies greater than its E_g, electrons can be excited from VB to CB, thereby generating electron-hole pairs. The excited electron then ''thermalizes'', it looses some energy to lattice vibrations (phonons). When it recombines with the hole, photons can be emitted; their energy is characteristic for the material of interest. This process of emission of light by an electron-hole recombination is called luminescence, Figure 3.14. When the electron-hole pairs are excited by electrons of a certain energy range, the process is referred to as cathodoluminescence (CL) [Kasap00]. The photons can be collected by a mirror and analyzed by a spectrometer, both of which installed in a transmission electron microscope (TEM) or a scanning electron microscope (SEM). The analysis is performed over the specimen area of interest, defined by the electron beam, and is therefore highly localized, in contrast to conventional photoluminescence.
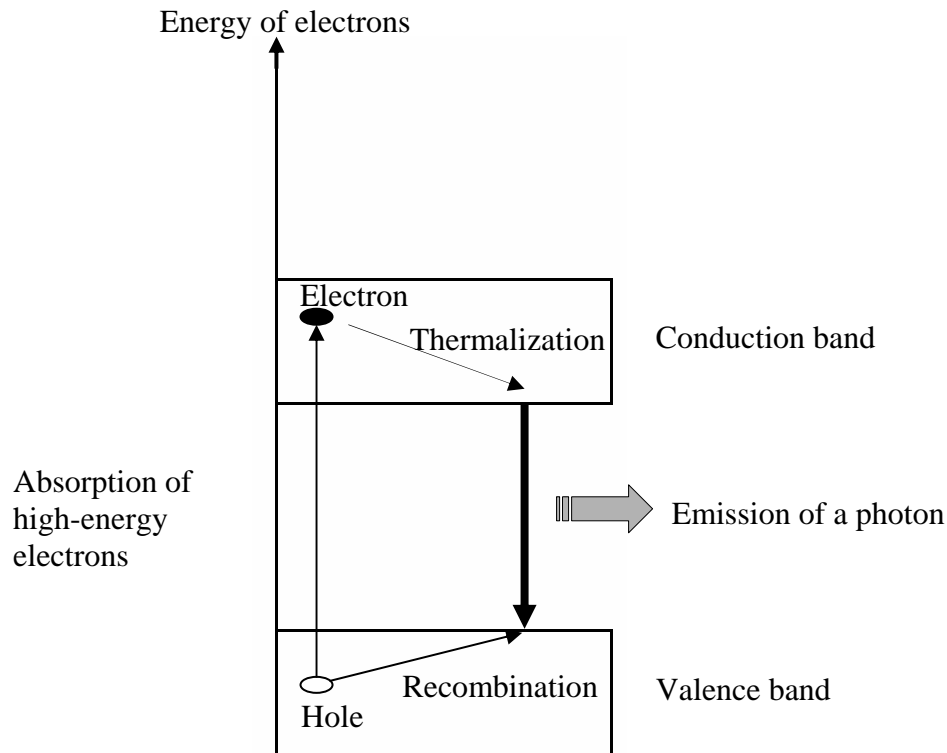
Figure 3.14: Emission of a photon by an electron-hole pair in a semiconductor material (luminescence). In photoluminescence, an absorbed photon creates an electron-hole pair, while in cathodoluminescence, an absorbed electron (100 eV to 10 keV) excites the electrons. In both cases, the hole is in the valence band (VB), the excited electron resides in the conduction band (CB), and their recombination causes emission of photons.

In this work, a SEM with a heated field emitter (FE-SEM) was used for all CL measurements, and the sample temperature was adjusted to a few tens of K. The advantages of a field emitter are the high spatial resolution and the relatively high current density. The latter is needed in order to excite electron-hole pairs at a large density, which means that small sample volumes (nanoobjects) suffice for detection. However, the volume is strongly dependent on the electron energy; at 3 kV, the spatial resolution of the microscope is ~100 nm. For coupling out the CL, a glass fiber was used. The glass fiber can be positioned 50-100 μm from the incident point of the electron beam. High collection efficiency, comparable to conventional mirror optics (fixed configuration), is achieved in

this configuration since the working distance can be controlled. The glass fiber guides the CL signal

to the detection system with a spectral resolution down to ~0.1 meV.

CHAPTER 4

Mineralization of TMV for Metal Nanostructures

In this chapter, the capability of Tobacco Mosaic Virus (TMV) as a bionanotemplate for the synthesis of a variety of metal nanostructures by using electroless deposition (ELD) methods is described. The functionalities of TMV particles, because of the unique amino acid sequence of the coat protein (discussed in chapter 2), can offer a wide variety of nucleation sites for surface controlled metal deposition on the inner and the outer surface as well as at the ends of TMV particles. New ELD baths compatible with virions have been developed in order to synthesize nanowires within the central channel of the virions. ~3 nm diameter copper, nickel, and cobalt-iron alloy nanowires have been achieved within the central channel of the TMV rods. High-resolution transmission electron microscopy (HRTEM) investigation of the nickel nanowires inside the TMV is also explained. In addition, 6 nm gold nanoparticles (Au-nps) have been selectively attached to the ends of the TMV rods. These Au-nps have been further size-enhanced and dumbbell-shaped structures have been fabricated. The mechanisms of all the mineralization experiments are discussed in detail. A special section describes the chemical composition of the deposited materials (Section 4.6).

4.1 Introduction

The fabrication of nanostructures with well defined chemical composition and structure is very important in the growing field of nanoscience. Nanochemistry, the synthesis and study of well-defined structures with dimensions of 1-100 nm, seeks to find ways of synthesizing nanomaterials with different techniques. In this regard, the design and construction of nanoscale structures using biological molecular templates is an emerging research field of nanochemistry. The use of biological molecules, assemblies and systems as templates in the synthesis of nanomaterials offers new and exciting alternatives to conventional synthetic strategies. Sometimes the fabricated nanomaterials are difficult or impossible to obtain by using other means. Biological templates, such as DNA [Braun98,Monson03], Tobacco Mosaic Virus (TMV) [Knez04,Shenton99], bacteriophages [Mao04], and protein fibers [Mertig98] have been successfully used to guide the deposition, assembly, and patterning of inorganic nanomaterials. Genetic engineering strategies have been also used to enhance or alter the affinities of specific biotemplates for inorganic materials [Whaley00]. Mineralization of tubular biological templates has resulted in a range of nanotubular inorganic-organic composites [Shenton99]. Mineralization is here defined as either the formation of metals (or metal alloys), or of components containing metal cations and nonmetal anions. In this process, an organic substance is coated or decorated with an inorganic substance and thus forms an inorganic-organic composite. In the case of biomineralization, living organisms form materials from bioorganic and inorganic solids, for example, the iron mineral magnetite (Fe_3O_4-varying in size from 50 to 100 nm in magnetotactic bacteria) [Baeuerlein00].

The electroless deposition (ELD) method enables mineralization of several biological templates [Mertig98]. By means of ELD, a variety of interesting materials can be deposited on nonconductive surfaces without applying an external current to the deposition system [Schlesinger00]. Applications of ELD on biological molecules have resulted in a new way of synthesizing nanomaterials [Knez04]. One of these biological templates is TMV (see chapter 2 for details). The

protein shell of the virus provides highly promising scaffolds for the fabrication of new materials. Kausche and co-workers published the first work in 1939, in which they demonstrated that gold colloids can adsorb on the exterior surface of TMV particles [Kausche39]. Thereafter, inorganic nanomaterials have been fabricated using TMV as a bionanotemplate [Knez04,Dujardin03,Shenton99]. Instead of genetic modification of the TMV, chemical modification can also install new functional groups, which expands the range of applications of TMV in the fabrication of nanomaterials [Schlick05].

ELD (see also chapter 3) is widely used in electronic packaging for selective metal deposition [Schlesinger00]. The major components of an electroless deposition solution are metal ions in a suitable oxidation state, a complexing agent, a reducing agent and a buffering agent [Diamand95,Schlesinger00]. Some ELD solutions contain additional ingredients (e.g., surfactants) in order to achieve the desired quality of the deposited material. The buffering agents, controlling the pH during ELD, are very important because a very high or low pH values can denature biological templates such as TMV [Zaitlin00]. In addition, ELD is highly pH-sensitive, often with a maximum of the rate obtained at certain pH values. The complexing agent, preventing random deposition of the metal ions in the solution, changes the electrochemical reduction potential of the corresponding metal ions and determines the kinetic stability of the ELD solution. The reductant reduces the metal ions from the ELD solution to the metallic state. ELD occurs by an autocatalytic redox process, which means that the deposited metal catalyzes its own deposition. However, the deposition usually requires initial presence of noble metals: "activation" creates noble metal clusters on nonconductive surfaces. Selective deposition of materials can be achieved either by selective passivation of a catalytic substrate [Bittner02] or by selective activation of a nonreactive surface by a noble metal catalyst [Putten93]. The details of this pretreatment are not yet known even though some theoretical studies exist [Nakai01,Mertig02]. Recently, Seidel and co-workers have found that a long incubation of DNA molecules with Pt(II) complexes is necessary to obtain a template-directed formation of thin, uniform and long cluster chains after chemical reduction of the

DNA-Pt (II) solution [Seidel04]. Therefore, the steps followed in the pretreatment process affect the final shape of the deposited material on the template.

Here, we explain selective deposition of a variety of materials such as cobalt, nickel, copper, iron, and gold within the central channel, on the outer surface as well as at the ends of the TMV particles using ELD methods. In this project, energy-filtering transmission electron microscopy (EFTEM) was used as the main analysis tool for the chemical mapping of inorganic nanowires in and at TMV. In addition, X-ray microanalysis (EDX) in conjunction with conventional TEM attachment was used for chemical analysis of size-enhanced gold nanoparticles attached to the ends of TMV particles. Transport properties of a TMV rod, which is the first step towards electrical characterization of the nanowires inside the virus, were also explored.

The electrical, optical and magnetic properties of the synthesized materials are of interest, because few such structures have been synthesized. Cobalt, nickel and iron (the later codeposited with cobalt) are important in terms of magnetic properties; however gold, and copper are show interesting optical properties (e.g. field enhancement in nanooptical devices). Moreover, the low electrical resistivity of copper could be a valuable property. Presently, integrated chip industry uses copper for the fabrication of connecting wires (~100 nm wide) in integrated circuits since they show higher resistance to electromigration and stress-induced voiding, and a lower resistivity than aluminum [Andricacos98,Diamand97]. However, it has been anticipated with theoretical calculations that the resistivity of the copper nanowires should increase with decrease in the diameter (narrow-line resistivity increase (NLRI)) [Diamand03]. The NLRI effect should become dominant below 50 nm, which has not been measured in detail yet. Even more interestingly, when the size of the nanomaterials is smaller than the Fermi wavelength, the energy levels are quantized with values directly related to the size of the nanomaterials under investigation (an effect called quantum confinement) [Alivisatos96]. Therefore, there are certain critical sizes below which fundamental electrical, optical, and magnetic properties of nanomaterials change substantially, e.g.

class of ferromagnetism, ohmic conductivity, an energy shifts for luminescence. These critical scales are not known especially for 3 nm wide nanowires. In this chapter, being able to deposit a variety of materials to TMV particles, we demonstrate that TMV is a suitable template for the synthesis of a variety of nanomaterials.

4.2 Experimental Part

Synthesis of nanowires. Before the mineralization of TMV, the virus was first activated with an aqueous Pd (II) solution. 500 µl of a 0.2 mg/ml TMV suspension in water was incubated with an equal volume of a freshly prepared aqueous 1.36 mM Na_2PdCl_4 (Aldrich 99,998%) solution with an excess (1M) NaCl (Merck p.a.≥99, 5%) (the pH of the solution was around 5). After 10 min, the suspension was centrifuged for 10 min at 14000 rpm, producing a pale brown pellet. The supernatant was removed and the pellet was resuspended in water. Pd (II)-incubated TMV suspension was metallized with copper by treating the virus suspension with the corresponding copper electroless deposition (ELD) solution for 20 – 30 min. For this purpose, a new copper ELD solution was developed in order to metallize TMV with copper at pH~7.5, based on a formulation described by Jagannathan et al. [Jagannathan93]. Pd (II)-incubated TMV suspension was mixed with an equal volume of a solution containing 0.032 M $CuSO_4.5H_2O$ (Sigma 99,999%), 0.04 M EDTA (ethylenediaminetetraacetic acid disodium salt, Aldrich), 0.05 M TEA (triethanolamine, Janssen Chimica 97%) and 0.067 M DMAB (dimethylamine borane, Aldrich 97%) in water (the pH of this solution was around 7.5).

For the nickel wire synthesis, the Pd(II)-incubated TMV suspension was mixed with an equal volume of a solution containing 0.18 M $Ni(CH_3COO)_2.4H_2O$ (Aldrich 98%), 0.23 M lactic acid (Aldrich 95%) and 0.067 M DMAB (Aldrich 97%) [Mertig98,Knez04]. For rate measurements in absence of TMV, a copper plate with a total area of 26.5 cm^2 was used. Another Ni-ELD bath was

also employed. The bath contains 0.032 M $NiSO_4 \cdot 6H_2O$ (Merck 99%), 0.087 M Ammoniumhydrogencitrate (Aldrich 98%), 1.25 M Ammoniumchloride (Merck 99.8%), and 0.067 M DMAB. The pH of both Ni-ELD baths was adjusted with 1 M NaOH (Merck 99.0%) to around 7. For the cobalt metallization, the Pd (II)-incubated TMV suspension was mixed with an equal volume of a solution containing 0.14 M $CoSO_4 \cdot H_2O$ (Aldrich), 0.15 M sodium succinate (Aldrich 99%) and 0.067 M DMAB [Mertig98]. The cobalt bath was used as it is, i.e. without adjusting the pH of the deposition solution. In order to synthesize CoFe alloy nanowires, 0.02 M $FeSO_4 \cdot 7H_2O$ (Fluka Chemie) was added to the cobalt bath and metallization was done as in the case of cobalt metallization. The bath was used without adjusting the pH. After addition of an iron compound, a small amount of precipitate (presumably iron(II)-succinate) was observed. This precipitate may act as a nucleation center or uncontrolled material deposition during the ELD reaction. Therefore, the bath was filtered with a filter paper before use in mineralization of TMV.

For all reactions, after an induction time of 10 to 15 min, gas bubbles and thin metal layers on the internal surface of the reaction vessel (indication of the success of the ELD reaction) were observed. All mineralization experiments were carried out at room temperature and in air. One can assume that the solutions, which have a relatively small volume in the ml range, are nearly saturated with oxygen. Note that dissolved oxygen in the deposition solution can affect the deposition rate of the materials (see e.g. Kind et al. [Kind98]). Water was purified with a Millipore Milli-Q to 18.2 $M\Omega cm$ with total organic contamination (TOC) most of the time lower than 5 ppb. All the glasswares were cleaned in Nochromix® (Godax Laboratories, Inc., New York) solution prepared in H_2SO_4 (BASF 96%).

TMV isolation. A Plasmid-DNA was employed to mechanically infect *Nicotiana tabacum* cv. Samsun nn plants. 4 weeks post inoculation, systemically infected leaves were harvested and stored at –20 ^{0}C. Two methods were employed to isolate the virus, including centrifugation in CsCl or sucrose gradients, yielding 6 mg TMV /g plant material. TMV suspensions were stored at 4 ^{0}C. In

some cases water was replaced with Na_2HPO_4/KH_2PO_4 buffer (pH =7, ''Na/K buffer'') (see also details in ref. [Knez04]). Water was purified with a Barnstead Nanopure apparatus to 18.2 MΩcm. The virus suspension was dialyzed before metallization using Slide-A-Lyzer 10000 MWCO units (KFM, Lohmar).

Selective binding and size-enhancement of gold nanoparticles. In order to adsorb Au-nanoparticles (Au-nps) to the ends of the TMV particles, 2 µl of TMV suspension from a 10-mg/ml stock suspension was diluted with 800 µl water. 200 µl commercially available 6 nm Au sol (AURION, Wageningen-The Netherlands) from the stock solution (0.8 mg/ml) was added to the diluted TMV suspension. The TMV-Au-np suspension was incubated overnight at room temperature.

Au-nps were selectively size-enhanced using the method developed by C. J. Murphy and coworkers [Jana01]. First, the TMV Au-np suspension was adsorbed (a droplet dried with a filter paper) on various surfaces (an oxidized silicon surface and a carbon coated Cu-TEM grid surface). For the size-enhancement of 6 nm Au-nps, an oxidized silicon substrate containing Au-nps together with the virions was immersed into the gold deposition bath, consisting of 150 µl of 0.06 M cetyltrimethylamonium bromide (CTAB) (Fluka, 99.8%), 200 µl of 0.25 mM $HAuCl_4 \cdot 3H_2O$ (Aldrich) and 10 µl of 0.1 M L (+) ascorbic acid (Merck) were used. The pH of the reaction solution was adjusted to 4 with 0.01 M NaOH in order to prevent disassembly of TMV coat proteins.

In order to remove RNA from the TMV particles with RNAase (Sigma), 4 µl of 10mg/ml TMV suspension was diluted to 1000 µl. At 37 ^{0}C, 1 µl of 10mg/ml RNAase was added to the diluted virus suspension. After 30 min, the RNAase treated TMV suspension was centrifuged at 14000 rpm and the supernatant was removed. The pellet in the reaction vessel was suspended in 800 µl water and mixed with 200 µl 6 nm gold sol (0.8 mg/ml).

Proteinase K (Genaxxon BioScience), which cleaves peptide bonds in proteins (''digesting''), was used for disassembling the coat protein of the TMV particles. 10 µl TMV (10 mg/ml) suspension

was mixed with 90 µl of Proteinase K (100 µg/ml) in 0.1 M Tris buffer (Tris (hydroxymethyl) aminomethane (Fluka, 99.8%)) at pH of 8.3 for 2 hours. For testing Au np attachment, 200 µl of 6 nm gold sol (0.8 mg/ml) were added. Alternatively, in order to remove the coat protein around the nickel nanowire within the central channel, metallized TMV particles were adsorbed on carbon-coated Cu-TEM grid. Subsequently, the grid was incubated for 30 min in the same enzyme solution.

Substrate preparation. Silicon wafers (100 orientation, MEMC Electronic Materials) were cut into 3x3 mm pieces with a wafer saw. The wafers were sonicated for 15 min in acetone (Roth Rotipuran, 99.8%) before the surface of the wafer was terminated with hydroxyl groups by standard RCA procedure [Kern90]: 15 min immersion into a 1:1:5 (vol.) mixture of 25% NH_4OH (VLSI Selectipur, Merck), 30% H_2O_2 (VLSI Selectipur, Merck) and water, followed by 15 min immersion into a 1:1:5 (vol.) mixture of 37% HCl (Suprapur, Merck), 30% H_2O_2 and water. All experiments were performed under sonication at 70-80 C^0.

Sample preparation. In order to analyze the samples in the transmission electron microscope (TEM), 10 µl of the metallized TMV suspension was deposited on ethanol-rinsed (Roth Rotipuran) Formvar/carbon-coated copper grids (300 or 400 mesh, SPI-Supplies) and air-dried. The 10 µl samples were taken during the mineralization of the TMV particles with the corresponding ELD bath.

Instrumentation. Most of the transmission electron microscopy (TEM) experiments were performed on a Philips CM 200 operated at 200 kV. The microscope is equipped with a LaB_6 filament. Atomic force microscope (AFM) images were obtained with a Thermomicroscopes Autoprobe M5, operated in non-contact and intermittent contact mode, with MikroMasch NSC11 cantilevers or NCHR Pointprobe Nanosensors. UV-Vis spectra were obtained with a UV-Vis Spectrometer Lambda 2 (Perkin Elmer).

Elemental mapping experiments were performed on a Zeiss 912 and a LIBRA 200 FE energy-filtering microscopes (both from Carl Zeiss NTS). The Zeiss 912 is equipped with a LaB_6 filament and a magnetic omega-type energy filter, and it is operated at 120 kV (see chapter 3 for details).

Bright-field (conventional) TEM images for 6 nm gold nanoparticles attached to the ends of TMV particles and for size-enhanced gold nanoparticles were obtained in a Philips CM 200 microscope operated at 200 kV. All elemental mapping of Ni, Co, and Cu within the virus central channel have been performed with the Zeiss 912. The LIBRA 200 FE, which was used for elemental mapping of CoFe, and pristine TMV particles, is equipped with a highly efficient field emission electron source and a corrected omega-type energy filter (90° corners in the energy filter). EDX experiments were performed with the LIBRA 200 FE microscope, using an EDX detector (EDAX) for analyzing the X-rays emitted from the sample surface. In addition, a scanning transmission electron microscope (VG HB 501 UX) operated at 100 kV was used. The microscope is capable of forming an electron probe with a size of less than 1 nm, so it has a higher spatial resolution for analytical measurements, when compared to the Zeiss 912. Unfortunately, the high electron beam current density caused radiation damage at the nanowires, so the results are omitted here.

Elemental mapping. In order to obtain an elemental map from a region, firstly an electron energy loss (EEL) spectrum was acquired. In a typical EEL spectrum, three principle regions are important. The first region contains the zero-loss peak (at 0 eV), which consists mainly of elastically forward-scattered electrons. The second region is the low-loss region up to an energy loss of ~50 eV (plasmon losses), containing electrons that have interacted with relatively weakly bound outer-shell electrons of the specimen atoms. From the low-loss region, elemental information can be obtained because each element has specific plasmon energies, for example iron, cobalt, and (amorphous) carbon 23.0 eV, 20.9 eV, and 24.0 eV, respectively [Egerton96]. However, this is more conveniently obtained from the last region (Figure 4.9), the high-loss region from ~50 up to ~1000 eV, where electrons interact with the very tightly bound (core) electrons, giving direct chemical information.

Element	Pre-edge energy1 (eV)	Pre-edge energy2 (eV)	Post-edge energy (eV)	Edge energy (eV)	Slit width energy (eV)
Cu	841	901	961	931	40
Ni	775	820	885	854	40
Co	699	749	804	779	40
Fe	638	678	733	712	40
C	239	269	299	284	30
N	353	383	416	401	30
O	477	512	552	532	30

Table 4.1 Pre-edge, edge and post-edge energies of the elements used for elemental mapping with the three-window technique.

Based on the edge energies in the EEL spectrum, elemental maps can be obtained. Firstly, two pre-edge images, and a post edge image are recorded, each exclusively with electrons of the specified energies (see Table 4.1). This so-called three-window technique was used for the edge background (intensity vs. energy curve) calculation (see also chapter 3 for background estimation in elemental mapping) [Williams96]. The pre-edge images allow fitting a simple power law, and the post-edge image contains the chemical information, namely intensity that is above the intensity-energy background curve. The corresponding pre-edge and post edge energies for the elemental map calculation for each element are tabulated in Table 4.1. For example, a nickel map was recorded with two pre-edge images and a post-edge image at 775, 820, and 885 eV, respectively.

All data were acquired using a Gatan slow-scan CCD camera with 1024 x 1024 pixels (in some cases 512x512 pixels) and a pixel size depending on the magnification of the microscope. For the experiments, a window size of ~50 eV, binning 2x, an objective aperture of 60 µm and an exposure time of 60 seconds (sometimes 30 and 120 seconds) were used. All EEL spectra and EFTEM images/maps were acquired with the *Digital Micrograph* software package, which also allowed to remove artefacts (very intense spots) in the spectra using the 'point blemish' function. It is common to present line profiles across structures, which are in fact averages of several lines in a digitital image. Averaging of 12 lines of 40 pixels each, corresponding to a 20 nm x 60 nm box area (perpendicular to the nanowire axes), was used for calculating line profiles of 60 nm length.

Electron beam lithography and I-V measurements. The details about electron beam lithography processes are given in chapter 3 and chapter 6. TMV particles were adsorbed on a silicon substrate (a chip), which is patterned with gold markers. The locations of the TMV particles were determined with respect to these markers by AFM scanning of the surface. Knowing the locations of the TMV rods on the surface, electrodes were drawn to the ends of the TMV rods in a graphic program (*Xfig* software). The chips were then covered with polymethylmetacrylate (PMMA). In order to increase the effectivity of the lift-off process, a layer of PMMA with a higher molecular weight was spin coated on top of a slightly more sensitive bottom layer of lower molecular weight PMMA. Further details about *lift off* and *development* processes are given in chapter 6. In short, the resist layers were dried at room temperature without annealing at 160 ^{0}C (thickness~100-150 nm). A chromium layer was deposited in order to increase the adhesion of gold electrodes to the silicon oxide surface. Finally, the gold electrodes contacting the TMV rods on the silicon oxide surface were obtained. During the I-V measurements, a Keithley 2400 SourceMeter® as a voltage source, a Keithley 2000 Multimeter as a voltage measurement instrument, and an I-V converter from the DL Instrument were used.

4.3 Deposition of Copper

For future nanoscale devices such as atomic-scale switches, very small interconnects (< 10 nm) will be required. In case that metal structures are searched for, templated copper wires might be a significant advance for nanoscale integrated circuit manufacturing. The ability to generate copper nanowires from TMV templates could furthermore facilitate the transition from top-down lithographic fabrication techniques, which presently use copper, to bottom-up techniques. Although copper is a metal presently used to produce connecting wires in integrated circuits, the TMV templated production of copper nanowires is not a all straightforward because the standard formaldehyde-based high pH level ELD solutions [Schlesinger00] destroy the virions. The required

pH for this process is above 12. In order to deposit copper within the central channel of the TMV, the TMV was incubated in Pd (II) aqueous solution. Otherwise no deposition of copper was observed (Chapter 4.2). The surface chemistry of the TMV is crucially important: In the case of virions stored in phosphate buffer, TMV suspension is dialyzed against water prior to usage. Otherwise, due to the adsorbed phosphates, metallization would occur on the external surface of the virions [Knez04].
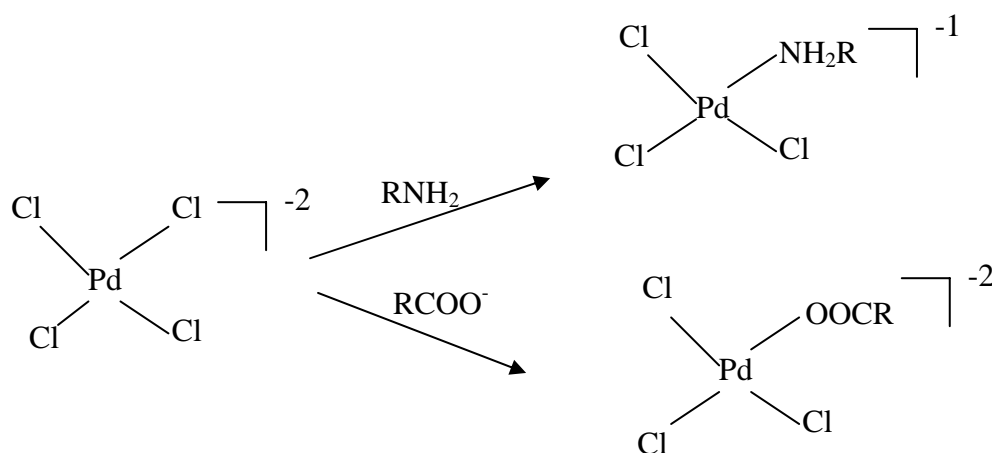
Scheme 4.1: Coordination of $PdCl_4^{-2}$ to amines and carboxylate [Kind98,Mackay96].

Our activation solution contains only Na_2PdCl_4 (1.36 mM) and excess NaCl (1 M) at pH 5, aiming to deposit metals within the hollow channel of TMV particles. Excess NaCl is very important in order to avoid formation of palladium oxo and hydroxo complexes [Kind98]. These complexes are favored if the pH value is above 2, and the chloride concentration is very low. In order to initiate deposition of metals within the central channel of TMV, the palladium complex (or palladium oxo or hydroxo complex, if sufficiently small) has to reach the central channel of the virion. It cannot bind electrostatically to the negatively charged channel. Nevertheless, it might form complexes with amine and carboxylic groups of the amino acids, covering the interior channel (see chapter 2 for the details), even if the residues contain positively charged protonated amine groups [Kind98]. Scheme

4.1 illustrates the complex formation of $PdCl_4^{-2}$ with carboxylate and amine functional groups. Here the carboxylate and amine functional groups donate electrons to the electron deficient Pd(II) and form complexes [Mackay96]. Furthermore, Pd(II) can coordinate with the phosphate groups present in the backbone of RNA molecules [Mori02]. For example, at the ends of the TMV particles, RNA is accessible to Pd(II) ions (see also chapter 2 for the structure of TMV).

Prior to the ELD of the metals, the Pd(II) species have to be reduced by the reductant dimethylamine borane, DMAB, present in the solution since only Pd^0 can act as a catalyst for ELD, but not Pd(II). Since small palladium (or platinum) clusters down to a few atoms in size are catalytically active [Kind98,Mertig02], the metal deposition can not only be confined to the viral channel, but also be so effective that the channel is filled with a wire instead of separate clusters. After reduction of the palladium ions in TMV suspension with hypophosphite, no palladium clusters have been detected within the central channel [Knez04b], which probably means that the formed clusters were < 1 nm. In fact, very small palladium clusters (1 to 4 nm) have been observed on the exterior surface of the TMV particles [Knez04b]. However, a single cluster (nucleating center) can also produce a wire within the channel of the virus since ELD is an autocatalytic process [Schlesinger00].

In order to deposit copper, we tested conventional formaldehyde-based high pH level ELD solutions [Schlesinger00]. The actual reducing agent in this plating process has been shown to be the methylene glycolate anion formed by the interaction of formaldehyde with the hydroxyl ions in the plating solution [Tam85]. The methylene glycolate anion formation is favored at high pH levels (>12), which is needed for reasonable deposition rates for use in the industry. The requirement of high pH levels cause virion disassembly since TMV denatures at pH >9 [Zaitlin00]. However, Demir et al. [Demir03] have reported the photo-reduction of copper at the surface of TMV particles at pH 6.5. The number of copper particles incorporated per virion (external surface) was very low and the particles were not monodisperse. Deposition of copper to other biotemplates such as DNA

is also very difficult. Copper nanowires of ~3 nm in diameter and 10 nm in length have been synthesized using surface-adsorbed DNA as a template; the surface-adsorbed DNA molecules were first incubated in copper (II) aqueous solution and then reduced by ascorbic acid. However, one has to repeat the process several times in order to increase the diameter of the copper nanowire [Monson03]. This process is very difficult to perform because some copper (II) complexes can cleave DNA molecules via oxygen-based radicals, making impossible to obtain long copper nanowires along the surface-adsorbed DNA molecules [Routier97]. The same conditions were tried for depositing copper to TMV particles. Nevertheless, the process did not yield any copper deposit.
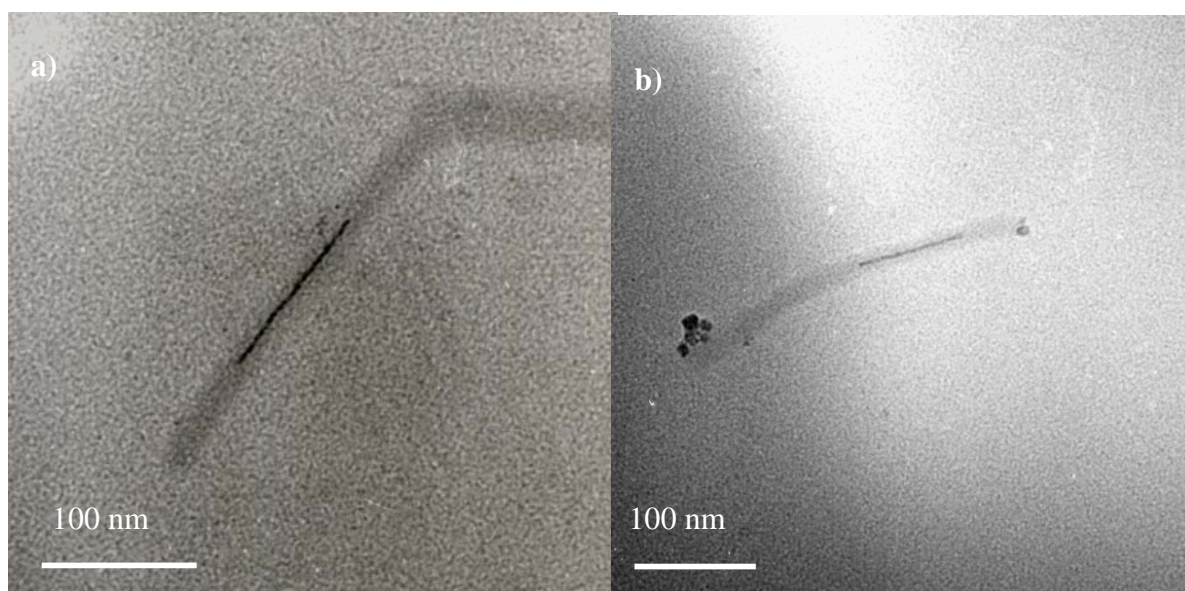
Figure 4.1: TEM micrograph of copper nanowires within the central channel of TMV particles. **(a)** The dark line corresponds to a copper nanowire, 3 nm in diameter, and 115 nm in length. The wire is surrounded by a dark-grey region, the viral coat proteins of a single virion. The mineralized virion is attached from its one end to two side-to-side assembled virions (right, top). **(b)** A 85 nm copper nanowire (dark line 3 nm in diameter) within the central channel of a virion. Several copper nanoparticles (dark discs) have formed close to the ends of the virion.
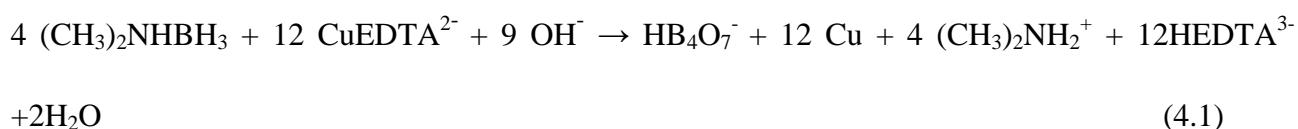
The best approach turned out to be again ELD. For this, the low pH level ELD copper solutions described by Jagannathan et al. were slightly modified [Jagannathan93]. Instead of multidentate nitrogen donor ligands, EDTA was used as the complexing agent. EDTA is a strong complexing agent, which is essential to keep the copper ion in the solution at this pH level (~7.5) and to reduce the possibility of spontaneous homogeneous decomposition (bath decomposition) [Schlesinger00]. The other ingredients in the process were copper sulfate as the metal ion source, triethanolamine as the buffering agent, and DMAB as the reducing agent. Triethanolamine (TEA) inhibits the change in pH of the ELD bath during the deposition of copper since it is a good buffering agent at pH around 9. It has been claimed that when EDTA is used with TEA, substantial improvements in the stability of the deposition bath can be observed at pH 9 [Jagannathan93]. In this case, it was suspected that mixed ligand complexes of Cu (II) with EDTA and TEA were formed. Another ingredient used in the ELD bath, DMAB, is a strong reducing agent and stable in neutral and alkaline media [Schlesinger00]. The pH change between 7 and 10 provides the optimal environment, in which TMV particles are not significantly affected (until pH 9).

After the usual activation procedure (see experimental part), the virions were suspended in the Cu ELD bath, whose pH was adjusted around 7.5. Copper deposited within the 4 nm-wide internal channel of TMV particles without denaturation. Fig.4.1a, and 1b show bright-field transmission electron microscopy (TEM) images of copper nanowires inside virions, ~3 nm in diameter. This experimental result (formation of very small diameter copper nanowire) also supports theoretical studies where molecular dynamics simulations have showed that freestanding ultrathin copper nanowires can maintain their structures at room temperature [Kang03]. Nevertheless, these simulations have been performed for vacuum conditions. At ambient conditions, the properties (i.e., structural) may differ substantially from the theoretical expectations. For example, since all the experiments are performed in an aqueous environment, oxidation of copper nanowires might happen. Indeed, Diamand et al. have shown that Cu(II) ions might also be reduced by formaldehyde to Cu(I) (Cu_2O) [Diamand95]. This transformation is noncatalytic and can proceed in the volume of

the solution and hence, causing solution decomposition and uncontrolled copper deposition (see Figure 4.1b, copper nanoparticles close to the metallized virus). In ambient condition, copper surfaces can be oxidized with the oxygen in air, leading to the formation of Cu_2O and later to a mixture Cu_2O and CuO [Barr78]. A thin coating (a few Å in thickness) on the copper surface can be expected after a day of exposure to the air [Kim04]. In the case of copper nanowires in the virus, we expect an even thinner coating (probably less than a monolayer of oxide) after a day of synthesis; indeed, oxygen in the air can diffuse through the coat protein of the virus and contact the nanowire. Previous studies have shown that oxygen molecules could quench the fluorescence of apparently buried tryptopohan side chains (penetrating in proteins) in a variety of proteins with surprising ease [Calhoun83]. All these arguments mean that the oxide must be taken into account when measuring the electrical properties of the copper nanowires, especially after releasing the nanowire, e.g. by enzymatic digestion of the coat protein.

In four separate experiments, it was observed that between 40 and 50 % of the TMV particles were metallized with copper nanowires, and the length of the nanowires varied from 5 nm to 150 nm. 300 nm long copper nanowire within the viral central channel has never been observed in the experiments. When complete metallization of a single virion (300 nm long) is assumed, then ~180000 copper atoms within the central channel of the virus would be obtained (copper density: $8920 kg/m^3$ and volume of a nanowire 3 nm in diameter and 300 nm in length: $2120 nm^3$).

The ELD of copper can be formulated as follows, assuming a complete oxidation of the borane [Pourbaix66,Burke92], and taking into account the various (de)protonation equilibria:

$$4\ (CH_3)_2NHBH_3 + 12\ CuEDTA^{2-} + 9\ OH^- \rightarrow HB_4O_7^- + 12\ Cu + 4\ (CH_3)_2NH_2^+ + 12HEDTA^{3-}$$

$$+2H_2O \tag{4.1}$$

The equilibrium is on the right hand side, hence ELD of copper is thermodynamically allowed (spontaneous reaction). Thermodynamics predicts equilibria in electrochemical reactions by using

the Gibbs free energy ΔG, expressed in terms of the cell potential E^0 in an electrochemical reaction (ΔG=-nFE^0) [Schlesinger00]. Only if ΔG has a negative value, the reaction is spontaneous. However, the kinetic barrier is high, so spontaneous deposition does not occur in the deposition bath [Schlesinger00] and catalysts such as noble metals (or copper) are required. The Pourbaix diagram for the system boron-water shows that $HB_4O_7^-$ is the dominant species at pH values from 7 to 9 at nearly all relevant redox potentials (from–1.0 V to 0.8 V) [Pourbaix66]. A deeper analysis is needed to figure out the role of each component in the equation 4.1. The reaction can be separated into two half reactions, cathodic reduction of copper ions and anodic oxidation of DMAB on a catalytic surface such as palladium for the first copper atoms to be deposited, or copper during ELD [Schlesinger00,Sverdlov05,Saito98,Burke92]. The reduction of the copper-EDTA complex

$$CuEDTA^{2-} + 2\ e^- + H_2O \rightarrow Cu^0 + OH^- + HEDTA^{3-} \tag{4.2}$$

requires potentials below -0.22 V_{SHE} [Schlesinger00]. Note that EDTA can capture positively charged copper ions in the solution since the formation constant of the copper-EDTA complex is very large (log K_f=18.8), thus free Cu^{2+} is practically absent in the deposition solution [Schlesinger00]. We assume that the oxidation of DMAB is described by the following equation

$$4\ (CH_3)_2NHBH_3 + 21\ OH^- \rightarrow HB_4O_7^- + 4\ (CH_3)_2NH_2^+ + 14\ H_2O + 24\ e^- \tag{4.3}$$
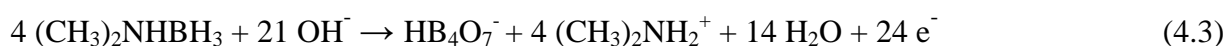
which is a two-electron process (per H atom of the borane) [Burke92]. Note that this equation does not suggest any mechanism. The mechanism of the anodic oxidation of DMAB has not been completely clarified and depends strongly on the pH value of the medium [Schlesinger00,Sverdlov05,Saito98,Burke92]. There appears to be general agreement that $BH_3(OH)^-$ is the active reducing species – clearly its formation from DMAB depends on pH. Multistep electron transfer mechanism, in which each step involves the production of hydrogen (one-electron oxidation of the borane hydrogen atoms), have been proposed for an alkaline media [Schlesinger00,Sadik05]:

$$2 \, BH_{4-n}(OH)_n^- + 2 \, OH^- \rightarrow 2 \, BH_{3-n}(OH)_{1+n}^- + H_2 + 2 \, e^- \tag{4.4}$$
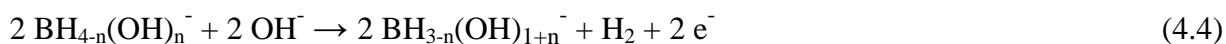
(with n=1,2,3 in the course of the oxidation). Note that the (formal) oxidation state of the boron (+3) does not change before and after the oxidation instead it is the hydride hydrogens that are oxidized to H_2 molecules (see also chapter 3). This mechanism predicts a strong correlation with high pH values; hence it cannot be expected to be valid at pH values lower than 7. The relevant redox potentials have been determined at several very basic pH values [Sadik05]. An extrapolation of the pH dependence to our pH 7.5 gives values above 0 V_{SHE}, which would not allow copper, let alone cobalt or nickel reduction, another indication that the multistep electron transfer mechanism (4.4) can be responsible only for the side reactions, especially hydrogen evolution. However, some predictions about the standard electrode potential of DMAB can be made. Since DMAB can reduce iron (E^o=-0.45 V) to its metallic state [Nakanishi05], standard electrode potential of DMAB must be smaller than (-0.45 V) therefore iron can be reduced (E^o_{DMAB}<-0.45 V). Then the more noble copper would be very easy to reduce. Besides DMAB, previously hypophosphite (standard redox potential, E^0=-1.57 V) has been used as a reducing agent in the deposition of nickel and cobalt within the central channel of the TMV particles [Knez04b]. If the E^0 value of a reductant is lower than that of an oxidizer, then the reaction between an oxidizer and a reductant will take place from the thermodynamic point of view. For example, if we had used hypophosphite instead of DMAB in the ELD of copper in the presence of $EDTA^{4-}$ (E^0= -0.216 V), the spontaneous deposition of copper would occur since the difference of the standard redox potentials of anodic and cathodic reactions is positive (+1.354 V) and therefore the change in the free energy is negative (spontaneous reaction). The addition of ligands to the ELD solution changes the redox potentials of metal because of the strong complex formation with the ligands. For example, upon addition of $EDTA^{4-}$, the redox potential of copper decreases from 0.345 V to –0.216 V. Therefore, spontaneous metal deposition is prevented. Another parameter affecting the thermodynamics of ELD reactions is the pH of the solution. The redox potential of the reducing agent becomes more negative when the pH of the ELD solution is increased.

A number of side reactions should be considered. First, gas bubbles were observed during the ELD processes (and actually used as an indicator for the start of the metallization). This is attributed to the evolution of H_2 molecules (see also chapter 3.3 for gas evolution during ELD in different deposition conditions). Nevertheless, hydrogen evolution during the ELD reaction causes voids in the deposited material, which affects the final structure of the material [Schlesinger00]. Surfactants or wetting agents are used to decrease the surface tension of the deposition solution and improve the elimination of hydrogen gas bubbles formed on the deposited material surface by the reducing agent dehydrogenation reaction. The selection of surfactants may vary depending on the deposition condition of the ELD bath employed. Alternatively, cyanide ions are very likely to adsorb strongly on metal surfaces and facilitate the desorption of the hydrogen gas bubbles from the deposit surface [Nakahara83]. It is crucial to note that all mechanisms can involve the codeposition of boron, during the deposition of metal structures, by yet another side reaction [Sverdlov05], with important consequences for mechanical and magnetic properties of the deposit.

While all these considerations are valid at the macroscopic scale, at the nanoscale, ELD can change a number of parameters. For example, the dissolution potential of nanoscale metals can shift some mV from the bulk value [Kolb97]. The concentrations in the vicinity of a growing copper surface deviate substantially from the bulk values. In the extreme case, one may have to be cautious to define the concentrations: A 4 nm long part of the 4 nm wide channel of TMV filled with the ELD bath contains only one copper ion and two DMAB molecules, and the electrochemical double layer on the face of a growing copper wire refers to an area of only $\pi x (2 \text{ nm})^2$ with 220 copper atoms.

4.4 Deposition of Nickel, Cobalt and Iron

Because of the bulk ferromagnetic properties of nickel, cobalt and iron, synthesis of those metals within the central channel of TMV is of high interest [Sun00,Andricacos98a]. The magnetism at low dimension is even more interesting, for example, highly ordered arrays of magnetic nanowires are expected to play an essential role as materials for high density arrays of magnetic storage and magnetoresistive devices due to their unique magnetic properties [Fert99]. As it is discussed in chapter 2, TMV is a very suitable template for the synthesis of a variety of nanomaterials on the outer surface as well as within the central channel due to the presence of different amino acids on both surfaces (see chapter 2 for details). As in the case of copper metallization, here the TMV was first activated with Pd (II) ions, followed by metallization with borane-containing metal ion solutions. In this way, synthesis of nickel and cobalt wires (3 nm wide) has been accomplished within the central channel of TMV particles [Knez04]. In this part of the work, the development of a new Ni ELD bath compatible with TMV particles for the synthesis of Ni and CoFe nanowires within the central cavity of the virus is explained. Note that most of the ELD baths are prepared with a trial and error method and therefore they are empirical. By manipulating the ingredients of the ELD bath by various metal ion sources, complexing agents, and buffering agents, it is expected to cause modification of the structure and magnetic or electrical properties of the synthesized nanowires within the channel of the virion. It has been observed that magnetic and structural properties of nanomaterials (4-6 nm FePt nanoparticles) are strongly correlated with each other [Sun00]. Some of the ELD solutions contain additional organic and inorganic ingredients (e.g. thiourea) in order to achieve the desired quality of the deposited films. For example, addition of guanidine hydrochloride to the electroless copper deposition solution enhances the ELD rate and hence the morphology of the deposited copper becomes rougher and porous [Hung86]. Using organic additives, Lallemand et al. have concluded that the morphology of the electrolessly deposited CoFe alloy strongly depends on the organic additives in the ELD bath [Lallemand04]. As

expected, electrolessly deposited Co films showed the usual hexagonal close packed (*hcp*) structure whereas CoFe alloy films showed face centered cubic (*fcc*) structures [Schlesinger00]. Addition of iron has changed the crystalline structure of cobalt. Single crystals of the same compounds show the same structures (Co (*hcp*) and CoFe (*fcc*)) [Shapiro77]. In the same way, magnetic properties of the Co changed upon addition of Fe.

A Ni ELD bath compatible with TMV particles was developed in the same way as the Cu ELD bath was developed for the deposition of copper within the virion (Chapter 4.3). For this reason, many of the arguments concerning the mechanism apply also here; the activation procedure is even identical. The ELD bath consists of nickel sulphate as a metal ion source, ammonium hydrogen citrate as a complexing agent, ammonium chloride, and DMAB as a reducing agent. All the ingredients of this Ni ELD bath have been used for ELD of various metals including Cu, Ni, Co, and Au [Mallory90]. The pH of the bath was adjusted to 7.5 with NaOH. The developed bath is stable at room temperature. Thus, there is no color change, gas evolution, and metal agglomerates formation in the ELD bath without contacting catalytically activated surfaces.

The nickel deposition was performed by first treating the virions with an aqueous solution of palladium (II) and afterwards mixing the catalytically activated virions with the nickel ELD bath. Figure 4.2 shows bright-field TEM images of nickel nanowires inside the virions, ~3 nm in diameter and approximately 100 nm in length.
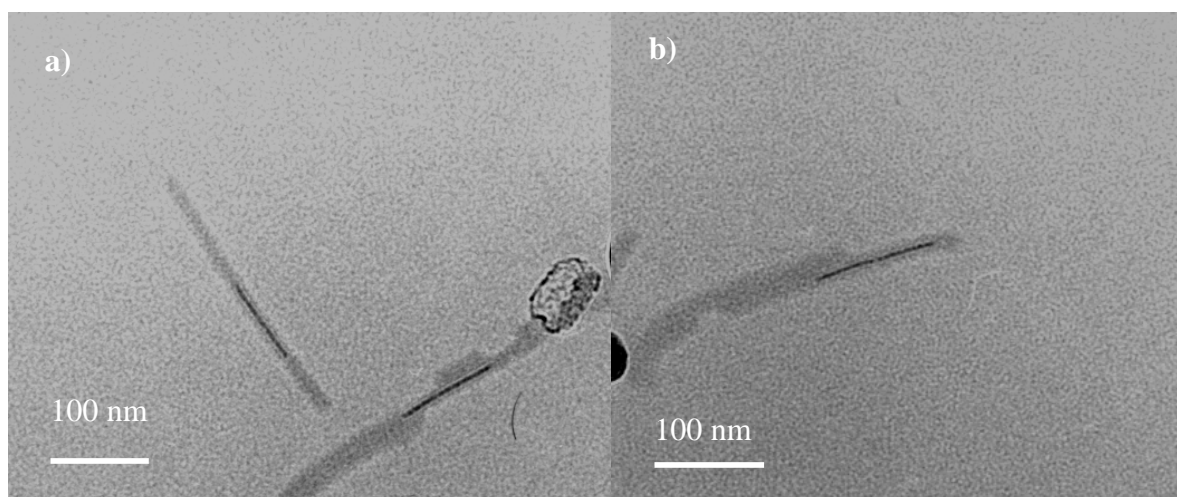
Figure 4.2: TEM micrographs of nickel nanowires within the central channel of TMV particles. **(a)** The dark lines correspond to two-nickel nanowires perpendicular to each other, 3 nm in diameter, approximately 100 nm in length. Dark-grey regions (the viral coat protein) surround the wires. The lower mineralized virion aggregated with another virion side by side. The large object attached to the end of the metallized virus might be a protein aggregate. **(b)** A 100 nm nickel nanowire (dark line 3 nm in diameter) within the central channel of a virion (grey region around the nanowire). Next to the metallized virus, another virus is attached from its side.

Selectivity of the metallization. An obvious question is why the wires are deposited with such high selectivity. As previously discussed, without dialyzing the TMV suspension against water, nanowires inside virions cannot be observed, but the outer surface is coated with nickel [Knez04]. During dialysis of TMV suspension against water, sodium-potassium phosphate buffer (from the isolation procedure of the TMV) in TMV suspension moves through the dialysis membrane and concentration of the phosphate buffer decreases substantially. The decrease in phosphate concentration depends on the amount of water in the dialysis unit, the amount of dialysis time, and the number of dialysis steps. Nonetheless, all the phosphate molecules present in the virus suspension cannot be completely removed. The concentration of phosphate in the TMV suspension decreases exponentially until the equilibrium is reached. 10 minutes waiting is enough for selective deposition of the nickel within the channel of the virus. Note that ten dialyses against fresh water

(each 1 min) might be better than one dialysis against fresh water (10 min) in order to further decrease the concentration of phosphate in the TMV suspension. Nevertheless, one dialysis of the TMV suspension was performed for the synthesis of nanowires within the virus. Phosphate mainly exits in aqueous solution at pH around 7 in the form of HPO_4^{-2}, and $H_2PO_4^{-1}$ (pKa_2 phosphoric acid=6.9) [Fritz74]. These ions can interact with the positively charged amino acids. Upon addition of Pd(II) solution to the phosphate containing TMV suspension, phosphate molecules on the coat protein surface may interact with the palladium ions. Indeed, recently Mori and coworkers have attached $PdCl_4^{-2}$ to hydroxyapatite surface via chemical bond formation between the palladium ions and phosphate molecules bound to the surface [Mori02]. These complexes were proposed after analyzing the hydroxyapatite surfaces by several spectroscopic techniques [Mori02,Mori04]. The system has been used in several organic reactions and surprisingly catalyst particles have survived after harsh chemical reactions [Mori04]. Scheme 4.2 illustrates two different kinds of coordination of Pd(II) with PO_4^{-3} molecules fixed to a surface; HPO_4^{-2}, and $H_2PO_4^{-1}$ would qualify, too. Since it is well known that at the beginning of the ELD reaction, materials can only be deposited on catalysts surfaces, thus nickel can be deposited on the outer surface of TMV particles and it can be fixed there by palladium-phosphate complexes [Schlesinger00].
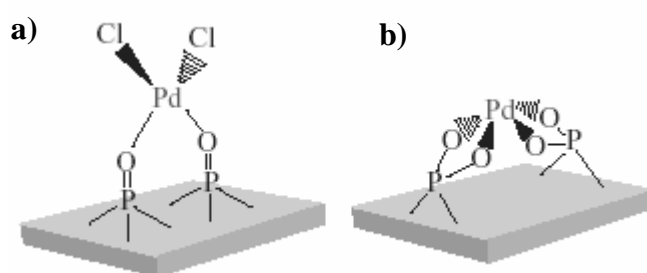
Scheme 4.2: Coordination of Pd(II) with PO_4^{-3} fixed to a TMV coat protein surface. **(a)** $PdCl_2$ coordinated by chemisorption on the phosphate **(b)** a monomeric Pd(II) phosphate complex surrounded by four oxygens.

In the absence of phosphate molecules (after dialysis of TMV suspension), grown metal clusters on the outer surface of virions can easily detach. However, in the presence of the phosphate molecules,

the metal clusters grow on the exterior surface of the coat protein. Scheme 4.3 compares the effect of phosphate buffer on the metallization of TMV. Note that RNA molecules (in the backbone) of TMV also contain phosphate groups, but they are close to the inner surface of the TMV particles and not accessible from the outer surface (see chapter 2 for details). As a result they do not contribute to the metallization of the outer surface. However, at the ends of the virions metal ions can indeed interact with some parts of the RNA backbone that cannot be buried inside the coat proteins.

a) Without phosphate buffer   Detaching from the surface

a) With phosphate buffer   Staying on the surface
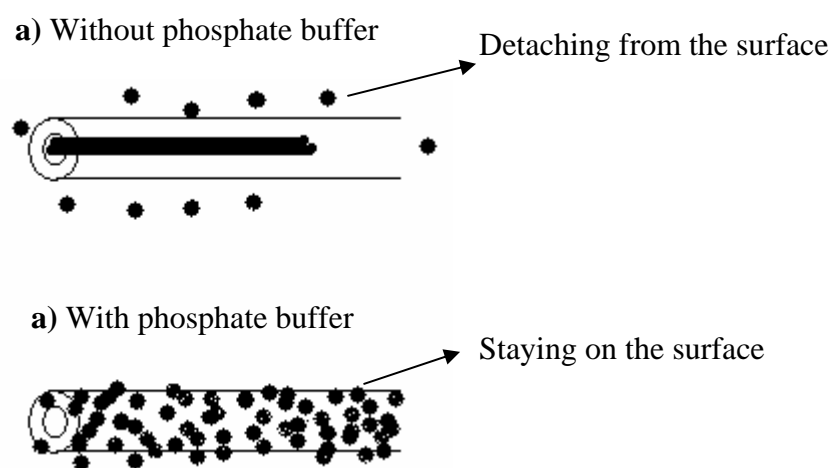
Scheme 4.3: Comparison of "inside" and "outside" metallization of TMV. **(a)** "Inside metallization" of TMV in the absence of phosphate buffer **(b)** Early stage of "outside metallization" of TMV in the presence of phosphate buffer.

Deposition kinetics. Since the nanowires are merely about 10 atoms wide, one would not expect that the growth kinetics (see also Scheme 4.3a) are comparable to measurements at macroscopic systems. However, the opposite is true; it turns out that from the macroscopic rate measurements some predictions can be generated. To this end, we first have to estimate the influence of the diffusion of the reacting species inside the viral channel. We can safely assume that metal ions diffuse through the central channel of the virion instead of diffusing between the protein subunits of

the coat protein. This is obviously the conclusion from the work of Dujardin and co-workers in which they deposited silver nanoparticles inside the channel of TMV and afterwards treated the metallized virions with uranyl acetate [Dujardin03]. Between the silver nanoparticles they did not observe any uranyl acetate contrast (staining) in TEM observations. Thus uranyl acetate is diffusing through the central channel of the virus rather than diffusing through the coat protein. In a first approach, one-dimensional diffusion can be assumed during the deposition of materials in the channel. The following formula: $(<x^2>)^{1/2} = (2Dt)^{1/2}$ describes the average diffusion path of a molecule related to the diffusion coefficient of a molecule and time needed to travel a long the path [Adamson73]. Small molecules have diffusion coefficients of about $\sim 10^{-5}$ $cm^2 sec^{-1}$ at room temperature in water [Adamson73]. If we take the diffusion path as 300 nm (length of a single virion), the time required for traveling the path is in the microseconds range (~ 25 µs). This is a very rough estimation of the diffusion of complexes through the inner channel of TMV, however it gives the time scale (microseconds range). Obviously, even when we allow for a more complex mechanism, this is much faster than the growth of the wire, so we expect that all reactants are present more or less at bulk concentration inside the channel.

Macroscopically, the rate of nickel (density 8.9 g/cm^3) deposition on a copper plate at room temperature was measured to be as high as 0.155 mg/min (amount of deposited material/time), corresponding to 0.109 nm/sec (thickness of deposited material/time). A large copper plate was used in the rate measurements (see also experimental part). If we assume nanoscale deposition of nickel in the channel as depicted in Scheme 4.4a, the time needed to fill the whole channel would be (300 nm /0.109 nm/sec) 45.8 min (t_1). This is slightly longer than the time required for metallization of TMV suspension (20-30 min), but surprisingly not off by some orders of magnitude. If we assume two nucleation sites in the channel as shown in Scheme 4.4b, then 22.9 min (t_2) can be obtained to metallize the whole channel of a virion, which corresponds to the measured metallization time (20-30 min). In the case of many nucleation sites (Scheme 4.4c) inside

the channel, the time required for filling the whole channel with metal is much smaller (for 3 nm, deposition time=~28 sec).
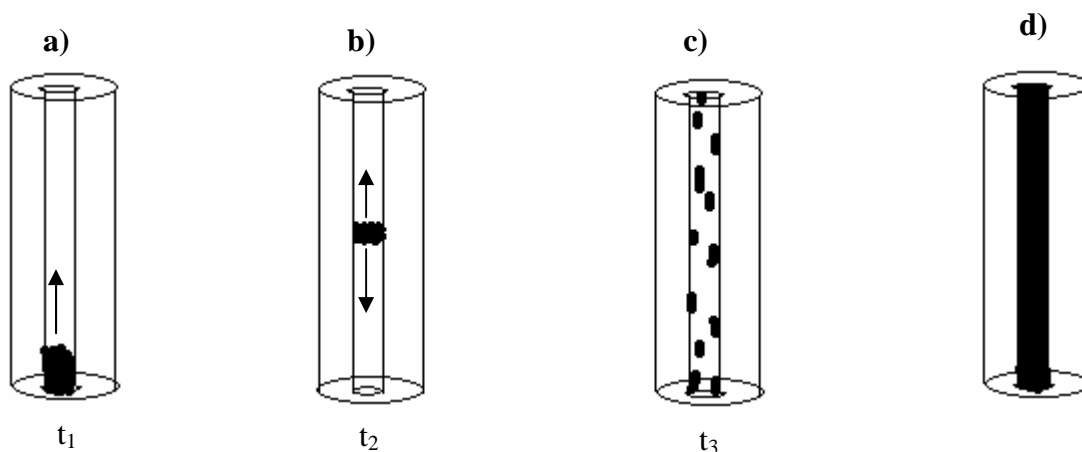
Scheme 4.4: Schematic overview of metallization of a single TMV particle. **(a)** Single nucleation process in which metallization continues in one direction **(b)** Double nucleation process in which metallization continues in two different directions **(c)** Multiple nucleation processes **(d)** A completely metallized virion ($t_3<t_2<t_1$).

In TEM, we do not observe many nanowires in a single virus instead we observe one or two nanowires in the channel of the virus. Based on the experimental observations, it can be concluded that instead of many nucleation sites, single or double nucleation sites are present in the metal deposition in the channel. Despite these results, one has to be careful to assign the same ELD mechanism as for bulk samples because in the latter case usually large areas with more than 10^{15} atoms are investigated. On an area with only around 200 atoms, of which up to 100 are so close to the channel surface that they are sterically not easily accessible, the electronic structure of the surface and also the electrochemical double layer might change substantially. Moreover, the unresolved question of where on the growing surface the catalytic reactions occur is even more complex due to the close distance of metal ion and reductant.

Preparation of uncoated 3 nm wires. Coming back to the wire itself, the measurement of some of its physical properties (i.e. transport / conductivity) requires elimination of the coat protein of the virus. In order to remove the coat protein of the metallized virions, an enzyme called Proteinase K was used. The smallest peptide that can be hydrolyzed by this enzyme is a tetrapeptide, and therefore the comparatively large protein subunits of TMV (17.5 kD) can be easily hydrolyzed into smaller units. For such an experiment, TMV particles were activated with Pd(II) and metallized with an ELD bath containing nickel acetate, lactic acid, and DMAB (see also experimental part). Subsequently, the metallized virions were adsorbed on a TEM grid and incubated in Proteinase K solution. A bright-field TEM imaging revealed nickel nanowires without coat protein (Figure 4.3).
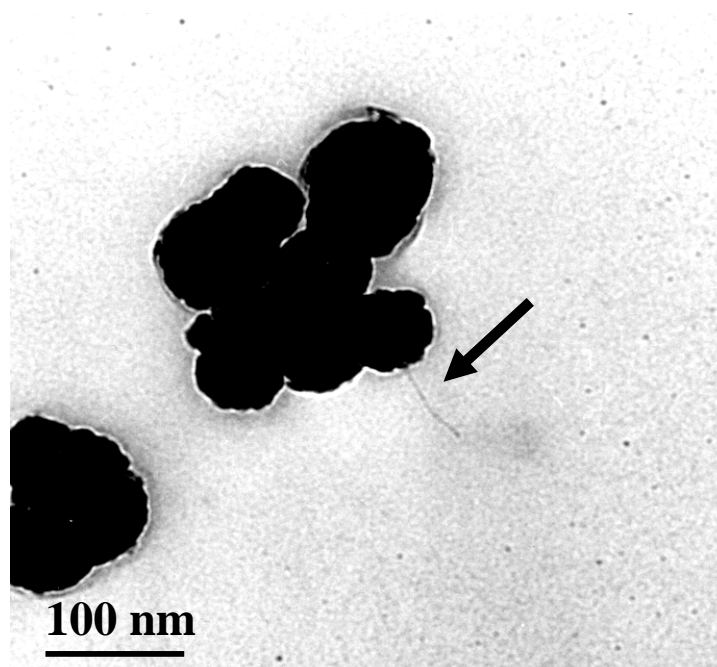
Figure 4.3: TEM micrographs of a nickel nanowire after Proteinase K treatment on a carbon-coated TEM grid. The dark line indicated with a black arrow indicates a ~50 nm long nickel nanowire. One end of the nanowire is attached to the large metal agglomerate (a few hundred nanometers in diameter).

This process will be very useful for measuring the transport properties of individual nanowires without coat protein on its surface. Moreover, Figure 4.3 shows the final proof the ELD produces continuous wires rather than agglomerates of nanoparticles; the bare wires even withstand contact

with solutions (such as the enzyme solution). As discussed above, a thin oxide layer can be expected upon contact with air or aqueous solutions.

Alloy wires and corrosion. Various alloys of nickel, cobalt and iron have been synthesized and evaluated for properties including corrosion resistance, microstructure, electrical resistivity, and magnetoresistance [Andricacos98a]. The deposition of alloys of CoFe works in the same way as the deposition of copper, nickel or cobalt except one difference: Instead of a single metal ion source several metal ion sources were used. As in the case of other metallizations (nickel, cobalt and copper) (see also experimental part) the TMV suspension is dialyzed against water prior to usage [Knez04]. In order to prepare the CoFe ELD bath, to the original cobalt ELD bath, which contains sodium succinate, cobalt sulphate and DMAB, iron sulphate is added. The bath remains stable at room temperature. In other words, the prepared ELD bath does not decompose. Subsequently, the CoFe ELD bath is contacted with the Pd (II) activated virions. Figure 4.4 illustrates bright-field TEM images of the nanowires, ~3 nm in diameter and approximately 100 nm in length.
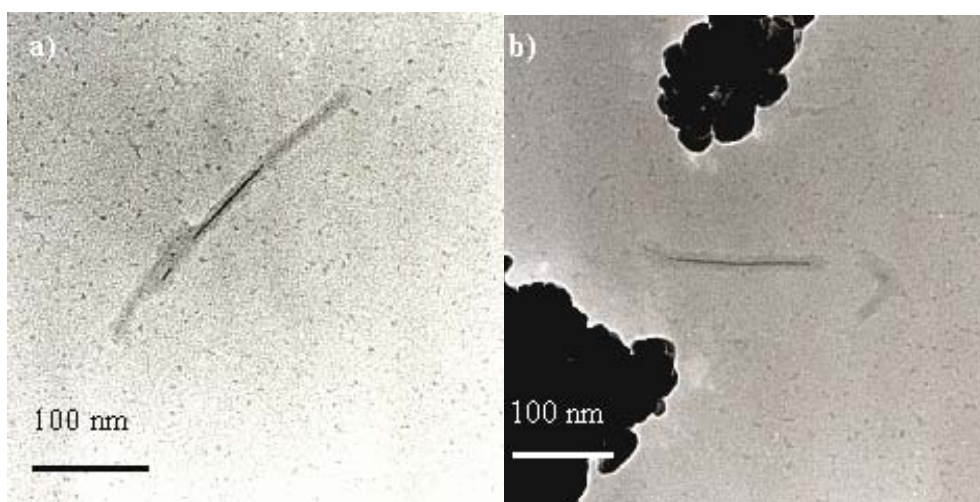

Figure 4.4: TEM micrographs of CoFe alloy nanowires within the central channel of TMV particles. **(a)** The dark lines correspond to CoFe alloy nanowires, 3 nm in diameter, approximately 100 nm in lengths. Below the lower part of the metallized virion a small nanowire (~10 nm) is present. Another shortened virus particle (~100 nm) is attached to the lower part of the metallized virion. Dark-grey region (the viral coat protein) around the nanowire is a single TMV particle. **(b)**

Approximately, 150 nm dark-grey region around the nanowire corresponds to the half of a TMV particle. The large dark regions correspond to the big nodules deposited on the surface.

Recently, Nakanishi and co-workers have reported DMAB assisted electroless deposition of iron on amine-terminated surfaces [Nakanishi05]. They have demonstrated that DMAB can reduce Fe(III) to Fe^0. Therefore, reduction of iron(II) and cobalt(II) ions to the metallic state is thermodynamically allowed. The reduction of more noble cobalt is at least thermodynamically even more favorable. The nanowires obtained from the CoFe-ELD bath were not stable for more than two weeks in air. On the TEM grid surface, nodules a few nanometers in diameter were observed at every part of the sample. In this condition, it is not easy to find virions in TEM observations. Probably, the deposited metal on the TEM grid reacted with the oxygen in air and formed metal oxides on the surface. Oxygen can penetrate through the coat protein of the virus [Calhoun83] and interact with the nanowire within the channel.

It has been shown that the corrosion (an electrochemical process in which a metal reacts with its environment to form an oxide or other compounds) resistance of the deposited films depends on deposited material composition (elemental composition) and on the microstructure, which are controlled by deposition solution composition and deposition variables [Andricacos98a,Myung01]. Moreover, it has been observed that electrolessly deposited nickel generally provides a nickel coating that has a lower porosity and more uniform thickness than the electroplated nickel [Schlesinger00]. Because of this property, electrolessly deposited nickel films are an effective corrosion protecting agent. Myung and co-workers added Ni to the Co, Fe or CoFe alloy films in order to improve the corrosion resistance [Myung01]. They have found that the corrosion resistance of electrolessly deposited CoFe films is an order of magnitude lower than CoNi and NiFe films [Myung01]. Substantially increased corrosion resistance has been obtained by adding Ni to CoFe alloys [Yokoshima00]. In a similar way, Ni was added to CoFe alloy by simply adding nickel acetate to the ELD bath containing sodium succinate, cobalt sulphate, iron sulphate and DMAB (see

experimental part for details). The produced bath was stable and could be used for depositing CoFeNi on activated surfaces; for instance, a palladium activated glass surface could be easily coated with a shiny coating of CoFeNi alloy. After contacting with the catalytically activated virions, nanowires within the central channel of TMV particles were obtained. These nanowires were used for further studies like chemical analysis (see chapter 4.6). Surprisingly, the improved corrosion resistance by codeposition of Ni, which is known for bulk samples, can be also observed on the nanoscale.

4.4.1 Crystal Structure of Ni Nanowires

The crystal structures of materials are directly related to the magnetic, electrical, and optical properties of the materials [Kittel53]. High-resolution transmission electron microscopy (HRTEM) allows the imaging of the crystal structure of the materials on the atomic scale [Williams96]. Therefore, HRTEM is used to reveal the crystal structure of the nickel nanowire. This part of the work describes the crystalline structure of the nickel nanowires (see chapter 4.2 for the nanowire synthesis). Figure 4.5 shows a high resolution TEM image of a nickel nanowire within the central cavity of a TMV particle. In this image, the lattice planes of the nanowire are clearly discernible. The regular spacing of the observed lattice planes is 2.10 Å. The lattice planes of the nickel nanowire are perpendicular to the virus long axis. The substrate is an amorphous carbon-coated Cu-TEM grid.
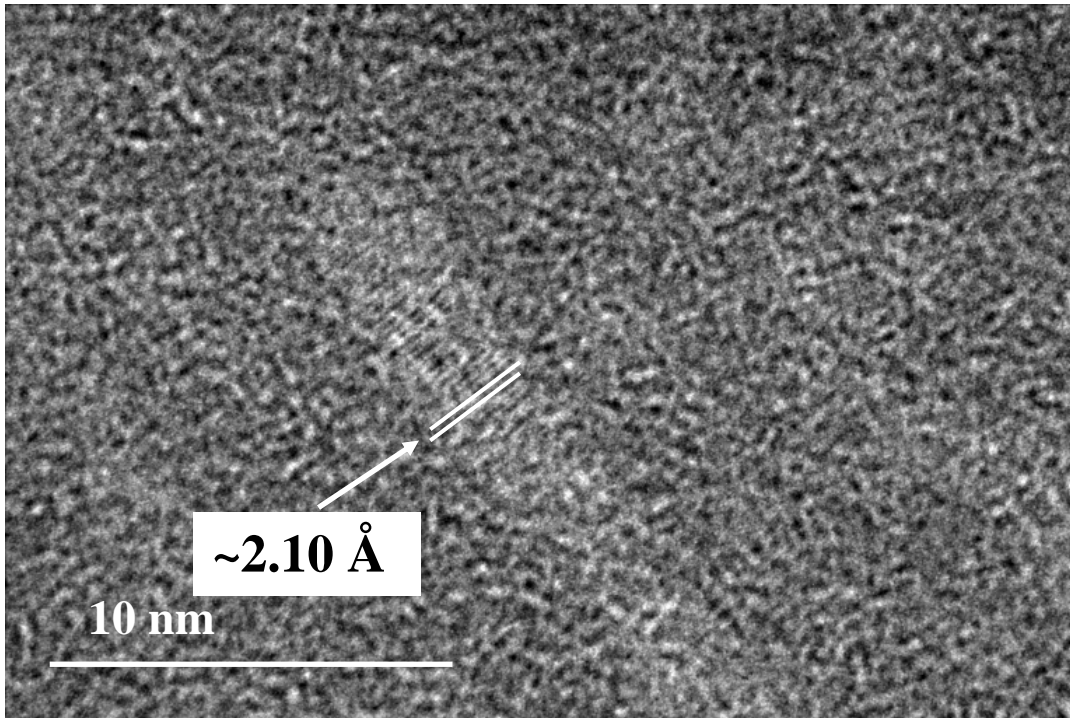
Figure 4.5: High resolution TEM image of a nickel nanowire. The nanowire is inside the virion central channel. The white arrow indicates the inter plane distance. Note that the nanowire is surrounded with the amorphous virus coat protein.

hkl_{cubic} (NiO)	$hkl_{\text{rhombohedral}}$ (NiO)	$d_{\text{calculated}}$ (Å) (NiO)	hkl_{cubic}(Ni)	$d_{\text{calculated}}$ (Å) (Ni)
111	100	2.4123	100	3.52
	111	2.4089		
200	110	2.0883	110	2.49
220	$\bar{1}$10	1.4775	111	2.03
	121	1.4759		
311	11$\bar{1}$	1.2599	200	1.76
	210	1.2594		
	221	1.2584		
222	200	1.2061	210	1.57
	222	1.2044		
400	220	1.0442	211	1.44
331	20$\bar{1}$	0.9587	220	1.25
	311	0.9580	221	1.17
	322	0.9574		

Table 4.2: Calculation of some of the diffraction peaks of NiO and Ni.

Table 4.2 shows the x-ray diffraction pattern of the rhombohedral NiO structure (a rhombohedral unit cell with a (lattice constant)=2.95Å, and α (angle)=60.07[0]) and cubic Ni structure (*fcc* structure, and a=3.52Å). At room temperature, NiO has a cubic lattice, which is slightly distorted to give a rhombohedral unit cell [Toussaint68]. Since the nickel nanowires were grown at room temperature, only the rhombohedral structure is discussed here. Calculations of the distances between the adjacent planes for NiO were taken from the work of Toussaint and co-workers [Toussaint68]. For Ni, distances between the adjacent planes are calculated with the formula $d(hkl)=a/(h^2+k^2+l^2)^{1/2}$ [Kittel53]. In this formula, $d(hkl)$ represents the spacing between the two adjacent planes of a set (hkl) [Kittel53]. The term (hkl) denotes a single plane or a set of parallel planes and h, k, and l are called *Miller indices*.

Based on the calculations in Table 4.2, the 2.10 Å of lattice planes corresponds to the separation of either (111) planes of *fcc* nickel metal (2.03 Å) or (110) rhombohedral nickel oxide (2.0883 Å). Note that coat protein of the virus surrounds the nickel nanowire shown in the figure. Therefore, the planes of the crystal are a little blurred by the amorphous coat protein, which makes interpretation difficult. In the future, HRTEM observations after removing the coat protein surrounding the nanowire, which is possible (see chapter 4.4), could enhance the image quality. Recently, Rellinghaus and coworkers have studied the oxidation of nickel nanoparticles in ambient conditions [Rellinghaus01]. Nickel nanoparticles were prepared by means of DC sputtering in argon atmosphere. It has been found that the nickel nanoparticles consist of a metallic core surrounded by an oxide shell [Rellinghaus01]. This conclusion has been supported using electron energy loss spectroscopic investigations. In a similar way, oxidation of copper nanoparticles in ambient air has also been studied in TEM [Kim04]. A thin coating (a few Å in thickness) on the copper spheres has been observed in TEM, the day after the production (0.3 Å/day) [Kim04]. This kind of thin layer oxide formation is called natural passivation (the process by which metallic species develop thin layers of oxidative products), which acts to protect the metals from further (corrosive) attack [Barr78]. Therefore, it is predicted that the nickel nanowire inside the virus consists of a metallic Ni

core surrounded by a passivating thin NiO shell. Note that addition of nickel to CoFe alloy nanowires resulted in an increase of the corrosion resistance of CoFe nanowire. In any case, spectroscopic characterizations of the nanowires are required in order to be sure that oxygen is present in the nanowire. For example, as it has been described in chapter 4.6, energy-filtering TEM can be used for this purpose. Previously, X-ray diffraction of the nickel films, produced with electroless deposition, showed a diffraction peak at (111) planes [Lewis96]. Moreover, nickel nanowires, 4 nm in diameter and grown within the carbon nanotubes, showed crystalline structure with preferable orientation of (111) planes of *fcc* nickel metal [Pradhan99]. The desired orientation in (111) plane direction could be associated with the lower strain in (111) orientations rather than in other orientations, e.g. (100).

4.5 Selective Deposition of Gold

Ordering inorganic nanoparticles by using soft materials as templates is essential to construct electronic devices with new functionality (for example, in the form of chemical or biological recognition and sensing capabilities). Nanostructured protein shelled viruses are attractive for ordering quantum dots for self-assembled building blocks toward next generation functional electronic devices [Lee05]. For example, such functionality has been realized in DNA assisted assembly bridging the electrical circuits [Chung05]. Hence these biomaterial systems are not only useful as biological sensors but also as self-assembled nanoelectronic circuits. In this part of the work, we describe the selective adsorption of 6 nm gold nanoparticles (Au-nps) to the ends of TMV particles and the size-enhancement of the Au-nps using electroless deposition (ELD) method. Different from the previous studies, the ends of the TMV are selectively mineralized using ELD of gold.

Selective binding of 6 nm Au-nps to the ends of TMV particles was achieved as described in the experimental part. Figure 4.6 illustrates the TEM micrographs of selectively attached Au-nps to the ends of the TMV particles (in Figure 4.6a a single TMV particle and in Figure 4.6b two TMV particles). In some cases, a single Au-np can be adsorbed to the ends of the TMV. However, more than one Au-np can also be found (Figure 4.6a), but no Au-np (~0%) was found attached to the coat protein of the virus.
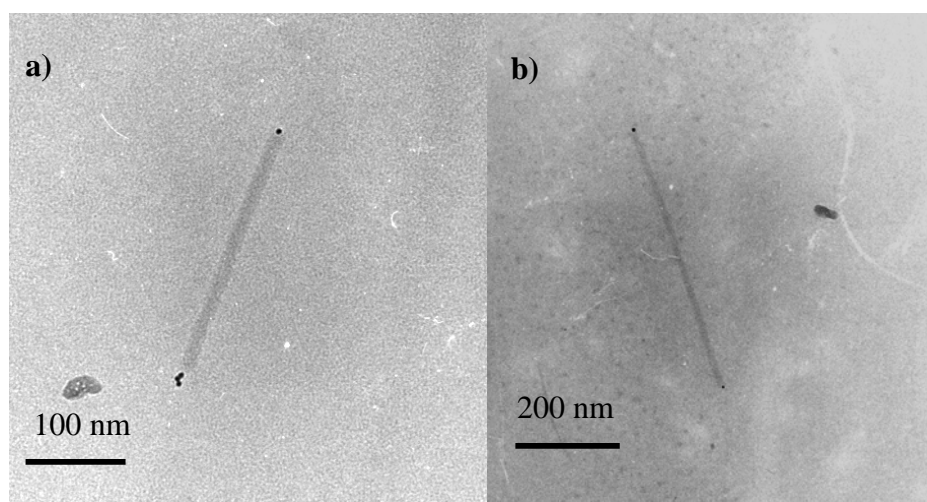

Figure 4.6: TEM micrographs of 6 nm Au-nps assembled at the ends of TMV particles. **(a)** A 6 nm Au-np is attached to one end of a single TMV particle (~279 nm in length), and three Au-nps are attached to the other end of the virion. **(b)** A single Au-np is attached to the ends of two end-to-end assembled TMV particles (~562 nm in length).

For an interpretation of these surprising results, RNA strands that protrude several nm from the TMV ends have to be invoked (this requires that several coat protein units are removed, which nicely explains the dimuished average length of the virions of ~280 nm). Whether RNA is "sticking out" from TMV or not is not well researched [Culver02]; commonly one assuemes that this is not the case. However, previously, coat protein of the TMV particles was stripped with alkali, urea, and dimethylsulfoxide solutions, and the protruding RNA was imaged with AFM [Drygin98]. Images of partially uncoated TMV particles with protruding RNA molecules from one or both ends and individual RNA molecules were demonstrated [Drygin98]. Another way of stripping the coat

protein of the virus is by using enzymes. An enzyme, Proteinase K (see also above) was used for stripping the coat protein completely of the virus. The TMV-RNAs were subsequently mixed with Au sol and incubated overnight. Figure 4.7 illustrates the TEM micrograph of aggregated Au-nps interacting with the stripped TMV-RNAs on a carbon coated Cu-TEM grid. Note that Au-nps sometimes form aggregated structures like a chain, which indicate a strong interaction of RNAs with the Au-nps. Au-nps adsorbed on the same substrate surface in absence of RNA did not indicate any such structures.
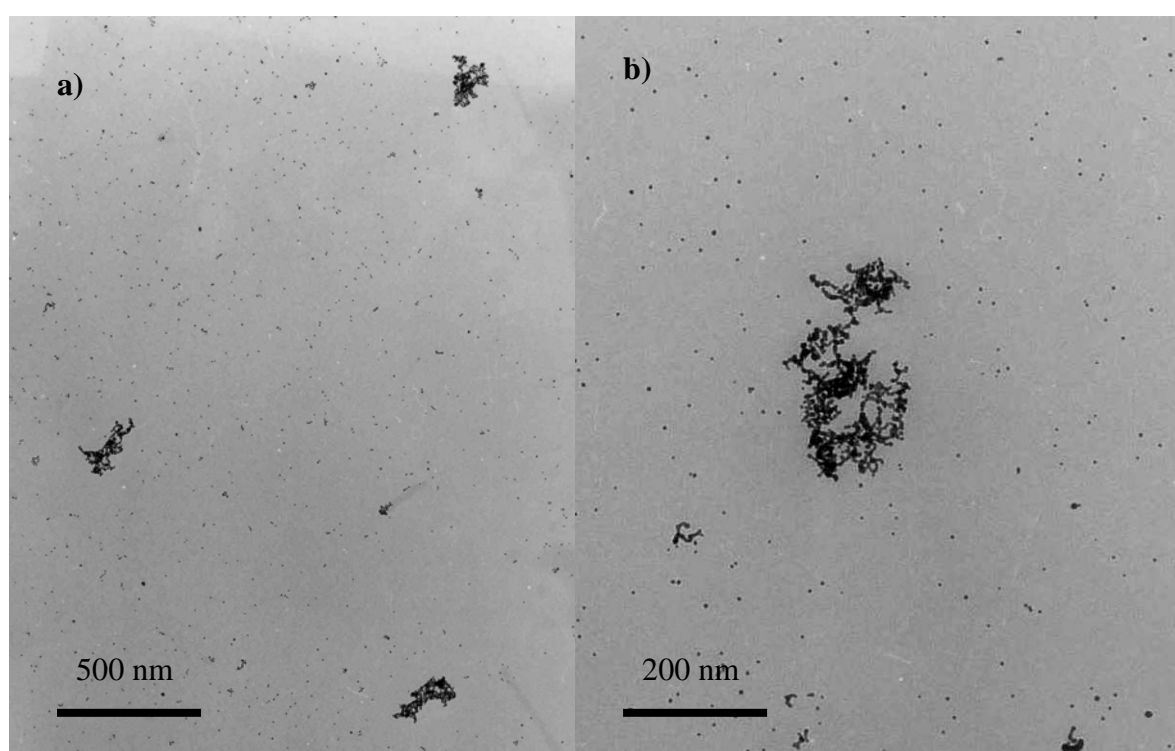
Figure 4.7: TEM micrographs of self assembled Au-nps along the RNA chains. These aggregated structures (Au-nps/RNA) were observed after pre-treatment of a TMV suspension with Proteinase K, followed by mixing with 6 nm gold sol.

In order to further understand the mechanism of the process, experiments were also carried out with TMV particles after removing the RNA protruding from their ends using an enzyme, Ribonuclease (abbreviated commonly as RNAse). This enzyme catalyzes the breakdown of RNA into smaller components. In parallel experiments, one TMV suspension was treated with RNAse and then

incubated with 6 nm gold sol. Another TMV sample without treating with RNAse was incubated again with 6 nm gold sol. All experimental parameters were adjusted to be the same for both of the samples. Approximately 20% of the RNAse treated TMV particles were labeled by the 6 nm Au-nps, however without RNAse treatment ~90% of the virions were selectively labeled at their ends with Au-nps. Additionally, it is clear that the presence of RNA at the ends of virions plays an important role in selective binding of the Au-nps to the ends of the TMV particles.
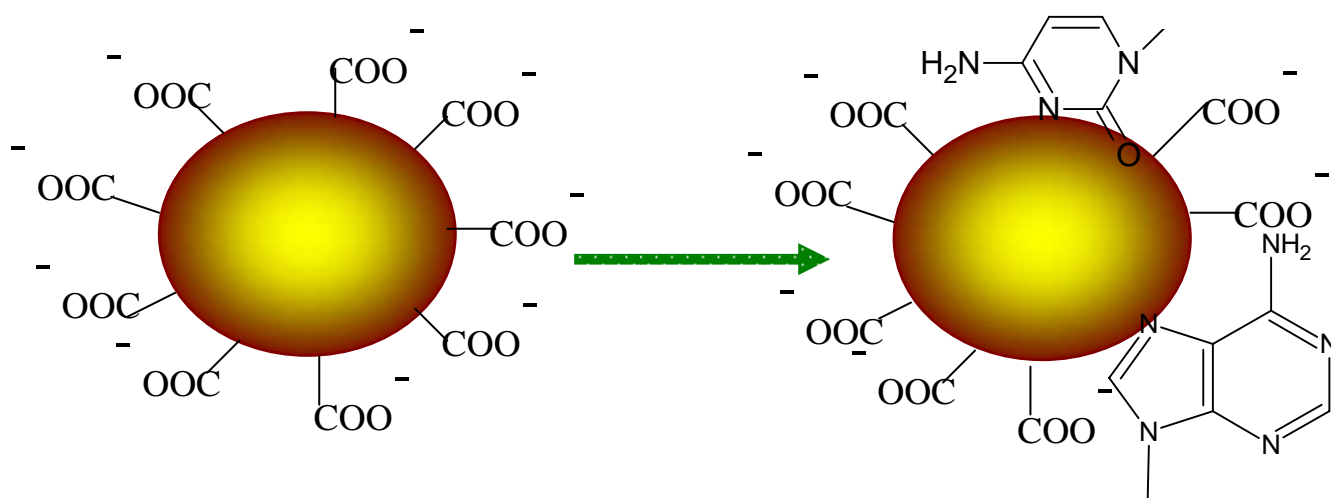
Scheme 4.5: Schematic view of selective attachment of 6 nm Au-nps to RNA (drawing not to scale). The lines connected to COO⁻ refer to citrate. The heterocylic aromatic bases in the backbone of the RNA replace the citrate on the gold surface. The RNA can be free RNA, or RNA protruding from the TMV ends.

Commercial (AURION) 6 nm Au-nps used in our experiments are terminated with citrate, yielding negatively charged particles with a zeta potential of about –42 mV. This result also correlates with the experimental measurements (by Biggs and coworkers), in which the citrate terminated Au-nps were shown to have –40 mV of a zeta potential [Juste01,Biggs94]. Furthermore, it has been highly accepted that the carboxylic groups of the citrate coordinate with the surface gold atoms (Au(I)) [Sandroff85]. The pH of the TMV-gold sol was around 5 so that we expect TMV particles to be

negatively charged since the TMV has an isoelectric point at a pH value of about 3.5 [Deggelmann94]. In other words, the TMV particles and the Au-nps are both negatively charged at the working conditions. Therefore, electrostatic interactions between the Au-nps and RNA of the TMV can be excluded from the mechanism of the process.

Previously, interaction of gold nanoparticles with DNA molecules was studied in detail, which gives some indications about the interaction mechanism of the RNA of TMV and 6 nm Au-nps. Sandström et al. have suggested a mechanism for the nonspecific or noncovalent binding of DNA (negatively charged due to the phosphate groups in the backbone) to the gold nanoparticles (negatively charged due to the presence of citrate groups on the surface of the gold nanoparticles) to be ion-induced dipole dispersive interactions, in which the negatively charged phosphate groups on the DNA molecules induce dipoles in the highly polarizable gold nanoparticles (13 nm) [Sandström03]. In this case high ionic strength of the solution is required to overcome the repulsive forces between the negatively charged DNA molecules and negatively charged 13 nm Au-nps. However, this mechanism cannot be applied to the TMV-Au-np system since the negatively charged coat protein does not interact with the Au-nps. Recently, it has been found that the driving force for DNA adsorption on the negatively charged gold nanoparticles is not of electrostatic origin, but rather due to the hydrophobic effect of the nitrogenous bases on DNA [Cardenes05,Cardenes06]. Similar mechanism can also be applied in the case of 6 nm Au-nps and RNA of the TMV, Scheme 4.5. The aromatic bases of the RNA replace the surface bound citric acid molecules and hence Au-nps selectively bind to the RNA. Since the major part of the coat protein is hydrophilic, Au-nps do not interact with the coat protein surface. Indeed, the work done by Larson and coworkers supports this process. It has been found that pyridine, a heterocylic aromatic compound, can replace the surface bound citrate molecules on gold surfaces [Larson97]. Using an AFM, it has been shown that the electrostatic potential of the gold surface decreases upon

addition of pyridine since negatively charged citrate molecules are replaced by uncharged pyridine molecules [Larson97].

In order to expand the scope of the functionality of the 6 nm Au-nps at the ends of TMV particles (for example for contacting nanowires within the central channel of TMV), electroless deposition of gold was used to enlarge the Au-nps at the ends of TMV. In this experiment, TMV-Au-nps were firstly adsorbed on a silicon wafer and subsequently, a solution containing $HAuCl_4$ (metal ion source in the reduction solution), ascorbic acid (a weak reductant), and CTAB (a cationic surfactant) was used to metallize the seed particles on the surface [Jana01]. Ascorbic acid is too weak to reduce gold in the presence of CTAB and in the absence of seeds (Au-nps), which was also shown by Jana et al [Jana01]. However, the gold salt reduction occurs very fast in the presence of gold seed nanoparticles.
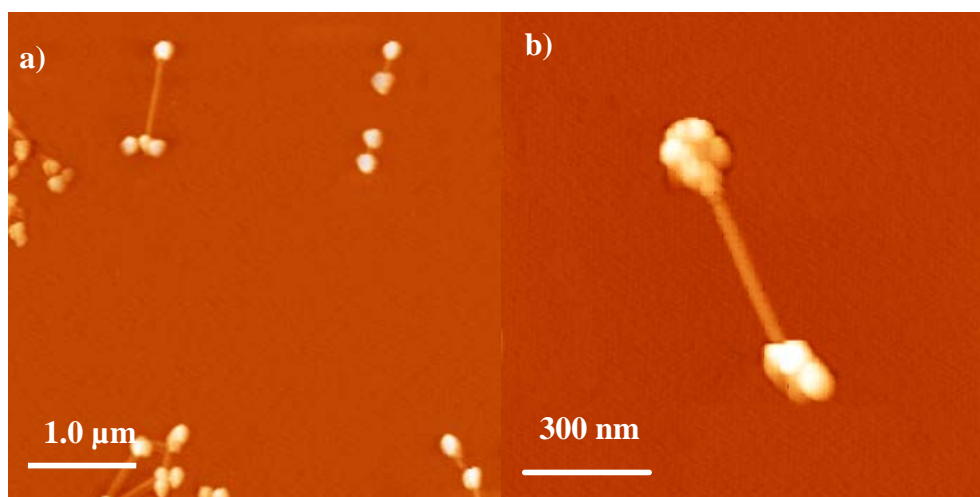

Figure 4.8: AFM image (non-contact, topography) of selectively size-enhanced gold structures (attached to the ends of the virions) on an oxidized silicon surface. **(a)** Size-enhanced gold structures at the ends of the TMV particles are sometimes building network structures. **(b)** Gold ''balls'' 60-80 nm in height after enlarging 6 nm gold nanoparticles. Two aggregated TMV particles (~600 nm in length) connect the gold ''balls''.

Dumbbell-shaped structures were formed after exposing the adsorbed TMV-Au-nps to the aforementioned ELD bath, (Figure 4.8). The height of the size-enhanced gold structures after gold

ELD is around ~60-80 nm. Nevertheless, these size-enhanced gold structures were not observed in the absence of Au-nps. Such dumbbell shaped structures, two metallic structures (''balls'') with one rigid protein rod in between, might be very valuable (as nodes) for investigating the electrical properties of the nanowires within the central cavity as well as on the outer surface of the TMV particles.
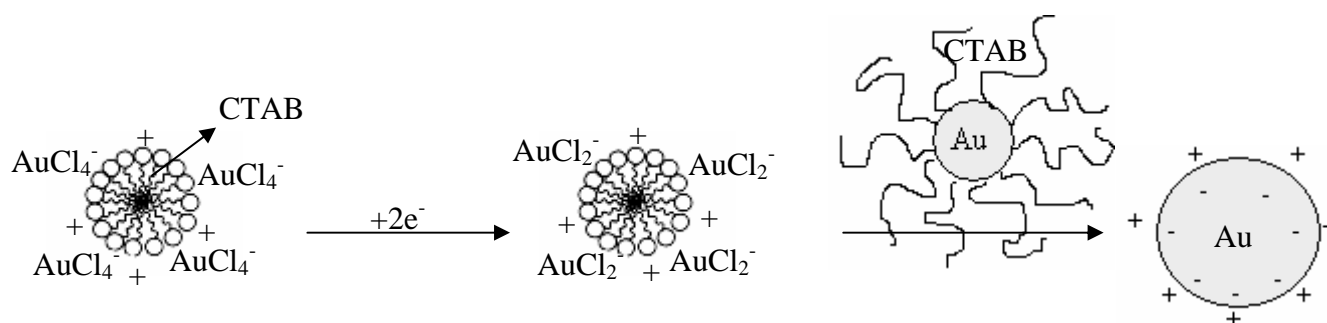
Scheme 4.6: Mechanism of electroless deposition of gold on the surface of 6 nm gold nanoparticles from the solution of $HAuCl_4$, CTAB, and ascorbic acid [adapted from Juste 04].

The mechanism of the enlargement of the gold seed nanoparticles has been heavily discussed in the literature by several research groups [Juste04,Jana01,Fernandez05]. According to the mechanism described by Juste and coworkers (see also Scheme 4.6), $AuCl_4^-$ ions are bound to cationic CTAB micelles by displacing the Br^- ions bound to the CTAB [Juste04]. Note that the zeta potential of Au-nps used in this experiment was measured to be as about –42 mV. CTAB molecules cover the gold seeds since CTAB is a cationic surfactant. This has been shown with the zeta potential measurements, in which the zeta potential of CTAB-coated gold surface has been found to be around +90 mV [Juste04]. Therefore, negatively charged $AuCl_4^-$ can easily coordinate with the positively charged CTAB molecules. It has been found that in the presence of CTAB, ascorbic acid reduces $AuCl_4^-$ to $AuCl_2^-$ [Juste04]. Moreover, the solution of $AuCl_2^-$-CTAB remains stable indefinitely. Nevertheless, without CTAB molecules present in the medium, $AuCl_4^-$ ions cannot easily coordinate with the Au-nps surface, which is negatively charged (–42 mV), at least in a very low ionic strength solution. CTAB acts both as a surfactant and a retarder in the gold deposition to

the 6 nm Au-nps and therefore uniform gold deposition can be accomplished in the presence of CTAB. Reduction of $AuCl_4^-$ ions to $AuCl_2^-$ ions by ascorbate takes place on the micelle surface. $AuCl_2^-$ ions remain adsorbed to the micelle surface. The transport of the bound gold ions to the growing seed particles is controlled by the double layer interaction of the cationic micelles with the micelle coated Au-nps attached to the ends of the TMV. Therefore, ascorbate anions transfer electrons to the Au-nps, which then reduce the gold ions to form a gold shell, which grows to a spherical shaped geometry (forming a dumbbell shaped structure).

4.6 Chemical Analysis of Nanostructures

A large range of analysis tools can be used in order to determine the chemical composition of nanomaterials. Here we concentrate on some examples of certain relevance to biotemplated structures or to the sub-5 nm scale, namely energy-filtering transmission electron microscopy (EFTEM), X-ray microanalysis (EDX), X-ray photoelectron spectroscopy (XPS), and mass spectroscopy (MS) [Dujardin03,Reiss04,Grobert01,Falkner05,Lee05]. EFTEM is one of the most powerful tools for nanoanalytical applications since it allows the analysis of small specimen volumes with high sensitivity and lateral resolution in the nm-range, thereby providing local chemical information [Williams96,Leapman82,Berger92,Thomas02]. The resolution of this technique can be better than 1 nm, making it an ideal tool to study the chemical composition of nanoscale materials [Verbeeck04]. In contrast to the conventional TEM, in which scattered electrons are used for contrast generation, EFTEM selects electrons not only according to their intensity and scattering angle, but also according to their energy with an in-column or post-column energy filtering system (see also chapter 3 for the details). The chemical sensitivity comes from the characteristic atomic inner-shell energy-loss edges, which are used to map the elemental distribution. By combining TEM with EFTEM, which is automatically done in the experiments, both structure and chemical composition of nanomaterials are accessible and thereby enabling to understand specific nanoscale regions of a sample. It is expected that this will also help developing

theoretical models both for the synthesis and physical properties of the corresponding material. EFTEM has been used for chemical analysis of various nanomaterials; of particular relevance is here that Grobert et al. have reported a nickel/iron alloy (invar) formed inside carbon nanotubes [Grobert01], and that Reiss et al. have analyzed FePt nanoparticles on the rod-like M13 bacteriophage [Reiss04].

XPS utilizes photoionization and energy-dispersive analysis of the emitted photoelectrons to study composition and electronic state of the surface region of a sample [Belin05]. Since X-rays are very difficult to focus, analysis on the sub-μm scale can usually not be attained. However, one should note that the method is quite sensitive to surfaces and also gives very detailed chemical information (e.g. the oxidation state of the analyzed elements). XPS will become useful for analysis of TMV-templated structures whenever they assemble in high density; say 10% surface coverage, which was not yet achieved.

MS is based on producing, differentiating, and detecting ions in the gas phase with very high mass resolution. Measuring the mass of ionized molecules (and fragments) can provide indirect structural information that is otherwise hard to obtain, especially for the characterization of biomolecules [Siuzdak94]. MS has been successfully employed for the analysis of mutated TMV coat proteins [Schlick05] and even for measuring the mass of complete virions [Bothner04]. Again, local information is very hard to gain.

In contrast, X-ray microanalysis (EDX) in conjunction with conventional TEM or SEM can give well-localized chemical information of very high quality, both from a quantitative and a qualitative viewpoint [Williams96]. The submicrometer scale is quite easily attained, and in connection with scanning TEM (STEM), where the focused electron beam is scanned over the surface to give images, the resolution is much increased. Unfortunately, STEM tends to destroy biological samples, and for conventional EDX it is not possible to prevent radiation from microscope stages and other parts of the sample, for example, from the grid mesh of the substrate (Cu-TEM grid), hence analyses of copper and carbon are difficult. However, the chemical analysis of platinum, gold, and

silver nanoparticles around TMV particles [Dujardin03,Lee05], and for palladium and platinum distribution in the solvent channels of cowpea mosaic virions (CPMVs) crystals [Falkner05] are straightforward.

EDX and EFTEM are complementary: While EFTEM can detect all the elements in the periodic table, but is more sensitive to the light elements, EDX is especially sensitive to heavy elements. Neglecting experimental problems, EFTEM is quite often preferred over EDX, because it offers advantages for the analysis of thin specimens, usually higher spatial resolution than even STEM-EDX, higher detection sensitivity, and higher energy resolution [Leapman91]. Another advantage is that EDX detects only a part of the emitted X-rays. Therefore, the time required for recording an elemental distribution (an image) of high information content (high signal to noise ratio) may be too long to be practicable. In contrast, EFTEM collects all forward-scattered electrons, which can create element distribution maps faster than comparable EDX experiments, although each elemental map requires sequential recording of three maps at different energies [Leapman91,Williams96]. In this project, EFTEM was used as the main analysis tool for the chemical mapping of inorganic nanowires inside and outside of the TMV. In addition, EDX in conjunction with conventional TEM attachment was used for chemical analysis of size-enhanced gold nanoparticles attached exclusively to the ends of the TMV particles.

4.6.1 Elemental Mapping of Cu, Ni, and Co Nanowires

After metallization of Pd (II)-incubated TMV suspensions with ELD-baths, metal nanowires of ~3 nm diameter were observed (see chapter 4.3 and 4.4 for details). Figure 4.9 demonstrates the electron energy loss (EEL) spectra from copper, cobalt, and nickel nanowires. The $L_{2,3}$ white lines of cobalt and nickel can easily be observed. Here we must clarify that the innermost electron shell is called the K shell, the next the L shell, and so on. This terminology comes from the simple Bohr

theory of atomic structure where electrons are circulating the nucleus in discrete shells (K, L, M, etc., where K=1s, L=2s and 2p, M=3s, 3p, 3d, etc.). All the shells except K may themselves have subshells; hence cobalt and nickel have L_2 and L_3 subshells, in short $L_{2,3}$ [Williams96]. The EEL spectra in Figure 4.9 were acquired from a region a few μm^2 wide, in which agglomerates on the TEM grid surface and nanowires within the central channel of TMV particles were found. Note that even for this large scale, the elemental signals are restricted to the electron-illuminated region in the focus of the microscope. For example, in the cobalt EEL spectrum no copper signal was observed from the TEM grid, which contains several micrometer wide copper lines (carbon coated Cu-TEM grid). This is not the case in EDX measurements in which the grid materials can contribute to the signal generation (see chapter 4.6.3). After ensuring that the element of interest (for example cobalt) was on the TEM grid, elemental mapping of nanowires was performed in sub-μm^2 regions.

Figure 4.10a shows a bright-field TEM image of a copper nanowire (dark line) synthesized within the hollow channel of a single TMV particle. The diameter and the length of the wire are measured to be approximately 3 nm and 30 nm, respectively. Note that the grey shaded region with 300 nm length and ~20 nm width corresponds to a single TMV particle, while the dark line within the particle indicates the wire. Small clusters attached to the external surface of the virion (a few nanometers in diameter) originate from uncontrolled deposition of copper during the ELD reaction. The exact diameter of the nanowires is difficult to measure since the borders of the nanowires are often smeared out (the resolution of the TEM is around 0.27 nm), which could be attributed to the carbon support below the sample.
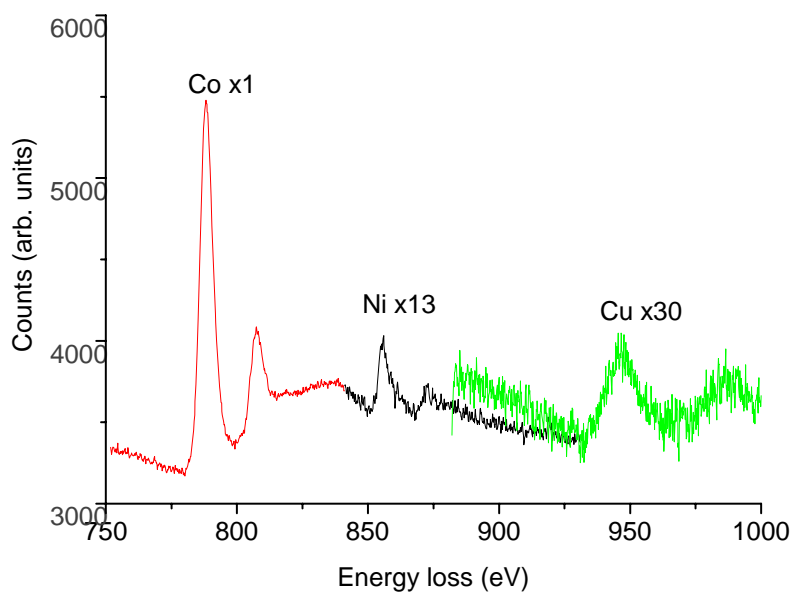
Figure 4.9: Three EEL spectra of Co, Ni, and Cu from the samples containing TMV treated with Co, Ni, and Cu deposition baths, resulting in ~3 nm diameter nanowires. The metallized TMV particles were adsorbed on TEM grids. Each spectrum shows the $L_{2,3}$ ionization edges characteristic for each element (the nickel and copper signals are magnified). Counts represent the electron intensity. The zero-loss peak (at 0 eV) and plasmon losses (around 50 eV) were not recorded.

The electron spectroscopic image revealing the copper elemental distribution across a single TMV particle is displayed in Figure 4.10d, which was obtained from the element-specific signal at the Cu $L_{2,3}$ edges and the two pre-edge images for background subtraction (see also Figure 4.9 for the electron-energy loss spectrum). Figure 4.10g shows the integrated line profile from the box-shaped area indicated in Figure 4.10d.
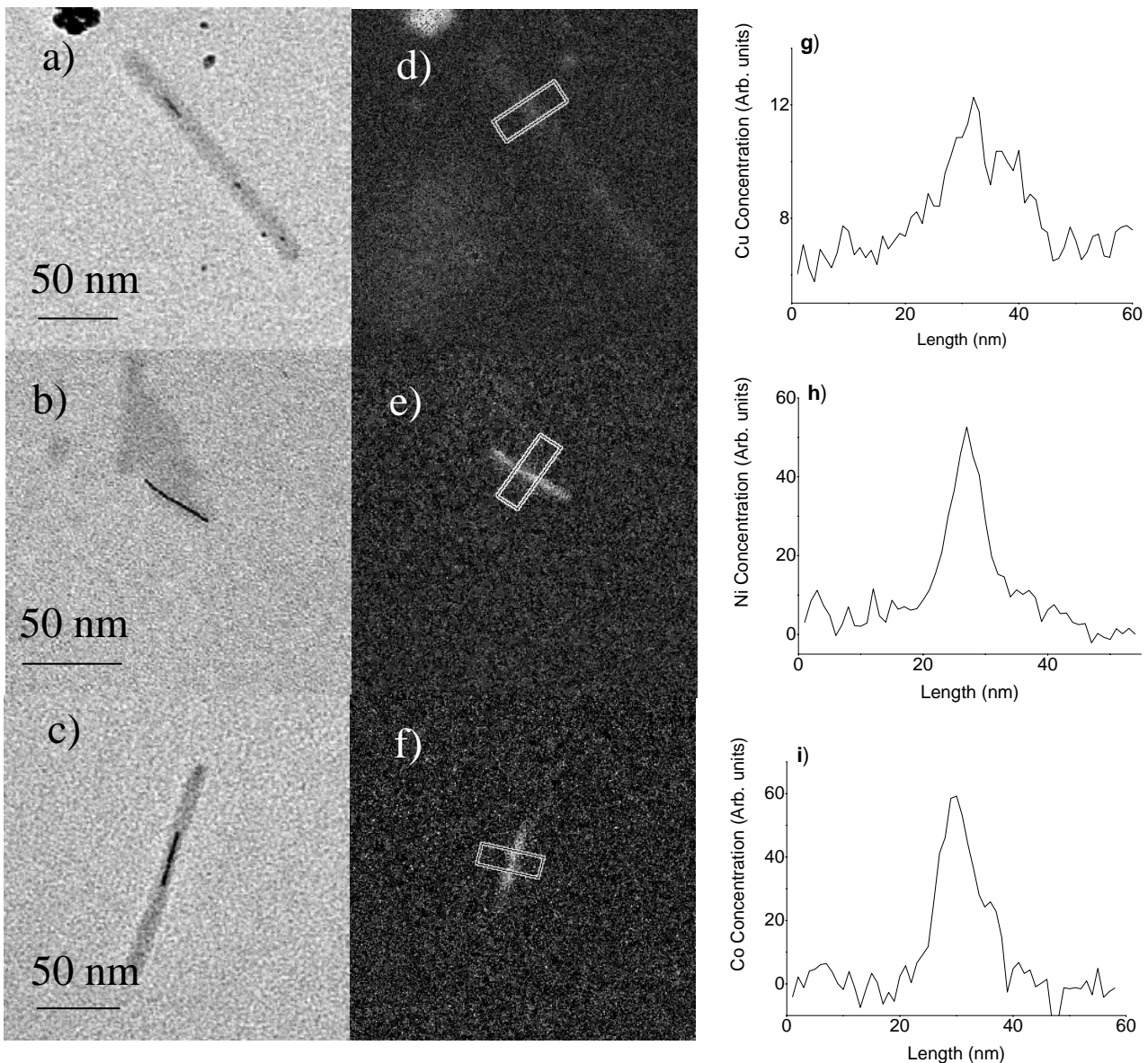
Figure 4.10: Elemental maps of copper, nickel, and cobalt nanowires by using EFTEM. Bright-field TEM image of **(a)** copper, **(b)** nickel, and **(c)** cobalt nanowires within the central channel of a single TMV particle are complemented by the elemental distribution images (**(d)** copper, **(e)** nickel, and **(f)** cobalt) recorded with the three-window technique (Cu $L_{2,3}$ edge at 931 eV, Ni $L_{2,3}$ edge at 854 eV, and Co $L_{2,3}$ edge at 779 eV). Integrated line profiles (**(g)** copper, **(h)** nickel, and **(i)** cobalt) show the compositional line trace of elements from the marked areas.

Equivalent data are also shown for nickel and cobalt (Figure 4.10). The wire diameters are always ~3 nm, and the lengths are approximately 65 nm for both the nickel and cobalt nanowires shown here. All grey-shaded regions in the bright field images are interpreted to represent intact or – in

case of larger ill-defined spots such as in Figure 4.10b - destroyed TMV particles. At least one of these regions envelops the dark line, which designates a nanowire inside a TMV channel.

The elemental maps prove conclusively that the deposited metal is indeed present in the channel only. The wire shape corresponds very well to the elemental map, with one difference: When one tries to measure wire diameters not from the bright field images (giving 3 nm), but from the corresponding EFTEM line profiles, one finds values well above 3 nm (Figure 4.10a, 10b and 10c). Moreover, the full width at half maximum (FWHM) values in the integrated line profiles for the copper, nickel, and cobalt nanowires (13.5 nm, 7.8 nm, and 7.1 nm, respectively) depend on the element. While this phenomenon is in part due to the instrumental drift during the EFTEM measurements (sequential recording of pre- and post-edge maps), the main problem is clearly the decreased signal to noise ratio for nickel and especially for copper. A closer look at the EEL spectra (Figure 4.9) shows that the shape of the edges and also the relative emission intensities differ very much from element to element. In fact, the intensities can be used for semiquantitative elemental analysis. The basic formula for comparing two elements A and B is:

$$N_A/N_B = I^A \sigma^B / I^B \sigma^A \tag{4.5}$$

in which N is the number of atoms per unit surface area, I is the intensity integrated at the K edge, and σ is the ionization cross-section. Here the important conclusion is that certain elements such as copper (compared with e.g. nickel), have such low ionization cross sections, that their intensity is surprisingly low, even for the same amount of material ($N_A = N_B$; this condition was approximately fulfilled for Figure 4.9). In our experiments we tried to use the same parameters for elemental mapping of nickel, cobalt and copper nanowires. We assume that all the nanowires within the central cavity of the TMV particles have a similar number of atoms per unit length for each particular element (copper, nickel, or cobalt).

The higher relative noise level means that line traces "smear out", explaining the large FWHM value especially for copper. A reason for the low relative intensity for the copper EFTEM is that other elements, e.g. nickel and cobalt, exhibit intense and sharp so-called "white lines" at their

respective edge onsets, due to the excitation of L electrons into unoccupied d states [Leapman82,Williams96] (see Figure 4.9). Note that the L shell electrons do not escape from the atom, but end up in the d states. In contrast, no pronounced features occur at the Cu $L_{2,3}$ edge since the 3d shell is fully occupied [Leapman82] (Figure 4.9). In addition, the Cu $L_{2,3}$ edge lies at the highest energy loss (931 eV) among the investigated materials, and thus the intensity is lower [Leapman82,Williams96]. Altogether, the diminished signal/noise ratio increases the FWHM, thus making EFTEM analysis of copper nanostructures comparatively difficult.

In principle, the signal to noise ratio of elemental maps can be increased with longer acquisition times and/or higher beam currents. However, long acquisition times can result in problems caused by the drift of the samples during the acquisition of the pre-edge and post-edge images, leading to artefacts in the calculated elemental maps. Approximately 60 seconds were an optimal acquisition time for obtaining the highest possible contrast. Measurements with a higher beam current (also leading to additional artefacts in the images), have the disadvantage that the nanowires are damaged. We also tried to operate the Zeiss 912 at 60 kV instead of 120 kV to obtain a better contrast, but the data quality could not be improved.

4.6.2 Elemental Mapping of Fe-Co-Ni Nanowires

In chapter 4.4, the synthesis of nanowires within the central channel of TMV particles from an ELD bath containing Fe(II), Co(II), and Ni(II) is discussed in detail. Here we explain the local analysis of the chemical composition of these nanowires (see chapter 4.2 for the used baths).
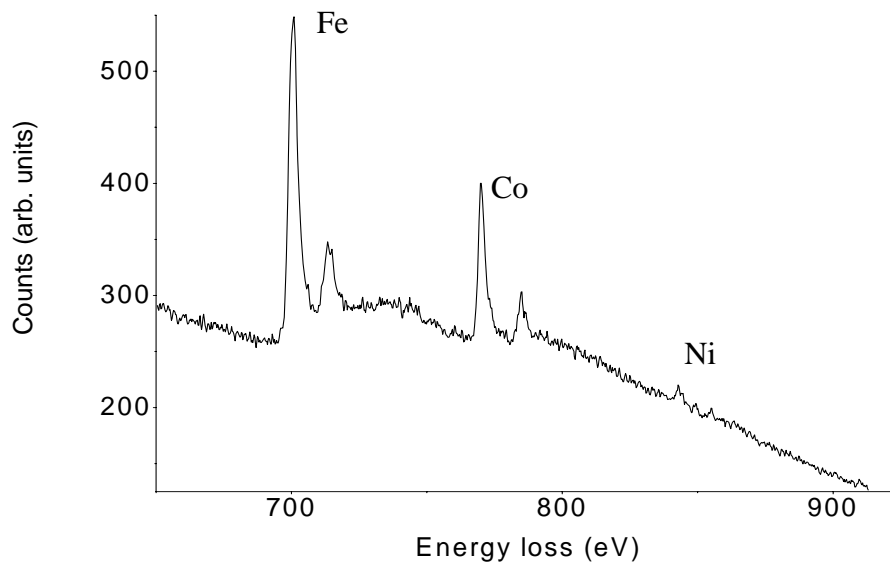
Figure 4.11: EEL spectrum of a CoFeNi sample on a carbon coated Cu-TEM grid surface showing the $L_{2,3}$ ionization edges at characteristic energy losses: Fe $L_{2,3}$ at 708 and 721 eV, Co $L_{2,3}$ at 779 and 794 eV, and Ni $L_{2,3}$ at 855 and 872 eV.

Figure 4.11 presents the electron energy loss spectrum of FeCoNi-metallized TMV. The illuminated area used for the EEL spectrum acquisition contained a nanowire within the central channel of the TMV particles and also some metal agglomerates produced during electroless deposition. Literature values of ionization edges of Fe, Co, and Ni show that the energy loss peak at 854 eV for Fe, 779 eV for Co, and 854 eV for Ni can be attributed to the corresponding elements (see also Table 4.1) [Williams96]. The spectrum shows sharp "white lines" that correspond to L_2 and L_3 edges of Ni, Co, and Fe (see above): The L shell electrons end in unfilled d states, which are present in Fe (6 electrons in the d orbital), Co (7 electrons in the d orbital), and Ni (8 electrons in the d orbital)[Leapman82]. As usual, the edge ionization energy depends very much on the atomic number Z because the L shell electrons require much more energy for ejection of electrons as *Z* (atomic number) increases (stronger interaction with the nucleus) [Williams96]. So the edge energy of Ni (E_{Ni}) is higher than that of Co (E_{Co}) and Fe (E_{Fe}), $E_{Ni} > E_{Co} > E_{Fe}$.
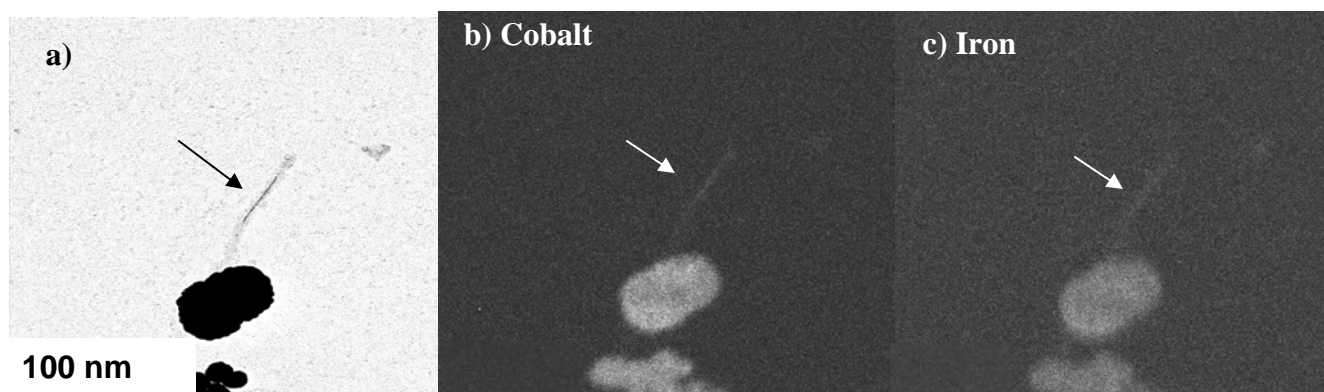
Figure 4.12: Elemental maps of a CoFe nanowire by EFTEM. **(a)** TEM micrograph of a CoFe nanowire within the central channel of a TMV particle. The dark line corresponds to the nanowire, ~3 nm in diameter, approximately 100 nm in length. The dark-grey region (the viral coat protein) around the nanowire is a single TMV particle. **(b)** Cobalt map, **(c)** iron map.

Figure 4.12a shows a bright-field TEM image of a nanowire (dark line) within the central cavity of a single TMV particle. The diameter and the length of the nanowire are approximately 3 nm and 100 nm, respectively. The grey shaded region with 200 nm length and ~20 nm diameter corresponds to a part of a virion attached to a large metal nanoparticle (~100 nm in diameter), while the dark line within the particle indicates the nanowire. The electron spectroscopic images revealing the Co and Fe elemental distribution across the single TMV particle in Figure 4.12a are displayed in Figures 4.12b and c, respectively. They were obtained from the element-specific signal at the Co $L_{2,3}$ and Fe $L_{2,3}$ edges (see also Figure 4.11 for electron-energy loss spectra of the elements). The nickel elemental map did not show any intensity indicating that the amount of nickel in the nanowire is very low (within our noise level, the amount is zero). The length of the nanowire (~100 nm) in Figure 4.12a was reproduced in both Co and Fe elemental maps. The large nanoparticle below the nanowire also reproduces the respective bright field image. Moreover, chemical analysis from the EEL spectra showed that both the deposited material on the TEM grid and the nanowire

within the virion included approximately 90% Co and 10% Fe (the relative concentrations were calculated with equation 4.5). The nanowires remained unchanged for a long time (weeks) and further studies, like EFTEM measurements, were performed without destruction of the wires.

The first important result is that not all bath constituents are deposited, even when they can be deposited (thermodynamically allowed and also sufficiently fast) in absence of the other constituents. In other words, ELD of a mixture of metals is not (or not generally) an additive process with independent reactions; rather the reactions influence each other, here for nickel to an extreme extent. This is to our knowledge the first chemical analysis of an alloy for nanoscale ELD. One should note that even for the independent reactions, the kinetics differ very much for each element, and one would expect that the element with the most negative reduction potential shows the smallest deposition rate. Most surprisingly, this is not Ni, but Fe, a strong and direct indicator for interdependence (see also chapter 4.4 for further discussions).

The obvious choice of leaving out nickel from the start did produce the expected wires within the central channels of TMV particles, but the wires deteriorated after two weeks in air, which is untypical for any of the other wires: Small clusters were observed, and no nanowires could be detected any more. The simplest interpretation is the oxidation of the CoFe alloy since the samples were stored in air. In this case, nickel should work as corrosion inhibitor. Myung et al. [Myung01] studied the influence of Ni on bulk CoFe alloys and found that corrosion resistance of electrodeposited CoFe films was an order of magnitude lower than that of CoNi and NiFe films, meaning that Ni plays a crucial role in increasing the corrosion resistance of materials; we believe that this result can be scaled down to the nanoscale (see also chapter 4.4). Naturally, the complex nature of the nanoscale system does not allow quantitative calculations on the corrosion. However, it is now well established that at least water and most ions can only reach the TMV channel from the openings, not by diffusing through the coat protein.
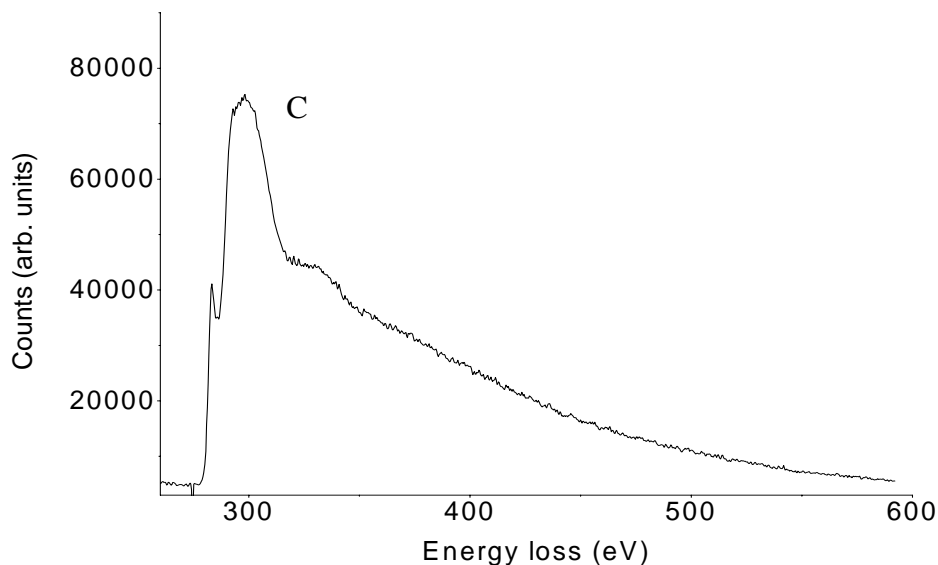
Figure 4.13: EEL spectrum of pristine TMV particles on a Cu-TEM grid. The broad peak centered at 284 eV is the carbon K-edge.

Further investigations of oxidation or other disintegration processes of different nanowires (for example Co, Ni, and CoFe), require an elemental composition study of pristine TMV particles first. Figure 4.13 shows the EEL spectrum of TMV particles on a TEM grid. Note that only the carbon K-edge, but not the oxygen K-edge at 532 eV, can be observed in the EEL spectrum. The TMV particles and the carbon coated Cu-TEM grid contribute to the carbon signal. EFTEM can analyze this signal better when it is localized, e.g. by the shape of TMV: Figure 4.14a shows a bright-field TEM image of TMV particles (dark grey lines). TMV particles are in most cases aggregated side-to-side and end-to-end. The electron spectroscopic images showed only the presence of carbon in the TMV particles (Carbon K-edge at 284 eV), Figure 4.14b. The carbon map closely reflects the bright field TEM image in Figure 4.14a., so contributions from the TEM grid form the background.

For these measurements, the instrumental drift is of relevance, so it will be discussed in some detail: During the EFTEM measurements, the carbon map does not contain all of the TMV particles in Figure 4.14a, but some additional ones (lower part). This is a result of thermal effects, which cause the sample to move during the electron beam exposure. The acquisition of a spectrum image takes only 60x3 seconds, but the drift causes obvious displacements. From this displacement in Figure 4.14, the drift velocity can be calculated to be approximately 40 nm/min towards the upper part of the image, which is unusually large. In order to decrease the drift in such cases, the specimen can be cooled.
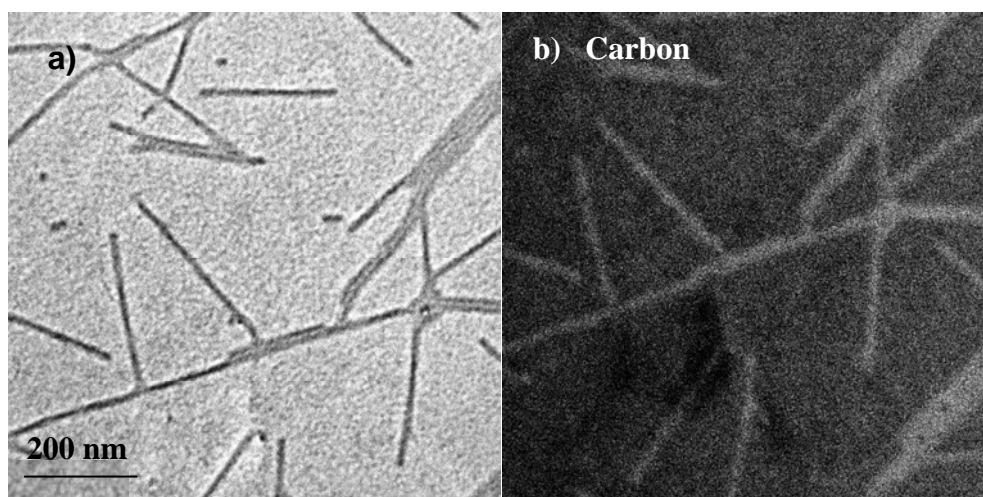
Figure 4.14: Elemental maps of pristine TMV particles by EFTEM. **(a)** TEM micrographs of TMV particles. Virions are distributed randomly on the Cu-TEM grid surface. **(b)** Carbon map of the virions.

In accordance with the EEL spectrum in Figure 4.13, oxygen and nitrogen signals (O K-edge at 532 eV and N K-edge at 401 eV) were not observed in elemental maps (data not shown here). Since TMV consists of C, N, O, H, and S, and since the TEM images correspond very well to all published data, probably the concentrations of oxygen and nitrogen are too low to be detected.

With this background, one should be able to detect nanowire oxidation simply by finding a clear oxygen signal that is spatially correlated with the respective metal signal (see chapter 5.4 for a good example), and any weak oxygen signal in the elemental map would be attributable to an (partial) oxidation of the wires. However, first experiments were inconclusive: For one sample, cobalt nanowires within virions showed a very weak oxygen map; however, the data could not be reproduced (in another sample, no oxygen signal was found by EFTEM). In fact, corrosion by oxygen and water is expected to start at the two ends of a nanowire since the protein coat is practically impenetrable. The expected dumbbell-shaped oxygen map was never detected. Together with HRTEM of nickel wires (see chapter 4.4.1), we can say that there are clear indications that the wires are not oxidized, although a final proof was not yet achieved.

4.6.3 EDX Analysis of Au Structures

In chapter 4.5, we discussed the selective size-enhancement of gold nanoparticles (Au-nps) (6 nm in diameter) at the ends of TMV particles using the ELD of gold. ELD, especially in the presence of biological material like TMV, might result in a mixture of the desired substance (gold), incorporated molecules (additives) and probably parts of disintegrated TMV. By energy-dispersive X-ray (EDX) analysis, here we show that the size-enhanced Au-nps are composed solely of gold.

Figure 4.15a shows 6 nm Au-nps selectively attached to the ends of TMV particles. Each virion is around 287 nm in length and contains Au-nps at the ends of the TMV. These Au-nps, adsorbed on TEM grids, were size-enhanced by using ELD of gold with the same procedure used for the size-enhancement of Au-nps on oxidized silicon surfaces (see chapter 4.5), resulting in very similar structures (Figure 4.15b). In the cases of virions with Au-nps at both ends, well-defined dumbbell-shaped structures (an object with two metallic spheres and one rigid rod in between) are produced.
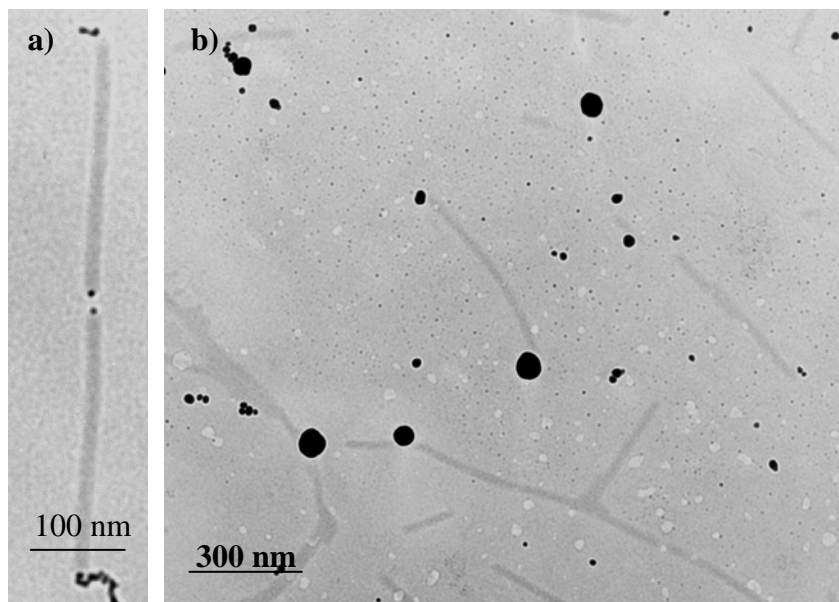
Figure 4.15: TEM micrographs of **(a)** 6 nm Au-nps attached to the ends of two TMV particles (each of them ~287 nm in length) **(b)** TMV particles after enhancement of the attached Au-nps by electroless deposition of gold. The diameters of the enhanced gold structures are between 20 to 60 nm. This is a typical region from which EDX spectra were acquired.

From the regions comparable to Figure 4.15b, in which at least one TMV particle contains enlarged gold structures (''balls'') at both ends, energy-dispersive X-ray (EDX) spectra were obtained (Figure 4.16). The EDX analysis was performed using a high-energy electron beam (200 kV). Briefly explaining the EDX, in the specimen the electron beam excites some of the atoms electrons creating empty energy levels in the atoms [Williams96]. A higher-energy electron from an outer shell occupies the empty position. The energy is released by emitting an X-ray quantum or (preferably in light atoms) Auger electrons, which are characteristic for each atom in the specimen. Therefore, a typical EDX spectrum displays peaks corresponding to energy levels from which the X-rays are emitted.
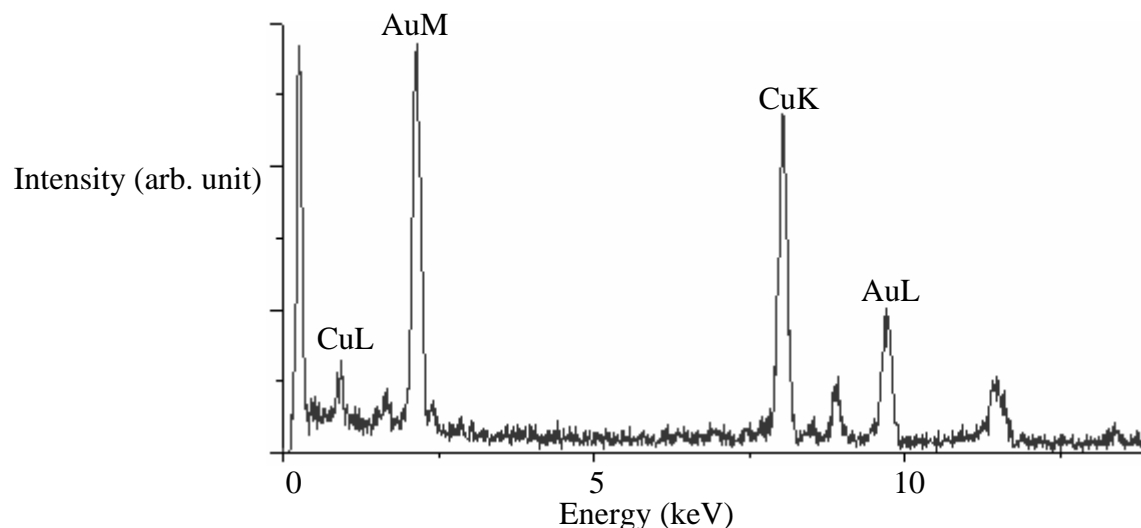
Figure 4.16: An EDX spectrum from the size-enhanced gold nanoparticles at the ends of TMV particles on a carbon coated Cu-TEM grid surface. The strong lines of Au-M and Au-L shells support the presence of gold in the enlarged structures at the ends of the TMV particles.

The X-ray signals (element specific) from M and L shells of gold support the presence of gold in the produced structures. Since lower atomic number elements have fewer filled shells, they have fewer X-ray peaks and therefore EDX is very sensitive for heavy elements [Williams96]. For instance, carbon has only one peak (K shell X-rays at 0.282 keV), while gold has two peaks (K and L).

One apparently simple fact, the presence of sharp peaks, is on closer inspection interesting: Very small gold nanoparticles (< 2 nm) have considerable energy levels (and thus catalytical properties) that are different from larger particles, which correspond to bulk gold. The clear observation of two peaks only means that the sample, especially the virion, is not coated by very small nanoparticles, which could be a problem for further chemical modification and for electrical measurements. Furthermore, the absence of other elemental peaks (except of course carbon) shows that the gold particles are pure. Given the relatively low sensitivity for oxygen and nitrogen, one can at least exclude that a huge aggregate like a denatured virion is the nucleation core for a gold structure. The lowest energy X-ray peak originates from carbon, and is largely due to the carbon-coated polymer

grid; it is impossible to extract those parts of the signal that originate from virions. Finally one should note that TEM grids always show copper signals (CuL and CuK), originating from the copper backbone of the grid. Thus a similar analysis will be very difficult for copper nanostructures, while other analyses are not affected.

4.7 Electrical Properties of TMV rods

The integration of biomolecules in electronic elements attracts great attention in recent years. The advantages of biomolecules are the unique structures and self-assembly properties. The reasons are the possibility to study the basic scientific questions and the prospective potential for applications. DNA is one of the mostly studied for these purposes [Porath00,Storm01]. For example, Keren and co-workers have demonstrated a new type of lithographic technique (a sequence-specific molecular-lithography technique) for growing molecular scale electronic devices with DNA molecules as templates [Keren02]. Metal coatings at the chosen locations on the strands of DNA have been demonstrated [Keren02]. In this technique, RecA protein is used as a protecting resist, similar to polymethylmetacrylate (PMMA) used in electron beam lithography processes. In addition, several research groups have reported the conducting, semiconducting, and insulating transport behaviors of DNA molecules at different experimental conditions [Fink99,Porath00,Storm01]. Fink and co-workers reported conductivity (I-V) measurements across a few DNA molecules associated into single ropes. These ropes were at least 600 nm long and showed a current flow with an applied voltage [Fink99]. In addition, Pkahata and co-workers studied the I-V measurements across a DNA film and detected current flow between the electrodes [Okahata98]. Finally, it has been concluded that insulating behavior of DNA is dominant in most of the experimental conditions [Storm01]. Discrepancies in transport measurements mainly arise from different sample preparations (films, ropes, single molecule…) and also measurement conditions. Nevertheless, the construction of electronic circuits based only on native DNA remains problematic because of the high resistance of the DNA molecules. In the same way, it has been expected that

TMV rods show insulating properties. In order to bypass this problem, DNA molecules have been metallized to install electrical functionality onto it [Braun98,Richter01]. For instance, Braun and co-workers presented a new approach in which they fixed a DNA molecule between two gold contacts placed on a silicon oxide surface and utilized it as a template for the fabrication of silver nanowires with diameters around 100 nm [Braun98]. In a similar way, Richter and co-workers, demonstrated that 50 nm thick palladium nanowires grown on the DNA template exhibit ohmic transport behavior at room temperature [Richter01]. These transport experiments of DNA molecules in different conditions could be a reference system for contacting other biomolecules like TMV before and after the metallization experiments.

In this part of the work, electrical transport measurements on TMV particles (towards contacting nanowires within the virus) contacted between the metallic electrodes on insulating SiO_2 surfaces are described. Transport properties of the TMV rods have not been yet reported in the literature. The structures have been prepared using standard electron beam lithography techniques (see also chapter 3 for details). For these measurements, TMV particles are deposited from an aqueous solution onto a SiO_2 surface. The surfaces are patterned with closely spaced thin metallic (gold) markers, which are used as a coordinate system. The markers area is surrounded by smaller contact pads that are connected to larger pads. These areas are large enough to be bound by the gold wires, which facilitate contact to the electrical equipment (see also details in chapter 3). The electrodes connecting the TMV particles to the inner contact pads are fabricated by electron beam lithography and subsequent lift-off processes. For the contact electrodes, a 17 nm thick gold film is used (see Figure 4.17). Underneath the gold electrodes, there is a 3 nm thick layer of chromium, which is used to increase the adhesion to the SiO_2 surface. In this way, TMV rods are contacted at their ends with a high accuracy. An much simpler way of contacting a nanowire, well known from early research on carbon nanotubes (CNTs), is adsorption from a suspension directly onto prepatterned finger-like electrodes [Tans97]. Although this method sometimes works for very long molecules

like CNTs, it often results in too high contact resistance, and this can be expected for TMV, too. In addition, for the much shorter TMV (300 nm), the probability of bridging two contacts is much lower.

Figure 4.17 shows an AFM image of a device with three end-to-end assembled TMV particles between the gold electrodes spaced by 250 nm. This is an example of a typical device used in transport measurements. The apparent height of the TMV particles is about 10 nm, and the width is about 60 nm. These values are typical for TMV particles adsorbed on a SiO_2 surface [Knez04]. From the height, width, and length determined from the AFM images, it can be concluded that the TMV particles are indeed connected between the gold electrodes.

500 nm
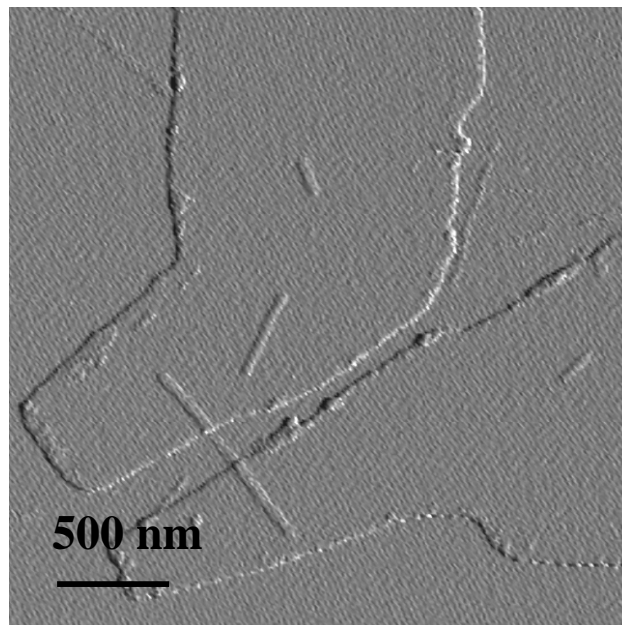
Figure 4.17: AFM image (non-contact mode, error signal) of the TMV particles and the two contacting gold electrodes on a SiO_2 surface. The long TMV rod (~900 nm in length corresponding to 3 TMV particles) is covered on both ends with the gold film. The gold electrodes, ~500 nm wide then increasing to 1.5 μm, are separated by ~250 nm on the SiO_2 surface. The thickness of the evaporated gold film on the insulating SiO_2 surface is around 20 nm.

Electrical characteristics of TMV were investigated in a three-terminal device configuration (see chapter 3 for details). Two terminals contacting the TMV particles (labeled as source (S) and drain (D)) were used to apply a voltage along the virus rods, whereas the third terminal (labeled as gate (G)) was electrically insulated from the virus rods and used to manipulate the electrostatic potential of the contacted virus rods. The bias voltage between the source and drain electrodes were increased up to 10 V (between the source and the drain electrodes in the device) and the observed currents remained below a noise level of about a few pico amperes. Therefore, no current flow was observed for this device, meaning that TMV adsorbed on a SiO_2 surface showed insulating behavior under this condition. More than five samples were measured in a similar way and in all the TMV connected between the gold electrodes no conductivity of TMV was observed. The gate voltage was set to zero during the transport measurements in order not to electrostatically dope the TMV molecules with additional charge carriers. However, in a separate experiment gate voltage of the device was increased to several volts but there wasn't any change in the transport behavior of contacted virions at all. In contacted DNA, Storm and co-workers also did not see the effect of a gate voltage on the conductance of the DNA [Storm01].
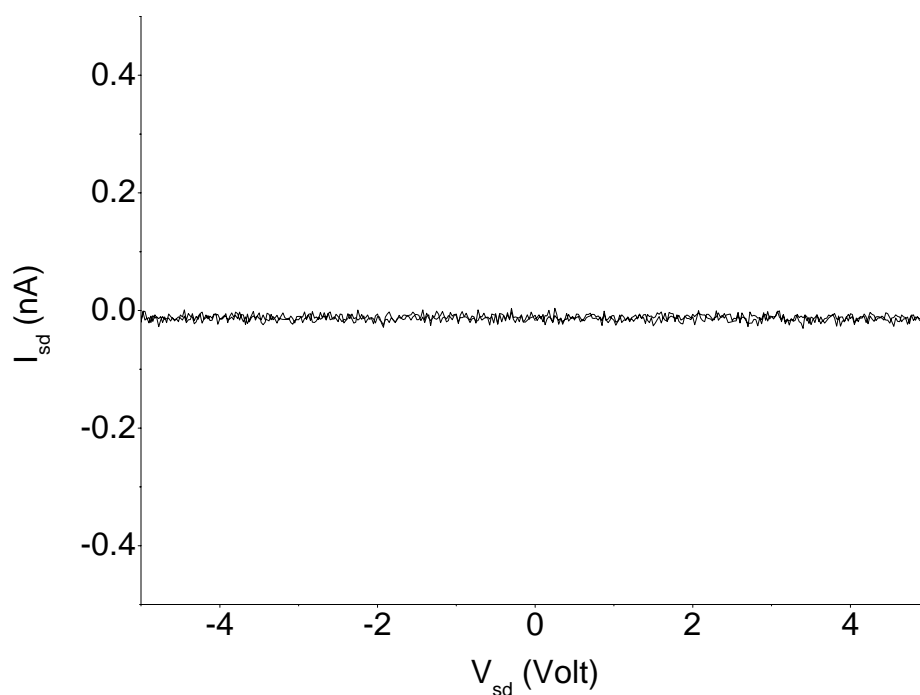
Figure 4.18: Current-voltage (I-V) curves measured at room temperature and in vacuum (4-6x10$^-$ ^{5}mbar) on TMV rods trapped between the two gold nanoelectrodes (see also Figure 4.17).

During electron beam lithography processes, the operating temperature was always smaller than 60°C meaning that TMV particles were preserved without denaturation at high temperatures. Heating to high temperatures (above 90°C) can disrupt attractive intermolecular forces (ionic interactions, hydrogen bonding, Van der Waals forces, etc.) in the virus coat protein. This occurs because heating increases the kinetic energy and causes the molecules to vibrate to such an extent that bonds rupture. Note that in standard electron beam lithography experiments poly (methyl methacrylate) (PMMA) is annealed at 160°C to remove solvent molecules present in the polymer matrix. In addition, the usual solvent 1-methyl-2-pyrrolidone was replaced by acetone, which is compatible with TMV. All the electrical measurements were performed in vacuum (4-6x10^{-5}mbar); therefore, the effect of condensed water on the surface was eliminated. Recently, Ostmann and co-workers investigated the conductivity of DNA in ambient conditions and observed an exponential increase of the conductivity of the DNA molecules (connected between the gold nanoelectrodes)

with increasing humidity [Ostmann06]. They attributed the increase at high humidity levels to water molecules accumulated at the phosphate backbone of DNA. In a similar way, the conductivity of TMV could be increased by controlled increase of the humidity. The insulating behavior of the TMV rods might be very useful for future applications such as virus-based transistors. This could be realized by contacting the metal nanowires inside the virus. Before contacting the nanowires, gold particles can be attached to the ends of the virus and size-enhanced (see chapter 4.5) thereby allowing a better contact. Another electrode can be deposited in the middle of the virus. The coat protein of the virus could then act as a gate insulator. Alternatively, nanowires without the coat protein around can be contacted. For such an experiment, an enzyme (Proteinase K) can be used to remove the coat protein of the virus. Indeed, such experiments were performed on a carbon coated Cu-TEM grid surface and nickel nanowires without coat protein were observed (see chapter 4.4).

4.8 Conclusions

From the experimental results described in this part of the work, the following conclusions can be drawn:

(a) A variety of materials (Co, Ni, CoFe, Cu, and Au) can be selectively synthesized within the central channel, on the outer surface as well as at the ends of the TMV particles. Therefore, TMV can act as a template for the synthesis of a variety of metal nanostructures. Depending on the type of material being deposited on the specific locations of the virions, one can expect a variety of physical properties (magnetic, optical, and electrical).

(b) A Cu ELD bath compatible with TMV particles was developed and the virions were metallized using this bath. The lengths of the copper nanowires can reach up to 150 nm. In a similar way, a Ni ELD bath was developed for the deposition of Ni within the central channel of virions. In a further experiment, CoFe alloy nanowires were produced within the central channel of the virus after

addition of Fe(II) to the cobalt ELD bath. In this manner, Co, Cu, Ni, and Fe can be introduced to the central cavity of the TMV particles using the ELD methods. Furthermore, high-resolution TEM observations revealed that nickel nanowires within the central channel of the TMV particles are crystalline with an inter plane distance of ~2.10 Å. It has been concluded that the nickel nanowire consists of a metallic Ni core surrounded by a passivating very thin NiO shell.

(c) Energy filtering transmission electron microscopy (EFTEM) proves that the inorganic nanowires within the 4 nm central channel and on the external surface of the tobacco mosaic virus (TMV) particles synthesized by using ELD are indeed composed of the corresponding metal elements present in the ELD baths (local chemical information). While the elemental maps of copper, nickel, and cobalt nanowires reproduce nicely the lengths of the nanowires measured by conventional (bright-field) TEM, the diameters (~3 nm) appear to be two to three times enlarged (copper, nickel, and cobalt wires have FWHM values of 13.5 nm, 7.8 nm, and 7.1 nm, respectively). The reason is that the EFTEM sensitivities for cobalt and nickel are higher than for copper, which can be traced back to the spectral features of the electron absorption edges and hence to the electronic properties of the copper atoms (filled d shell).

(d) By using EFTEM, it has been confirmed that ELD with a mixture of Co and Fe produces indeed a 3 nm wide CoFe alloy wire, located within the central channel of the TMV particles, whose chemical composition is about 90:10 Co:Fe. This does not reflect the ratio in the ELD bath, which must be due to interdependent deposition processes of Co and Fe. Moreover, when Ni is added, the air stability of the virus-nanowire composite is improved. This corrosion inhibition behaviour was until now known for bulk samples, but not on the nanoscale, and it requires only very small amounts (< 1%) of Ni, which cannot be detected by EFTEM.

(e) Elemental mapping of pristine TMV particles indicates that it is only possible to detect carbon in the coat protein of TMV particles (no oxygen and nitrogen). Due to the high lateral resolution of EFTEM, the carbon signal can be distinguished from the carbon signal of the underlying TEM grid.

This result is the basis for detailed investigations of possible corrosion/oxidation of the nanowires within the central channel of TMV particles. Preliminary results are inconclusive, but point towards good stability at least for some hours in air.

(f) Au-nps (6 nm) were selectively attached to the ends of the TMV particles and size-enhanced by electroless deposition of gold. Removal of the coat protein of TMV using Proteinase K enzyme and successive incubation with the gold sol resulted in self-assembly of Au-nps around the TMV-RNAs. Therefore, the RNA of the TMV plays an important role in the selective assembly of the Au-nps. It is believed that the heterocylic aromatic bases of the RNA interact with the Au-np surface (replacing citrate molecules on the Au-np surface) and that this is the main driving force for the selective attachment of Au-nps to the ends of the TMV particles. Therefore, without using antibodies (Au-tagged antibodies), chemical or genetic modifications of the virus, still excellent selectivity can be achieved in a very simple way. Furthermore, dumbbell-shaped structures, which might be very useful in contacting nanowires within the central channel of the TMV particles, were generated using the gold ELD process. EDX analysis confirmed that the enlarged Au-nps (20-60 nm) consist of gold, which was expected.

(g) By using electron beam lithography, TMV particles can be connected between the gold electrodes at temperatures (smaller than $60^{o}C$) lower than degradation of virions. Transport measurements demonstrated that TMV particles show insulating properties at room temperature and in vacuum ($4\text{-}6 \times 10^{-5}$mbar). Similar experimental conditions could be also used for contacting nanowires within the central channel of the TMV particles for future experiments.

CHAPTER 5

Mineralization of TMV for ZnO Nanostructures

In this chapter, mineralization of the Tobacco Mosaic Virus (TMV) particles for the synthesis of zinc oxide nanostructures is described. By using the electroless deposition method, zinc oxide, a well-known wide band gap semiconductor, has been deposited on the external surface of the TMV rods. The mechanism of the zinc oxide deposition process is discussed in detail. The chemical composition of the deposited material has been analyzed on the nano-scale by using energy-filtering transmission electron microscopy (EFTEM). Besides that the optical properties (cathodoluminescence) of the ZnO rods are explained.

5.1 Introduction

The synthesis and characterization of nanometer-sized semiconductor structures, and the determination of their size dependent physical properties represent an enormous technical challenge to many areas of science and technology. In the nanometer regime, where the extensions of the electron and hole wave functions are constrained by the particle size, and therefore the electronic and optical properties are in a drastic manner different from the bulk material [Alivisatos96]. For example, the band gap of a semiconductor such as CdS can be tuned from its bulk value of 2.5 eV

to about 4.5 eV for ~2 nm sized clusters [Alivisatos96]. This size quantification effect can be qualitatively realized by the simple quantum mechanical particle-in-a box problem in which upon decreasing the size of the box, the energy separation between the various levels increases due to the confinement of a particle in a small space. This property of the materials can be used for potential applications in various electronic and photonic devices. In this regard, zinc oxide (ZnO) (a wide band gap semiconductor) is of great interest in the optical, and electronic industries [Huang01]. Recently, it has attracted increasing attention as a room-temperature ultraviolet light-emitting material because of its wide band gap energy of 3.3 eV and high exciton (the bound electron-hole pair) binding energy of ~59 meV, which ensures that excitonic emission mechanisms are significant at temperatures well above room temperature [Huang01]. This exciton binding energy is much larger than the room temperature thermal energy (26 meV), suggesting that the electron-hole pairs are stable even at room temperature. Therefore, efficient UV light emitting diodes (LED) and laser diodes (LD) operating at room temperature can be expected. Small diameter ZnO nanowires are expected to further lower the laser emission threshold since quantum effects result in enhancement of density of states near the band edges and radiative recombination due to carrier confinement [Alim05]. Huang et al. have reported a novel synthesis method for ZnO nanowires by a vapor transport and condensation process in which the ZnO nanowire was selectively grown below the Au catalyst particles attached to sapphire substrates (The ZnO precursor dissolves in the gold catalyst and epitaxially grows below the gold catalyst.), and they obtained ultraviolet emission at room temperature [Huang01]. Ultraviolet lasing at room temperature from the vertically aligned ZnO nanowires was demonstrated [Huang01]. However, these growth processes require heat treatments at high temperatures, which can prevent embedding the ZnO components in circuit boards because of the high preparation temperatures.

A special way of synthesizing ZnO structures on surfaces is the use of electroless deposition (ELD) (and also galvanic or electrodeposition) [Izaki97,Izaki96] (see also chapter 3 and 4 for details of ELD). Note that here ELD does not refer to the reduction of a metal cation, but merely to the

presence of a reductant; in fact, the ELD mechanism of ZnO deposition is not yet completely understood. Izaki et al. have developed an electroless deposition method for crystalline particulate ZnO films through the reduction of nitrate ions with dimethylamine borane (DMAB) [Izaki97]. The authors have chemically prepared transparent ZnO films from aqueous solutions, and found a characteristic band gap energy of 3.3 eV [Izaki97]. In a very simple way, the glass substrate has been sensitized with an acidic solution of $SnCl_2$ and then activated with an acidic solution of $PdCl_2$ by using a conventional two-step process [Schlesinger00]. Subsequently, ZnO films have been prepared by immersing the substrate in an aqueous solution containing 0.05 M zinc nitrate and 0.001 to 0.15 M DMAB kept at 50 ^{0}C [Izaki97]. In the same way, Saito and co-workers have demonstrated the fabrication of ZnO micropatterns with selective electroless deposition of ZnO on a silicon oxide surface [Saito02]. Furthermore, spatially resolved cathodoluminescence (CL) images from these structures have been shown. In this part of the thesis, the deposition of zinc oxide on the outer surface of TMV particles together with its mechanism is described. In addition, chemical analysis (by energy filtering TEM on the nanoscale) and optical properties of the zinc oxide rods are presented.

5.2 Experimental Part

Synthesis of Zinc Oxide Rods. In order to coat the TMV particles with ZnO, Pd(II)-incubated TMV suspension is contacted with an electroless deposition (ELD) bath consisting of 0.013 M $Zn(NO_3)^.6H_2O$ (Fluka Chemie 99%) and 0.05 M DMAB [Izaki97]. The ELD bath was used as it is without adjusting the pH. Nevertheless, the ELD bath was filtered since a small amount of white precipitate was observed after addition of DMAB to $Zn(NO_3)$ aqueous solution (see chapter 4.2 for further details about TMV isolation, substrate preparation, sample preparation, activation of TMV (synthesis of nanowires)).

Determination of NO_2^- in ZnO deposition. In order to understand the mechanism of the ZnO deposition, which is not completely understood in the literature [Izaki97], standard nitrate tests

were used. Nitrate level in aqueous samples can be measured by first reducing the nitrate species to nitrite via a redox reaction with a zinc powder [Mackay96]. For the standard samples, 500 µl 10 mM sulfanilic acid (Fluka) and zinc powder were added to 500 µl 3.2 mM $Zn(NO_3)_2$. The sulfanilic acid solution was acidified with 1 M HCl (Suprapur, Merck) to a pH value of around 1. Adding 2 ml of water further diluted the sample. After 30 min, a 1 ml of 10 mM 1-naphtylamine (Fluka) was additionally introduced. The produced nitrite reacts with sulfanilic acid to form a diazonium salt, which reacts with 1-naphtylamine to form a colored compound. The final concentration of nitrite converted to the dye compound is 0.8 mM. In the same way, a similar procedure was applied to detect the amount of nitrite during deposition of ZnO on the outer surface of TMV particles. 30 min after the initiation of the ZnO deposition on TMV particles, a 500 µl of the deposition solution was mixed with a 500 µl 10 mM sulfanilic acid solution (in acidic solution with a pH of around 1) without adding zinc powder. Afterwards, 1 ml of 10 mM 1-naphtylamine was added to form a colored compound in the presence of nitrite. The sample was diluted with 3 ml water to a final volume of 4 ml. Similarly; another sample was prepared, 12 hours after the start of ZnO deposition to the TMV particles. UV-Vis spectra were recorded for each sample.

Cathodoluminescence measurements. The ZnO rods were adsorbed on a TEM grid for cathodoluminescence (CL) measurements at 10-20 K. A scanning electron microscope (SEM) with a heated field emitter (FE-SEM) was used for all the CL measurements. The advantages of a field emitter are the high spatial resolution and the relatively high current density. A high current density is needed in order to excite a large number of electron hole pairs inside the semiconducting sample, which in turn yield the CL intensity. For coupling out the CL-intensity, a glass fiber was used. The fiber can be positioned in a distance of 50-100 µm from the incident point of the electron beam. High collection efficiency comparable to conventional mirror optics (fixed configuration) is achieved. The small working distance is necessary to depict small structures in order to obtain good quality pictures. The glass fiber guides the CL signal to the detection system. The detection system consists of a monochromator with a focal length of 900 mm and a liquid nitrogen cooled CCD

camera. A spectral resolution of approximately 0.1 meV can be achieved. The excitation volume, i.e. the region that is excited by the primary electrons in the SEM, strongly depends on the acceleration voltage of these electrons. At 3 kV, the spatial resolution of the microscope is around 100 nm.

Instrumentation. Most of the transmission electron microscopy (TEM) imaging experiments were performed on a Philips CM 200 operated at 200 kV. Atomic force microscope (AFM) images were obtained with a Thermomicroscopes Autoprobe M5, operated in non-contact and intermittent contact mode, with MikroMasch NSC11 cantilevers or NCHR Pointprobe Nanosensors. UV-Vis spectra were obtained with a UV-Vis Spectrometer Lambda 2 (Perkin Elmer). Elemental mapping experiments were performed on a LIBRA 200 FE energy-filtering microscopes (from Carl Zeiss NTS) (see chapter 4 for the details).

Elemental mapping. See chapter 4 and chapter 3 for the details about the description of an elemental mapping by an energy-filtering transmission electron microscope (EFTEM). According to the edge energies in electron energy-loss (EEL) spectrum (see Table 5.1), elemental maps were obtained.

Element	Pre-edge energy1 (eV)	Pre-edge energy2 (eV)	Post-edge energy (eV)	Edge energy (eV)	Slit width energy (eV)
Zn	940	990	1110	1100	50
O	477	512	552	532	30

Table 5.1 Pre-edge, edge and post-edge energies of the elements used for elemental mapping with the three-window technique (see chapter 3 for the details).

5.3 Deposition of Zinc Oxide

An electroless deposition of ZnO films through the reduction of nitrate ions using dimethylamine borane (DMAB) as a reducing agent has been reported [Izaki97]. In the same way, ZnO was deposited from a similar ELD bath to TMV particles. Initially, comparatively high concentration of zinc nitrate (0.05 M) was used, but due to the high deposition rate we could not detect any TMV

particles in the TEM observations. Probably, all the TMV particles were embedded in large ZnO agglomerates. Subsequently, the concentrations of DMAB and zinc nitrate were decreased in order to optimize the deposition rate of ZnO. Finally, a zinc bath containing 0.013 M zinc nitrate and 0.05 M DMAB was found to be suitable for the deposition of ZnO on the outer surface of TMV particles. It is obvious that the concentration decrease of one of the chemicals is enough to decrease the growth rate of ZnO deposition [Schlesinger00]. After addition of DMAB to the zinc nitrate solution, a white precipitate was observed. This might be due to the pH change of the zinc nitrate solution upon addition of DMAB and therefore ZnO was formed. However, this precipitate is not catalytically active since no further increase in the amount of the precipitate was observed. Before contacting the bath with the catalytically activated virus suspension, the bath was filtered using a filter paper. From these observations, it can be concluded that ZnO is not catalytically active for the deposition of ZnO and thus a catalyst is required for the ELD of ZnO. In order to deposit ZnO on TMV, TMV particles were incubated in an aqueous solution of Pd (II) in order to activate TMV particles for the ELD of ZnO. After contacting the Pd (II) activated TMV suspension with the zinc bath, white precipitate of ZnO was immediately observed (see experimental part for the details). After 30 min., a drop of TMV suspension was brought on a TEM grid for TEM characterization.
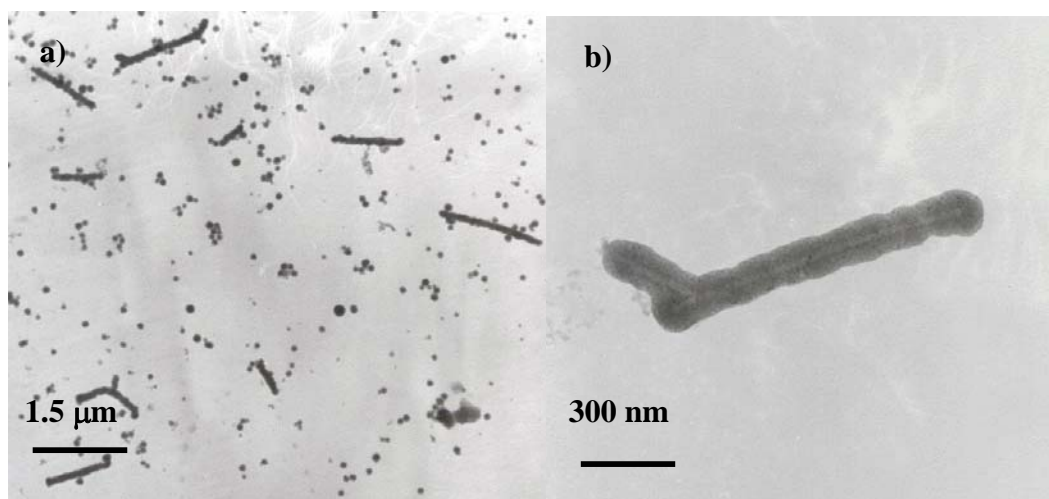
Figure 5.1: TEM micrograph of ZnO deposited on the outer surface of TMV particles. **(a)** Large area imaging. The diameter of the ZnO rods is in between 100-150 nm and the length of the

structures reach a few micrometers depending on the end-to-end assembled virions. **(b)** Imaging of a single ZnO rod. TMV particles can be observed in the center of the ZnO rod.

With the aforementioned ZnO deposition bath, we achieved coating of TMV particles with ZnO. Figure 5.1 shows a TEM micrograph of ZnO coated virions adsorbed on a TEM grid. The diameters of the ZnO rods are in between 100-150 nm and the length of the structures reach a few micrometers depending on the length of end-to-end assembled virions [Nedoluzhko01,Butler99]. Because of the formation of ordered linear aggregates of TMV particles in the presence of divalent metal ions, the length of the ZnO rods is larger than a single TMV particle (300 nm) [Nedoluzhko01]. TMV particles within ZnO rods can be discernible in the Figure 5.1. The rods are not completely smooth but in granular shape (~100 nm in grain size).

Experiments were also carried out to selectively deposit ZnO within the virus central channel. Initial experiments showed ~3 nm diameter ZnO rods within the central channel of the virions but the result was not reproducible. Removing the phosphate buffer in the TMV suspension after dialyzing against water did not change the deposition behavior of ZnO. Note that in the case of Ni, Co, Cu, and CoFe metallizations, dialyzing the TMV suspension against water before metallization resulted in deposition of metals within the virions. This tendency of ZnO not to deposit in the channel is attributed to its strong complex formation with the functional groups present on the external surface of the virus [Mackay96]. For example, the functional groups of carboxyl, amine, and hydroxyl could facilitate the process and the deposited ZnO adheres very strongly on the outer surface. It is also likely that ZnO reacts with the end groups (carboxyl and amine groups) of the coat protein subunits present on the external surface of the TMV and forms complexes with them.

TMV particles were also activated with an aqueous solution of Pt(II) and then treated with the ZnO ELD bath. However, on the outer surface of the TMV particles there was no ZnO coating but ZnO agglomerates were observed in the reaction solution (white precipitate observable in the deposition solution). At this point it is not clear why ZnO does not grow on the outer surface of the TMV after

activating with the Pt(II) aqueous solution. Nevertheless Pd(II) activated TMV can be coated with the ZnO.

In order to deposit ZnO onto the outer surface of the TMV particles, palladium has to form complexes with functional groups of the amino acids on the outer surface of the virion (see Scheme 4.1). Prior to the deposition of ZnO, the Pd(II) species have to be reduced by the reductant (dimethylamine borane, DMAB, present in the solution) since only Pd^0 can act as a catalyst for ELD, but not Pd(II) [Kind98].

The mechanism of the ELD of ZnO has not been clarified. However, nitrate is required to deposit ZnO [Izaki97]. DMAB acts as a reducing agent for the reduction of nitrate ions. Note that DMAB is not able to reduce Zn(II) to its metallic state. The deposition reactions can be described by the following schemes

$$NO_3^- + H_2O + 2e^- \rightarrow NO_2^- + 2\ OH^- \tag{5.1}$$

$$NO_2^- + H_2O + e^- \rightarrow NO + 2\ OH^- \tag{5.2}$$

$$NO_3^- + 2\ H_2O + 3e^- \rightarrow NO + 4\ OH^- \tag{5.3}$$

$$4\ (CH_3)_2NHBH_3 + 12\ NO_3^- \rightarrow HB_4O_7^- + 4\ (CH_3)_2NH_2^+ + 2\ H_2O + 12\ NO_2^- + 3\ OH^- \tag{5.4}$$

$$4\ (CH_3)_2NHBH_3 + 8\ NO_3^- + 2\ H_2O \rightarrow HB_4O_7^- + 4\ (CH_3)_2NH_2^+ + 8\ NO + 11\ OH^- \tag{5.5}$$
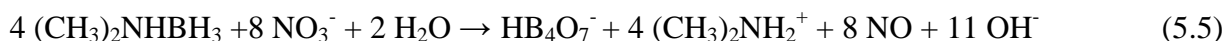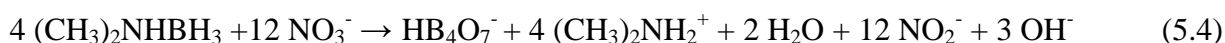
Oxidation of DMAB is described in chapter 4.3 (equation (4.3)). The mechanism of nitrate reduction on different catalytic surfaces has been clarified and suggested that the rate-determining step in the nitrate reduction occurs during its conversion to nitrite [Dima03]. The nitrate ion firstly adsorbs onto the catalytic surface before it is reduced to nitrite by generating hydroxyl groups (5.1) [Dima03]. The reduced palladium can catalyze the reduction of nitrate [Dima03]. The state of the nitrite ion is not completely clear, however, it is known that nitrite is very reactive on transition-metal surfaces and produces chemisorbed NO [Rodes95]. Therefore, it is assumed that reaction 5.1 is quickly followed by reaction 5.2 [Dima03]. Since no formation of N_2 or N_2O on a variety of

metal surfaces has been detected, it has been concluded that the further reduction of NO leads to either NH_3 or NH_2OH [Dima03].
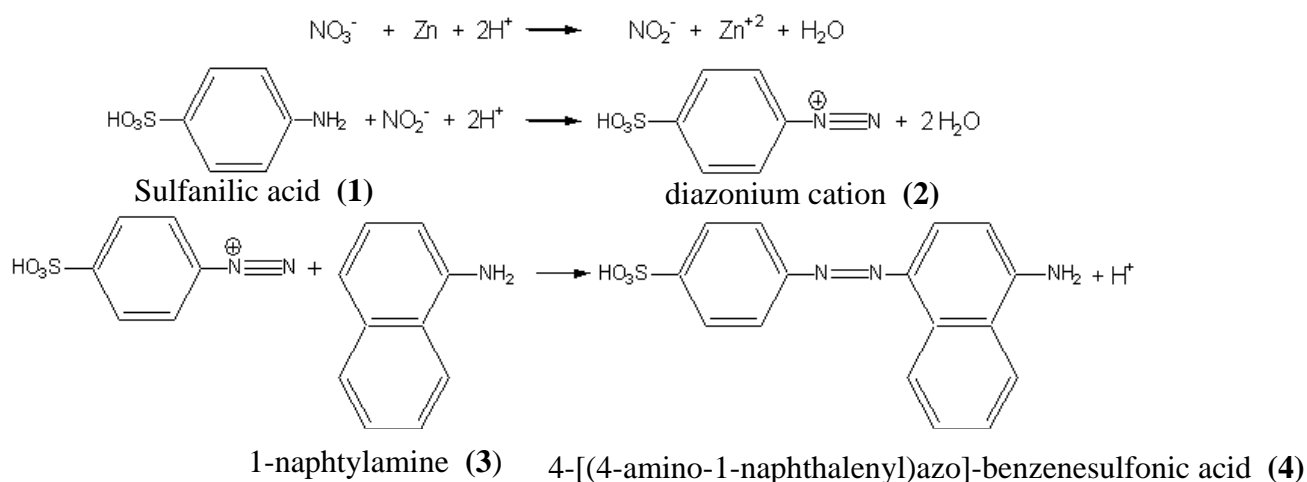

Figure 5.2: Schematic overview of the nitrate detection test. Zinc reduces nitrate to nitrite. The reduced nitrite reacts with sulfanilic acid to generate a diazonium cation. Electrophilic addition of the diazonium cation to 1-naphtylamine results in a formation of (**4**). Electronic spectra of (**4**) give directly the amount of nitrate present in the reaction medium (1/1).

In order to confirm the presence of nitrite during the reduction of nitrate, a standard nitrate test was used (Figure 5.2). In the standard experiment, the nitrate-containing solution with a known concentration was treated with a metallic zinc to reduce nitrate to nitrite in acidic conditions. After 30 min., the generated nitrite was further treated with (**1**) to produce (**2**). Addition of (**2**) to (**3**) generates (**4**) which has an absorption maximum at ~520 nm wavelength (Figure 5.3a). According to the Lambert-Beer law, the concentration of (**4**) is proportional to the absorbance of the compound (**4**) and therefore with the nitrate (or nitrite) concentration in the original solution [Fritz74]. After 30 min of ZnO deposition on the outer surface of TMV particles, a similar experiment was performed. However, there is no increase in the absorbance of (**4**) after 30 min from the initiation of the ZnO deposition (White ZnO precipitate was observed). Thus, there is no nitrite present in the deposition solution. After 12 hours from the initiation of the ZnO deposition reaction, a similar experiment

was carried out. An increase in the absorbance of **(4)** suggests that at the later stage of the ZnO deposition, nitrite was present in the deposition solution (Figure 5.3). At the later stage of the ZnO deposition, the catalyst surfaces might be covered with ZnO; hence the conversion of NO_2^- to NO could be minimized. Therefore the concentration of the nitrite is increased [Rodes95].

After combining the DMAB oxidation reaction in chapter 4.3 (reaction (4.3)) with two possible nitrate reduction reactions (reactions 5.1 and 5.3), two overall reactions can be obtained (reactions 5.4 and 5.5). It is clear that at the beginning of ZnO deposition there is not any nitrite present in the reaction medium. Therefore, reaction (5.5) is the preferred route. This also correlates with the experimental observations mentioned in the literature [Rodes95,Dima03]. Nonetheless, Izaki and co-workers suggested that the final product of nitrate reduction in the ELD deposition of ZnO from zinc nitrate solution is nitrite. At the beginning of the ZnO deposition reaction this is not feasible. However, in the later stage of the experiments nitrite is the dominant end product. Hence, reaction (5.4) is becoming more dominant than reaction (5.5) in the later stage of the ZnO deposition.
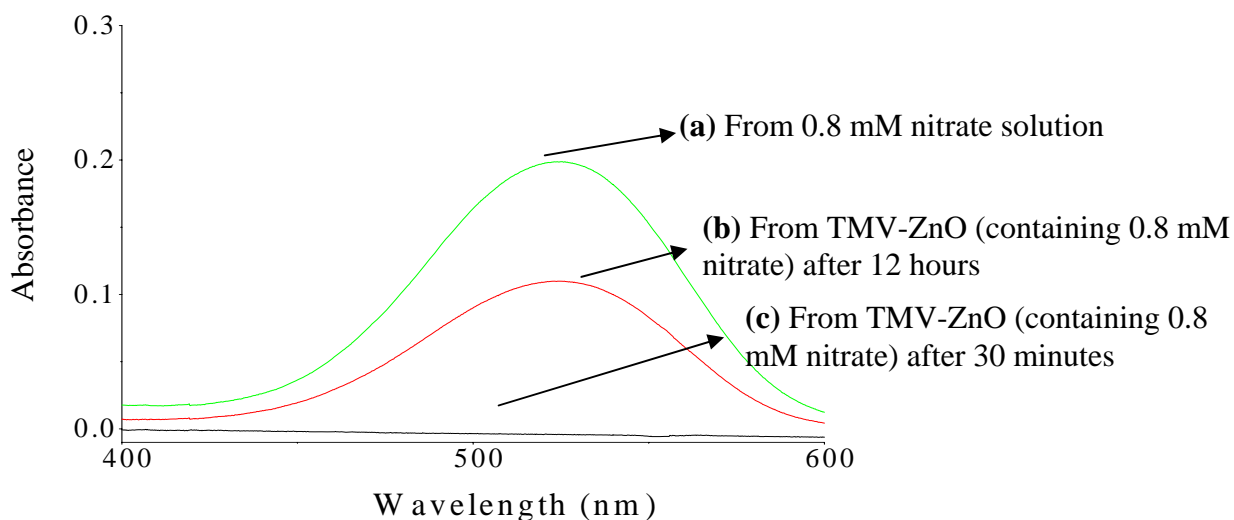
Figure 5.3: UV-Vis spectra of **(4)** from ZnO deposition solution **(a)** from standard (0.8 mM) nitrate solution **(b)** from TMV-ZnO solution containing 0.8 mM nitrate after 30 min. from the initiation of the reaction **(c)** from TMV-ZnO solution containing 0.8 mM nitrate after 12 hours from the initiation of the reaction.

The ELD of ZnO on palladium activated glass surfaces indicated that the pH of the solution increased during the process. This is also evident from reactions (5.4) and (5.5), in which hydroxyl groups are generated after the reduction of nitrate. The generated hydroxyl groups react further with the Zn(II) ions present in the solution (Zn (II) can not be reduced to its metallic state by DMAB) and thus resulting in ZnO formation, see reactions (5.6) and (5.7).

$$Zn^{2+} + 2OH^- \rightarrow Zn(OH)_2 \tag{5.6}$$

$$Zn(OH)_2 \rightarrow ZnO + H_2O \tag{5.7}$$

It has been revealed that the surface of the as-deposited ZnO quantum dots is passivated by a thin layer of $Zn(OH)_2$, thus, the ZnO quantum dots consist of a $ZnO/Zn(OH)_2$ core-shell structures [Zhou02]. In order to convert all $Zn(OH)_2$ to ZnO, annealing treatment has to be performed.
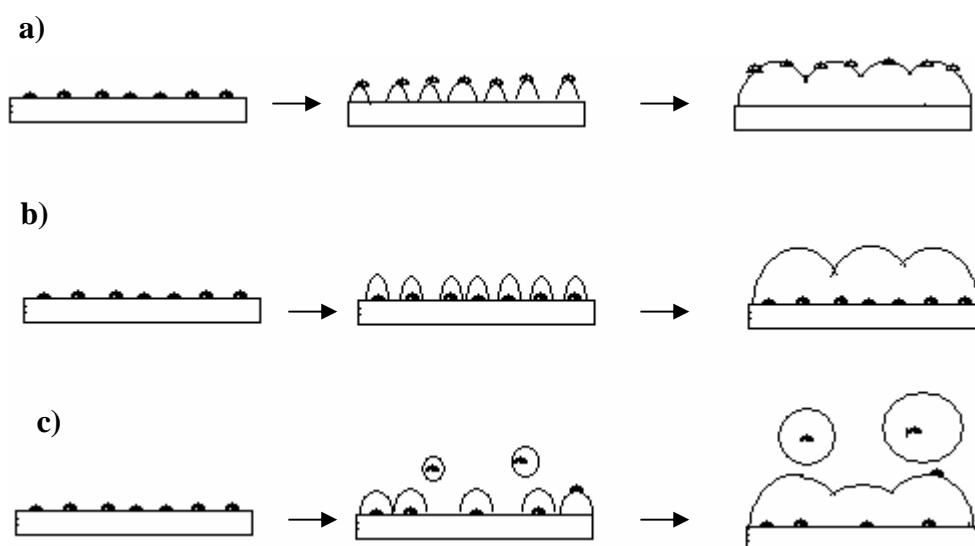
Scheme 5.1: Mechanism for the ELD of ZnO on the outer surface of TMV particles. **(a)** Palladium clusters (larger than 1 nm) are adsorbed on TMV outer surface [Knez04b]. These clusters remain at the surface of the growing ZnO layer. **(b)** Palladium clusters remain on the outer surface of the virus during ZnO growth. **(c)** Some of the palladium clusters remain on the outer surface of the virus while a few of them detach from the surface and stay in the deposition solution. In addition, a few of them bind to the growing ZnO layer like in (a).

Understanding the mechanism of the ELD of ZnO is very important, in the future, to synthesize ~3 nm diameter ZnO nanowires inside the virus. Based on the experimental observations during the ELD of ZnO, three different ZnO deposition mechanisms are proposed (Scheme 5.1). In Scheme 5.1a, catalyst particles are assumed to be present on the growing ZnO layer since ZnO is not catalytically active. Therefore, ZnO is continuously supplied to the growing layer. A similar mechanism has been proposed for gold nanoparticle catalyzed ZnO nanorod fabrication using vapor transport and condensation process [Huang01]. Another possibility is illustrated in Scheme 5.1b, in which catalyst particles are buried within the ZnO layer and attached to the virus surface. Indeed, this has been proven by Saito and coworkers investigations, in which they have found palladium clusters below the grown ZnO layer on a palladium activated SiO_2 surface [Saito02]. However, only the interface between the ZnO and the SiO_2 surface has been shown. Furthermore, previously, on the outer surface of the TMV particles, palladium particles of sizes larger than one nanometer (up to 8 nm) were observed after the reduction of Pd(II) [Knez04b]. The final mechanism (Scheme 5.1c) proposed here is the combination of mechanisms in Scheme 5.1a and 5.1b. Since ZnO does not show catalytic properties. In any case reducing agent together with the nitrate ions must be in contact with the catalytic surface. As it has been discussed above, it is known that nitrite is very reactive on transition-metal surfaces and produces chemisorbed NO [Rodes95]. Therefore, for the reduction of nitrate, a catalytic surface is required. The granularity of the ZnO structure might arise from the inhomogeneous distribution of the catalysts particles on the surface or varying the rate of ELD of ZnO on each catalyst particle whose size also affects the process.
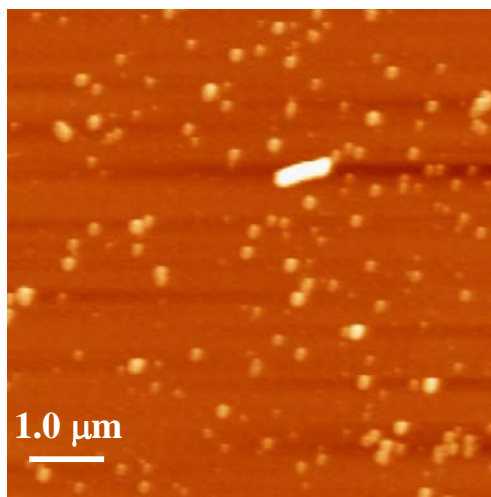
Figure 5.4: AFM image (non-contact, topography) of a ZnO rod on an oxidized silicon surface. The wire is approximately 700 nm (templated by two TMV particles) in length and ~150 nm wide.

ZnO rods were also adsorbed on SiO_2 surfaces. Figure 5.4 shows an AFM image of ~700 nm in length and ~150 nm wide ZnO rod adsorbed on a SiO_2 surface. The white features in the figure come from uncontrolled deposition of ZnO during adsorption of ZnO rods from the reaction solution.

5.4 Elemental Mapping of ZnO Rods

In the previous section, electroless deposition of materials on the outer surface of the TMV particles from an ELD bath containing zinc nitrate and a borane compound (DMAB) is discussed in detail. Here the chemical composition of the deposited material, investigated by EFTEM, is described. Figure 5.5 illustrates EEL spectra of the material deposited on the outer surface of TMV particles from the Zn(II) containing ELD bath. The carbon peak arises from TMV particles, and in part also from the TEM grid. However, the oxygen signal comes only from the nanowire since the pristine TMV particles do not show any oxygen signals in the elemental map (see also chapter 4). The broad zinc peak in Figure 5.5b arises from the deposited material on the outer surface of the TMV particles. Therefore, the deposited material consists of Zn and O with an elemental composition of 70:30. The deviation from the expected value of 50:50 originates mainly from the broad Zn peak in

the electron energy loss spectrum (Figure 5.5b); recording and integration of the peak cause an error of up to 50%, although <~20% was expected. EFTEM can now be used to give local elemental information: Figure 5.6a shows a TEM image of a rod synthesized from the Zn(II) containing ELD bath. The rod has a length of 900 nm and a diameter of 120 nm, likely containing three TMV particles in end-to-end assembly. The particle (~100 nm in length) attached to the upper end of the rod in Figure 5.6a could be the RNA of a partially uncoated TMV coated with the deposited ZnO.
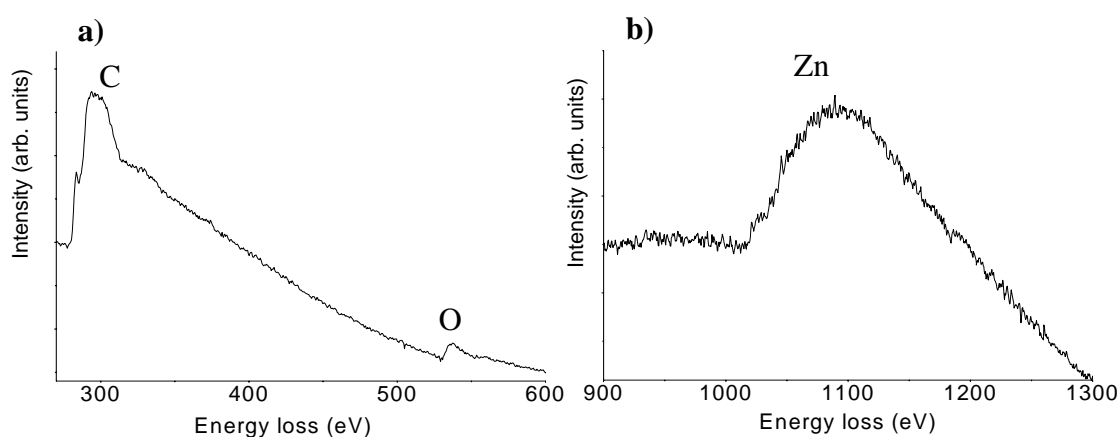
Figure 5.5: EEL spectra of carbon, oxygen, and zinc from the material (on a Cu-TEM grid surface) synthesized by ELD from zinc nitrate and dimethylamine borane. **(a)** Carbon K-edge at 284 eV, oxygen K-edge at 532 eV, **(b)** and Zn $L_{2,3}$-edges around 1100 eV.
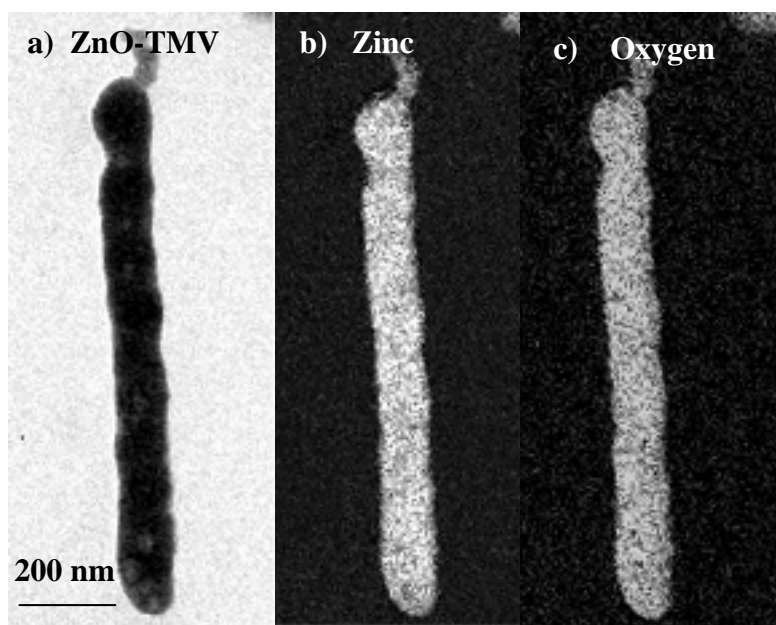
Figure 5.6: Elemental maps of a ZnO rod by EFTEM. **(a)** TEM micrograph of ZnO deposited on the outer surface of TMV particles. The length of the rod corresponds to ~900 nm (three virions). **(b)** Zinc map (Zn $L_{2,3}$ edges at 1020 and 1043 eV), **(c)** oxygen map of the rod (O K-edge at 532 eV).

The zinc and oxygen maps of the ZnO rod were obtained in the usual manner from the Zn $L_{2,3}$ and the O K-edges (see chapter 3 for the details), Figure 5.6. Note that the ZnO rod in Figure 5.8a is not completely smooth, but granular in shape. This is also supported by the O and Zn elemental maps, which reproduce the bright-field TEM image to nearly all details. The granular shape can be interpreted as originating from the variable deposition rates of ZnO at different locations of the virions. In addition, the amount of catalyst (palladium) attached to the outer surface of the virus can affect this process. In other words, although many catalytic nuclei may be present, it appears as if only very few, say 1 or 2 per 50 nm TMV length, are so active that the material growth wins out over all other nuclei. The crystalline structure of the synthesized material was not investigated; however, X-ray diffraction of bulk samples of electrolessly deposited ZnO (very similar conditions, no heating) shows the wurtzite structure [Izaki00]. It is likely that our ZnO grains, which are not true nanoscale deposits, but contain hundreds of atomic planes, has the same structure since bulk properties are expected for such large structures.

5.5 Cathodoluminescence from ZnO Rods

In the previous section, elemental analysis of the materials deposited on the outer surface of the TMV particles from the bath containing $Zn(NO_3)_2$ and DMAB indicated that the deposited material consists of Zn and O. In this part of the work, cathodoluminescence (CL) measurements from the ZnO rods on a carbon coated Cu-TEM grid are described. Electroless deposition of ZnO, based on the reduction of nitrate in the deposition solution, was explained in the experimental part. Figure 5.7a shows a scanning electron microscope (SEM) micrograph of ZnO mineralized TMV particles adsorbed on a TEM grid. In addition, micrometer scale ZnO agglomerates can be found on the substrate surface.
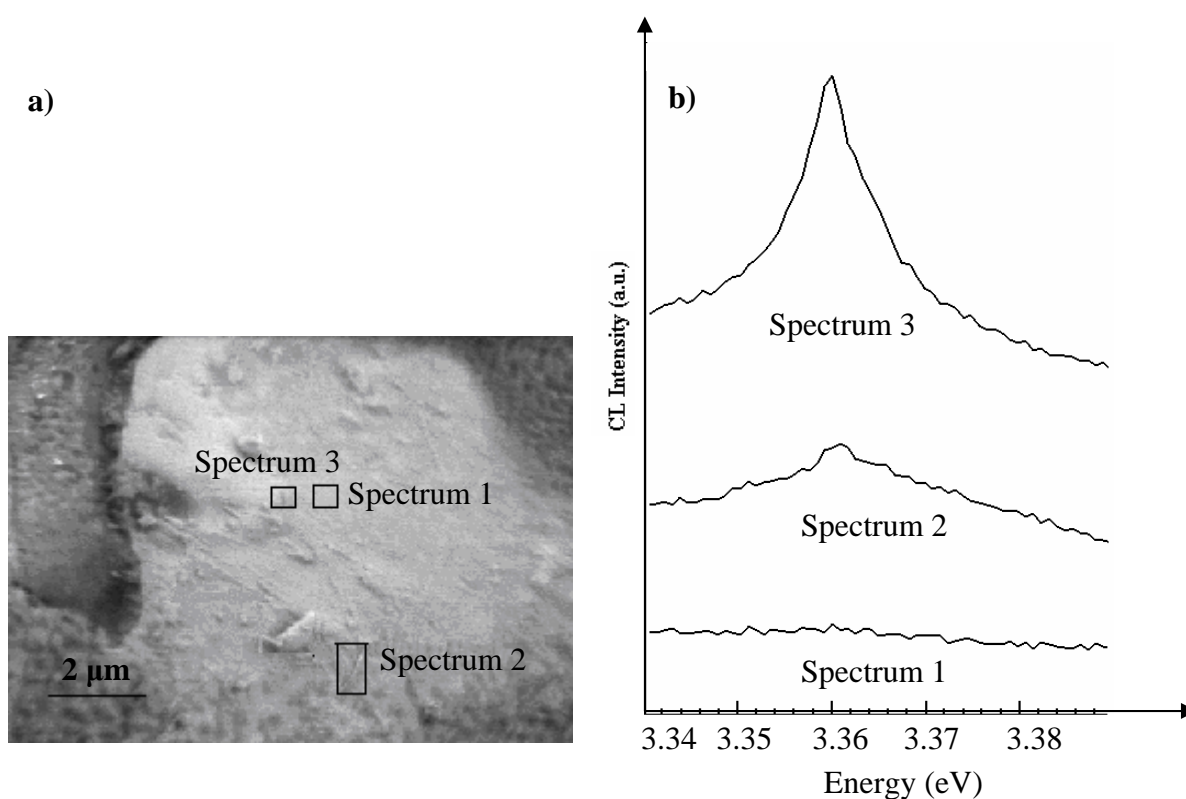
Figure 5.7: A SEM micrograph and cathodoluminescence (CL) spectra at 10-20 K obtained from ZnO on the outer surface of TMV particles. **(a)** A SEM micrograph of ZnO deposited TMV particles adsorbed on a TEM grid. Rectangular shaped boxes indicate regions where CL measurements were performed. **(b)** CL spectra obtained from the indicated regions in (a).

CL spectra from the different regions of the substrate are shown in Figure 5.7b. In order to measure the CL properties of the substrate (carbon-coated Cu-TEM grid), *spectrum 1* was directly taken from the region in which there was not any deposited material hence no CL intensity was observed from this measurement. This is a background spectrum also for other measurements. In the case of *spectrum 2*, the CL measurement was directly taken from a micrometer long nanowire, which presumably represents three virions coated with ZnO. An emission around 3.36 eV indicates the presence of large band gap semiconductor, which is attributed to ZnO. In the same way, CL measurements from the box shaped region in Figure 5.7a (*spectrum 3*) demonstrates very strong emission around 3.36 eV. In this region, ~300 nm long ZnO rod can be attributed to a single virion coated with ZnO. In a similar way, CL measurement from large agglomerate of a material on the surface (box shaped region without any label) in Figure 5.7a gave a very large CL intensity at around 3.36 eV. The band gap of the semiconductor on the TEM grid is around 3.36, which can be attributed to ZnO. Therefore, the deposited material on the outer surface of the virions shows ultraviolet emission approximately at 10-20 K.

The first report about the electroless deposition of zincoxide was published by Izaki and co-workers and in this report they reported the electroless deposition, crystalline structure analysis, and optical band gap of the deposited zincoxide [Izaki97]. However, the deposition mechanism of the zincoxide has not been explained in detail. They found that electrolessly deposited ZnO showed wurtzite structure, and an optical band gap energy of about 3.3 eV which correlates with our CL measurements. All of these CL measurements of ZnO are consistent with the values from the literature in which 3.3 eV is attributed to the band gap of the bulk ZnO [Srikant98]. Therefore, the deposited material on the outer surface of TMV particles with a $Zn(NO_3)_2$ and DMAB containing bath shows CL at 3.36 eV indicating that the deposited material is zinc oxide. Recently, ZnO was selectively deposited on a catalytically activated (by palladium catalyst) region of SiO_2 surfaces by using the electroless deposition method. The selectively patterned regions on the SiO_2 surface showed the CL at room temperature [Saito02]. Palladium catalysts activated the SiO_2 surface (as in

the case of s*pectrum 1* which does not have any ZnO) did not show any CL, confirming that the emission was solely due to the ZnO deposited on the SiO_2 surface [Saito02].

5.6 Conclusions

From the presented experimental results, the following conclusions can be drawn:

(a) ZnO was deposited on the outer surface of TMV particles. Spectrophotometric analysis of the ZnO deposition mechanism indicated that nitrite (in the literature, it is assumed to be present) is not present at the beginning of the deposition reaction (30 min.). Hence nitrate, which is an important species in the deposition of ZnO, must be further reduced to other species like NO. Three possible ZnO growth mechanisms on the outer surface of the virus have been discussed in the light of the experimental observations. In contrast to the other mineralization reactions (Cu, Ni, Co, CoFe), the product ZnO can bind to functional groups on the external surface of the virus, based on complex formation with Zn(II). As a result, ZnO adheres very strongly.

(b) Further experiments showed that the material deposited on the outer surface of the TMV particles from the Zn(II) / dimethylamine borane bath includes zinc and oxygen. Both zinc and oxygen elemental maps obtained by using the EFTEM reproduce the bright-field TEM images. Thus, TMV particles are mineralized with ZnO.

(c) CL measurements show that the deposited material on the outer surface of the virions show ultraviolet emission with a photon energy of around 3.36 eV, which is equal to the band gap of the bulk ZnO. Measurements from the regions without ZnO did not show any luminescence.

CHAPTER 6

Printing and Aligning TMV Particles on Surfaces

In this chapter printing and alignment of TMV particles on various surfaces are described. Firstly, microcontact printing (μCP) of a complete virus particle, TMV, has been achieved. Careful control of printing conditions and Atomic force microscopy (AFM) analysis have revealed selectively adsorbed end-to-end assembled TMV rods at the edges of the recessed regions of the stamp pattern (microstructure). Dewetting of the ink solvent (water) on the stamp surface is the driving force for this process. The assembled TMV rods have been successfully transferred from the stamp surface to the oxidized silicon surfaces. Therefore, easily produced microstructures are the basis for a very simple process for nanometer scale patterns. Secondly, simple directional mechanical forces, applied by very simple techniques, can align TMV rods in suspensions. Such alignment procedures are well known for > 1 μm long molecules such as DNA and nanowires; however, they also work for molecules as short as the 300 nm long TMV, and they can be combined with adsorption. Finally, virus particles have been shown to adsorb with high selectivity on sub-μm amine-fuctionalized patterns.

6.1 Introduction

Patterning and immobilizing biologically active moieties with micrometer and nanometer scale control have attracted intense interest due to their great potential in basic research, construction of electronic and photonic circuits, diagnostics, and drug discovery. A very simple and effective approach for mesoscopic structuring of surfaces with molecules is microcontact printing (µCP) [Xia98,Cavallini03,Cherniavskaya02] (see also chapter 3 for details). µCP can create patterned self-assembled monolayers on the surfaces of materials of interest such as gold, silicon oxide, using an elastomeric stamp whose surface has itself been patterned in an appropriate relief structure. One can then employ the chemical difference between printed and bare substrate, e.g. for the spatially selective adsorption of biomolecules [Xia98,Bernard00]. More attractive and even simpler is the direct transfer (direct printing) of the biomolecules in a desired pattern, as recently shown for dendrimers, proteins, and also for DNA [Bernard00,Nakao03,Wu02]. For example, Bernard et al. have succeeded in direct printing of 16 different proteins onto polystyrene [Bernard00]. They inked a stamp by means of a microfluidic network in the submicrometer range, and showed that the biological activity of the printed proteins was preserved. A simple method has also been developed for reproducibly creating highly aligned DNA nanowires on various substrates by aligning DNA nanowires on a stamp surface and then directly printing them on various surfaces [Nakao03]. Currently, the smallest features that have been generated using µCP were parallel lines of methyl-terminated SAMs that were ~35 nm in width, separated by ~350 nm [Biebuyck97]. It should be mentioned that a closely related alternative to µCP is nanoimprinting [Chou97]: A mold (made of SiO_2) is pressed into a thin polymethylmetacrylate (PMMA) polymer film that is heated above its glass transition temperature. Hence the polymer behaves as a viscous liquid and can flow under pressure, thereby adhering to the mold. This allows fabrication of arrays of holes in PMMA with diameters of ~10 nm [Chou97].

An important question is up to which sizes large molecules or supramolecular assemblies can be printed without loss of functionality and structural integrity. While for small molecules (e.g. alkanethiols) a molecule-covered scanning probe tip (dip pen nanolithography (DPN)) can be used for selective placement of molecules on a substrate [Piner99], this is difficult with TMVs or other very large supramolecular structures (i. e. with molecules larger than proteins or antibodies), since the required dissolution into and diffusion in the water meniscus between the tip and the sample is too slow. Indirect methods can overcome this limitation: Recently, TMV nanoarrays at the single-particle level have been fabricated by initially generating very small sized (in submicrometer square) templates of 16-mercaptohexadecanoic acid on a gold thin film by DPN, followed by selective adsorption of TMV particles on this template [Vega05]. However, the use of thiol as an ink in this case restricts the choice of the substrate to gold only.

We show that very large supramolecular units of TMV particles (300 nm in length and 18 nm in diameter) having more than 2000 protein subunits can be printed and aligned by simple and elegant direct transfer methods. However, an exact placement in a defined orientation is not straightforward: The printing process, while scalable down to 30 nm, would require extraordinary care concerning stamp chemistry, concentration of TMV suspension, inking solvent, and also drying conditions. The alternative is the assembly at the edges, printing the units with much higher accuracy (~30 nm) than the smallest feature size of the stamp.

An alternative way of organizing nanomaterials is the use of directional mechanical forces. In this case, a droplet with suspended or dissolved nanomaterial is deposited on the substrate of interest and removed by applying an external force [Nakao03]. Surface tension at the air-solvent interface plays an important role in generating parallel arrays of the nanomaterial. For example, Nakao and coworkers have deposited droplets containing DNA molecules on PDMS sheets, and removed them with a pipet [Nakao03]. When a droplet is sucked into the pipet, the surface tension at the moving air-water interface can stretch the molecules along the sucking direction [Nakao03]. Directional mechanical forces can generate parallel assemblies of nanowires, nanotubes, and biomolecules

during their adsorption on various surfaces [Deng03,Nakao03,Huang01]. Such assemblies would be especially useful for fabricating nanosized building blocks into functional networks [Huang01]. This type of parallel assembly of molecules is well known for DNA [Deng03] and nanowires [Huang01], however, this is not well known for much shorter supramolecular units (submicrometer range) like TMV. In the same way, TMV particles can be assembled parallelly on various surfaces. For such an experiment, a droplet of TMV suspension is removed with a filter paper; we show that the virions oriented in the direction of the solvent flow.

Finally, selective assembly of the virus particles on a 3-aminopropyltriethoxysilane (APTES) template is described. It is well known that APTES molecules react with the silicon oxide surface thereby producing an amine-terminated monolayer [Nakanishi05]. On such surfaces, TMV particles adsorb very strongly [Knez04a]. The APTES templates on silicon oxide surfaces have been generated by using electron beam lithography (EBL). This type of patterning approach has been termed selective molecular assembly patterning (SMAP) [Michel02,Lussi05]. SMAP is based on a combination of lithographic structuring of surfaces (In our case, silicon oxide surfaces were used.) with the selective self-assembly of organic molecules. In a related study, Vega and coworkers have fabricated TMV nanoarrays by initially generating chemical templates of 16-mercaptohexadecanoic acid on a gold thin film by using DPN [Vega05]. Obviously, such a selective assembly can be advantageous for manipulating virions on the single particle level, and for facilitating electrical contact of virions and mineralized virions.

6.2 Experimental Part

Substrates and stamps. For the µCP procedure, structured PDMS (poly dimethylsiloxane, Sylgard 184, Dow Corning) stamps were formed from a silicon wafer master (Institute for Microelectronics (IMS) Stuttgart), which was rendered hydrophilic with fluoroalkyl-trichlorosilane vapour before

use. We employed oxidized silicon wafers as solid substrates for printing experiments, which were terminated with hydroxyl groups by the so-called "RCA" procedure (see chapter 4 for the details).

Inking, printing and aligning. For the µCP procedure, PDMS stamps were treated for > 2 s with a 1 mbar oxygen plasma (Technics Plasma 100-E, TePla), immersed for 30 min in 0.1-10 mg/ml TMV suspensions (in water or phosphate buffer), dried with an argon stream, and contacted for 10-20 sec with Mg^{2+}-mica surfaces (freshly peeled and pretreated with 100 mM aqueous $MgCl_2$ for 10 min) or oxidized silicon wafers. The Mg^{2+}-mica is better suited than pure mica [Knez04a]. The reason is that the surface of Mg^{2+}-mica has a positive charge while the TMV particles are negatively charged, hence electrostatic interaction or Mg^{2+} salt bridges come into play. In order to align TMV particles on the surface of Formvar/carbon-coated copper grids (300 or 400 mesh, SPI-Supplies), the grids were first dipped into pure ethanol (Roth Rotipuran) and air-dried. 20 µl of 10 mg/ml TMV suspension was placed on the grid for 1 min, after which the droplet was removed by a filter paper touching the grid on one side. For selective adsorption of TMV particles on the surface of amine-terminated areas on silicon/silicon oxide wafers, the wafers were incubated in a 0.2 mg/ml TMV suspension overnight and then washed with water. 3-aminopropyltriethoxysilane (APTES) (Aldrich) was used for terminating an oxygen plasma treated PDMS surface with amine functional groups. For such an experiment, an oxygen plasma treated PDMS was dipped in a 10 mL aqueous solution containing 6 µl APTES for 2 min at room temperature.

Lithographical patterning. Electron beam lithography (EBL) (see also chapter 3 for the details) was based on a Hitachi S2300 scanning electron microscope (SEM) equipped with a motorized stage, a custom-made beam blanker, an external compensation of environmental magnetic fields, and the *Elphy* software. First, electron patterns were written into poly(methylmethacrylate) (PMMA) (MicroChem) layers, which were spin coated on a silicon/silicon oxide wafer substrate. The wafer contains coordinate markers made of gold, so the positions of objects on the chip can be easily found. Two layers of PMMA with different molecular weights were used as resist, so-called

"3.5% 200K" (PMMA-1) for the first layer and "1.5% 950K" (PMMA-2) for the second layer (Scheme 5.1). Before irradiating the PMMA coated wafer with an electron beam, the template patterns were drawn in a software package called *Xfig*. A file containing the coordinates of the templates on the chip was transferred to the SEM used for electron beam irradiation of the wafer. Therefore, the electron beam can only irradiate those regions defined in the software package.
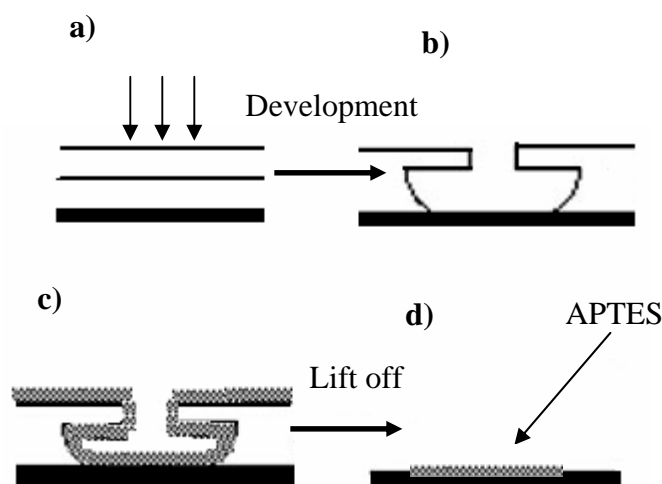
Scheme 5.1: The steps for generating APTES templates on a SiO_2 surface by using electron beam lithography (EBL). **(a)** PMMA layers are spin coated on SiO_2 surface and then exposed to an electron beam. **(b)** The PMMA is developed (giving a slight undercut). **(c)** APTES molecules react with the whole surface. **(d)** PMMA is completely removed from the surface (lift-off) (see also chapter 3 for EBL).

To open up the irradiated regions where the chains of PMMA are decomposed, methylisobutylketone (Merck, VLSI Selectipur) was used as a developer. After this local removal of the PMMA, the defined regions of the openly accessible silicon oxide surface were terminated with amine groups by reaction with 3-aminopropyltriethoxysilane (APTES) (Aldrich). The substrates were dipped in a 10 mL aqueous solution containing 6 µl APTES for 2 min at room temperature. Subsequently, the wafer was rinsed with pure water and blown dry with an argon stream. Finally, 1-methyl-2-pyrrolidone (Merck, VLSI Selectipur) was used as a remover in the lift-

off process (complete removal of all PMMA, leaving blank silicon oxide and the APTES-coated regions). The process does not affect the gold markers.

Instrumentation. Contact angles of pure water droplets were recorded with an OCAH 230 (Dataphysics) model contact angle machine controlled with a software program, which enables the machine to obtain measurements automatically. AFM images were recorded with a Thermomicroscopes M5 Autoprobe operated in non-contact and intermittent contact modes, with MikroMasch NSC11 or NCHR Pointprobe Nanosensors tips. Transmission electron microscopy (TEM) images were obtained in a Philips CM 200 at 200 kV.

6.3 Printing of TMV particles

It is well established that - without oxygen plasma treatment of the PDMS stamps - AFM images of TMV adsorbed on the PDMS show disordered, large-scale (several micrometers) multilayer aggregates of TMV [Knez03]. Dewetting phenomena occur on the strongly hydrophobic stamp surface (water droplet contact angle $\sim108^0$) during drying in air (before contacting the stamp with a solid surface). To bypass this problem, PDMS surfaces can be oxidized with an oxygen plasma, rendering it hydrophilic (contact angle $\sim10^0$). Note that in this part of the work, oxidized PDMS is abbreviated as Ox-PDMS to differentiate from the pristine PDMS. Then the stamp surface was inked with a TMV suspension. In contrast to the hydrophobic stamps, oxidized stamps (hydrophilic) can transfer TMV in well-defined patterns on hydrophilic substrates such as oxidized silicon wafers, as shown in Figure 5.1. The stamp in this case has separated square-and line shaped structures of a few hundred to several µm side lengths. A "positive" stamp was used for Figure 5.1, i.e. the square-shaped area contacted the surface. A "negative" stamp produces similar patterns, in which a grid-shaped area is in contact with the surface. Note that in both cases we observed 100% selectivity, i.e. virions do never cover a non-contacted area. Within the contact areas the virions are randomly distributed and oriented. Multilayers of TMVs can be transferred in some places (see

Figure 5.1a, white spots on the printed pattern). Remarkably, the line pattern in Figure 5.1b, produced by virions randomly adsorbed on the printing stamp, is decorated by virions on its entire width. Note that the same procedure works also on mica surfaces. However, we have to consider that freshly cleaved mica surface has a strong negative charge (one charge per ~0.468 nm^2) [Nishimura95]. Pretreatment with divalent cations (Mg^{2+}) results in fixing positive charges at the negative charges on the surface, thereby decreasing the negative surface charge density [Nishimura95]. Negatively charged TMV particles at neutral pH therefore can bind at the positively charged Mg^{2+}-mica surface through electrostatic interaction or through bridges formed by Mg^{2+} interacting simultaneously with both the negative charges of mica and chemical functional groups of TMV, such as carboxylate groups. The formation of TMV patterns on mica, on oxidized Si, or on Ox-PDMS requires relatively concentrated TMV suspensions, for example 10 mg/ml, when the suspension is contacted ("inking") with the stamp and removed after the inking time, or drying TMV suspensions of relatively low concentrations (0.2 mg/ml) completely on the stamp.
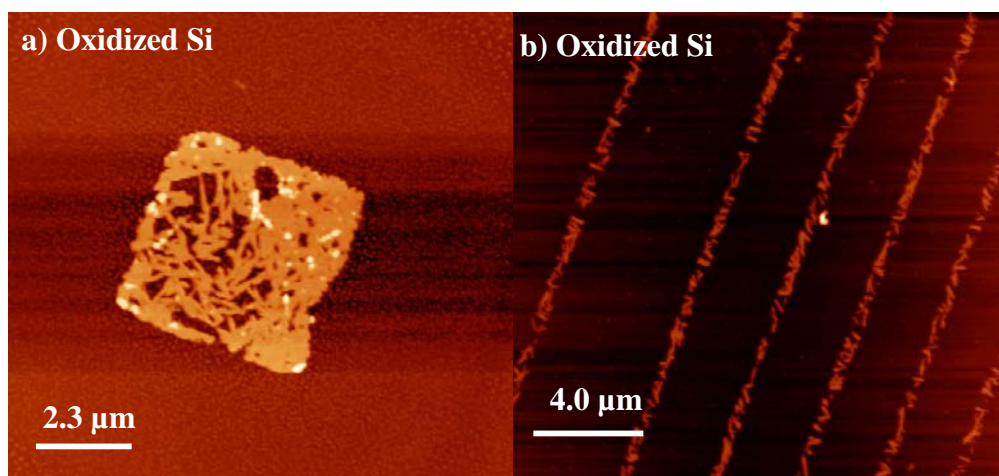
Figure 5.1: Printing of TMV particles. **(a)** AFM image (non-contact, topography) of an oxidized silicon surface, patterned with TMV particles in discrete areas, here a square, with a positive structured stamp. **(b)** AFM image (non-contact, topography) of an oxidized silicon surface, patterned with TMV particles in discrete lines with a positive structured stamp.

Obviously the interaction strength between TMV and the surfaces plays an essential role. Substantial differences between TMV adsorption on hydrophilic and on hydrophobic surfaces were already found by Knez [Knez04a], which can be confirmed by the µCP results presented here. Since the outer surface of the TMV particles contains many functional groups like hydroxyl, amine, amide, and carboxylate, the affinity to hydrophilic surfaces (Ox-PDMS stamps) is higher than the affinity to hydrophobic surfaces (PDMS stamp surface without treatment) because of the hydrogen bond formation between the functional groups on the outer surface of TMV particles and on the surface of the hydrophilic surface. Of course other interactions such as dipole-dipole and van der Waals forces operate as well, but the hydrogen bonds should dominate due to their high binding energy [Cosgrove05]. One should also be aware that TMV can bind to TMV, again with hydrogen bonds (ion-dipole interactions might operate, too), so in analogy to the well-known liquid crystal and fiber formation, and to side-by-side assembly of TMV, one would expect multilayers on Ox-PDMS stamps. We were able to verify this by AFM (see Figure 5.3). At this point it is interesting to note that nearly exclusively monolayer high TMV assemblies are transferred. The reason is that the side-by-side interactions, despite the involvement of strong ion-dipole forces, are limited to the small areas where TMVs overlap. Since they are usually crisscrossing rather than ordering in one direction, the TMV-TMV interactions are altogether rather weak, definitely weaker than the TMV-surface interaction with hydrophilic surfaces. Consequently, TMV particles are transferred in random distribution and orientation. We note that water on the TMV and on the stamp surfaces may be present as thin film and support the transfer, but the high selectivity proves that no meniscus as in DPN translocates the particles. Furthermore, the strong adsorption prevents mobility on the stamp surface, as proven by AFM: virions cannot be moved; even when the stamp surface is indented, TMV particles are dissected without lateral movement, see also Figure 5.2 for the details.
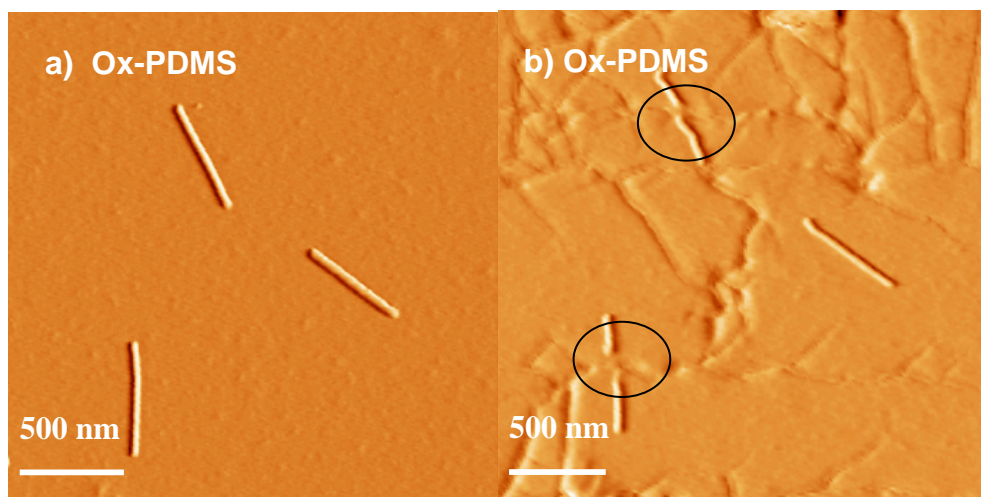
Figure 5.2: AFM images (non-contact mode, error signal) of TMV particles (0.2 mg TMV /ml) adsorbed on Ox-PMDS surface for mobility test. **(a)** End-to-end assembled TMV particles on Ox-PMDS surface (right to left scanning); **(b)** same area; TMV particles after dissecting with the AFM tip (left to right scanning). During non-contact mode AFM scanning on the stamp surface, the set-point was shortly decreased to zero in two places (indicated with the circles). At these locations, the AFM tip dissects the TMV particles without lateral movement of the virions. The cracks on the stamp surface (all other features, light grey) are due to the strong interaction of the AFM tip with the stamp.

The patterns (randomly distributed TMV particles in predefined areas) produced in Figure 5.1 might be valuable for biological applications; such as biosensors, chromatography, cell culturing, DNA microarrays, diagnostic immunoassays [Bernard00]. However, ordered assemblies of virus particles are more desirable in order to expand the scope of application for virus patterns in the fields of nanoelectronics, where TMV particles can be functional units like interconnects or device channels [Huang01].

6.3.1 Adsorption of Virus Particles on Stamps

Adsorption properties of virus particles on Ox-PDMS surfaces are important in order to have a better control of the printing process in µCP. Therefore, we tried to change several experimental

parameters. Note that using filter paper or an argon stream during inking of the stamp removes most of the TMV particles already in the suspension (estimated to be >99%). We applied 0.2 mg/ml TMV suspension to an Ox-PDMS surface. Subsequently, the suspension was dried completely (by waiting more than 30 min.) without using a filter paper or a stream of inert gas. In other words, all TMV rods in the suspension adsorbed on the printing stamp. Hence, the TMV particles were distributed randomly on the Ox-PDMS surface, see Figure 5.3a. Multilayers of them are discernible on the printing stamp surface. The inset shows a zoomed-in region with individual TMV particles.
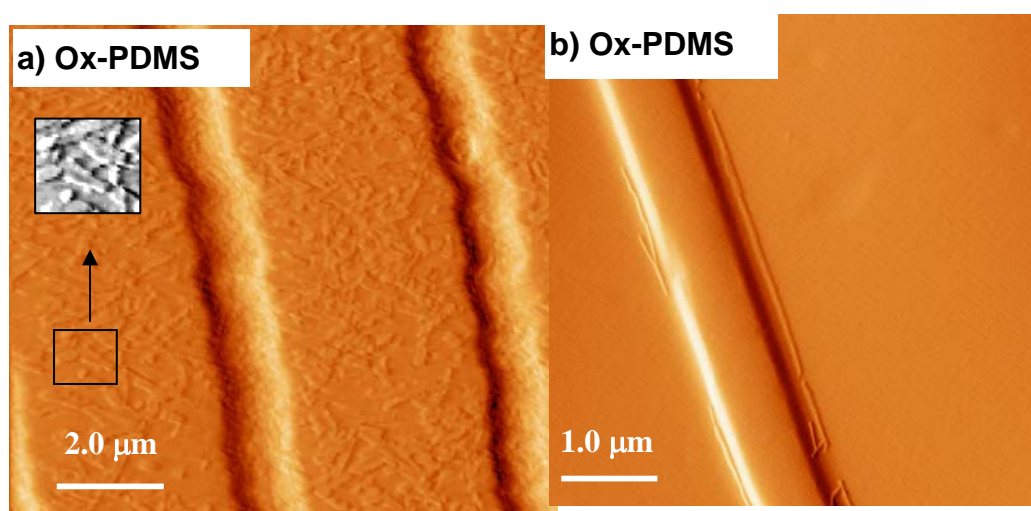
Figure 5.3: AFM images (non-contact mode, error signal) of TMV particles adsorbed on Ox-PDMS surfaces after an oxygen plasma treatment. The white and black parts (lines) show the steep slopes of the structure on the Ox-PDMS surface, as if appearing illuminated. **(a)** 0.2 mg/ml TMV suspension was dried on the surface, and TMV particles were adsorbed at very high density (randomly distributed over the Ox-PDMS surface) on the negatively structured stamp surface. The stamp structure has approximately 1.5 µm width. The inset shows an enlarged part of the image in which TMV particles can be discerned. **(b)** A 0.2 mg/ml TMV suspension was contacted with the surface, and after 30 min dried with an argon stream. Only few virions, aligning at the edges within the recessed region of the positive stamp structure, adsorb.

In another experiment, a 0.2 mg/ml TMV suspension was contacted with an Ox-PDMS surface for 30 minutes, the droplet was then allowed to dry with a stream of argon on the stamp surface. In this case, within the recessed region of the stamp structure, TMV particles appear to adsorb selectively and bind with enhanced end-to-end assembly at the edges (Figure 5.3b) similar to the surface aggregation reported by Nedoluzhko et al. [Nedoluzhko01]. Formation of selective adsorption of TMV particles on this region is highly reproducible. On the raised region of the stamp structures, no TMV particles were detected. More than 80% of the adsorbed TMV particles within the recessed regions were found to be present at the edges. Note that the argon stream applied to the virion suspension removed a very large fraction of the virions, which can also be observed by comparing Figure 5.3a with Figure 5.3b.
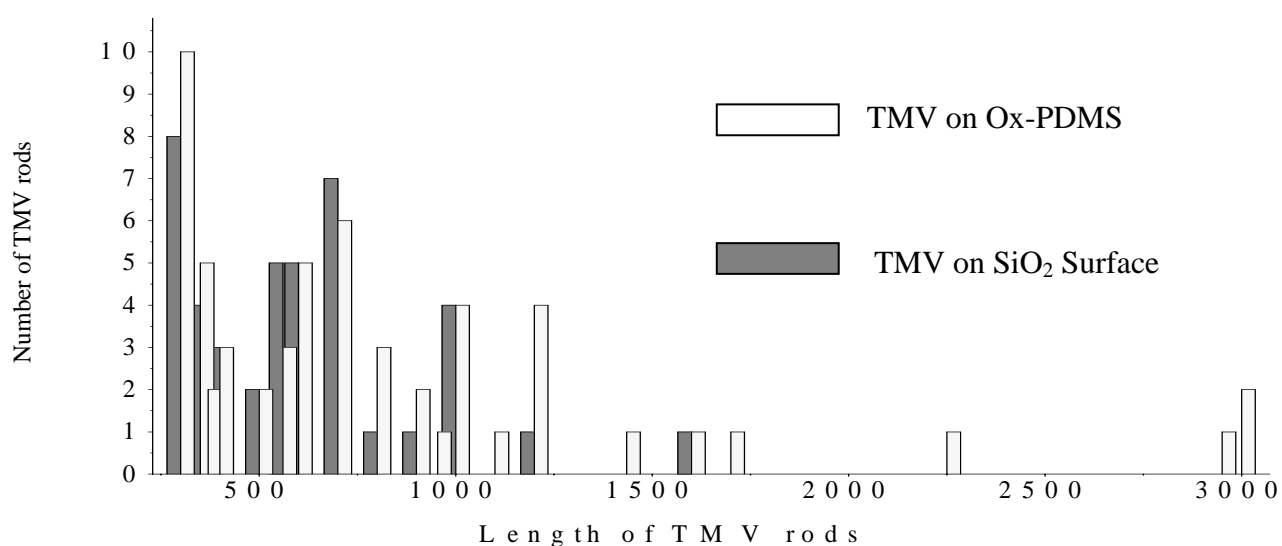
Figure 5.4: Length distribution of TMV rods (number versus length of the TMV rods in nm) at the edges within the recessed region of the Ox-PDMS structure and on the oxidized Si wafer.

The length of the end-to-end assembled virions at the edges within the recessed region of the stamp structure can reach up to several micrometers, (Figure 5.3b). Note that a single TMV particle is 300 nm in length. Figure 5.4 shows the length distribution of the virions at the edges within the recessed region of the stamp structure and also on the standard substrate, oxidized Si surface. Because of the

end-to-end aggregation in suspension, virions adsorbed on the oxidized Si surface (from 0.2 mg/ml suspension, scanned with AFM for length statistics) appear often to be longer than 300 nm; however such assemblies, which we can safely assume to exist already in suspension, are shorter than virion assemblies at the edges of the stamp structure. We only counted end-to-end assembled virions longer than 300 nm. As shown in the Figure 5.4, above 750 nm, the length difference between the TMV rods on two different surfaces is becoming obvious. Above this length scale, average length of the end-to-end aggregation on Ox-PDMS and oxidized Si surfaces is 1387±716 nm and 1052±256 nm, respectively. Hence virions assembled at the edges of the stamp structures are unusually long, although both surfaces are of comparable chemical nature (silica-like).

For both surfaces and also for suspensions, the tendency towards end-to-end assembly is based on the specific propensity of the coat protein to arrange helically even in the absence of the helix-stabilizing RNA [Butler99]. In other words, the protein-protein interactions operate towards helical arrangement in a single virion (see chapter 2.2), but similarly also for an end-to-end contact of two virions, which "interlock". The unusually long assemblies observed on stamps can be explained by decreased degrees of freedom for virions in a confined volume: During drying the stamp, virions diffuse inside a sub-µm scale droplet that wets the side of the positive features (see the following experiments and discussions). This process is slow, so virions can reorient until they fit optimally, and one can also suspect some orienting force along the feature edge (see also chapter 6.4).

We believe that the selective adsorption of the virions at the edges within the recessed region of the stamp structures is due to the dewetting of the water (inking solvent) during drying of the virus suspension on the stamp surface. This type of behavior of solvents on PDMS surfaces is due to discontinuous dewetting, which is selective inking of the sides and recesses of the stamp structure by solvents that dewet on the stamp surface [Jackman98,Cherniavskaya02]. This method has been used for large area patterning of molecular and nanoparticle materials with line widths of as small as 60 nm [Cherniavskaya02]. Originally, the method was used for filling large arrays of microwells with similar quantities of liquid in a very fast way, Scheme 5.2a [Jackman98]. The driving force for

the process is the difference in the interfacial free energies of the substrate and the liquid of interest, influenced additionally by the surface topography. The aspect ratio of the used wells changed from 1:50 to 1:1. The diameters (and depths) of the wells employed ranged between 2 µm (~1 µm deep), 10 µm (1-2 µm deep), 50 µm (1-50 µm deep), and 1000 µm (40-200 µm deep) [Jackman98]. Scheme 5.2 demonstrates a qualitative explanation: When a microwell is pulled from a solution, the bulk liquid retracts from the surface at a constant receding contact angle (dewetting angle). Upon reaching the top edge of the well, a sudden change in the contact angle pins a droplet to the edge. After reaching the equilibrium contact angle with the steep sidewall of the well, the bulk liquid breaks the connection to the droplet. Therefore, the well is filled with a droplet of well-defined size. Note that discontinuous dewetting was not shown for submicrometer dimensions.
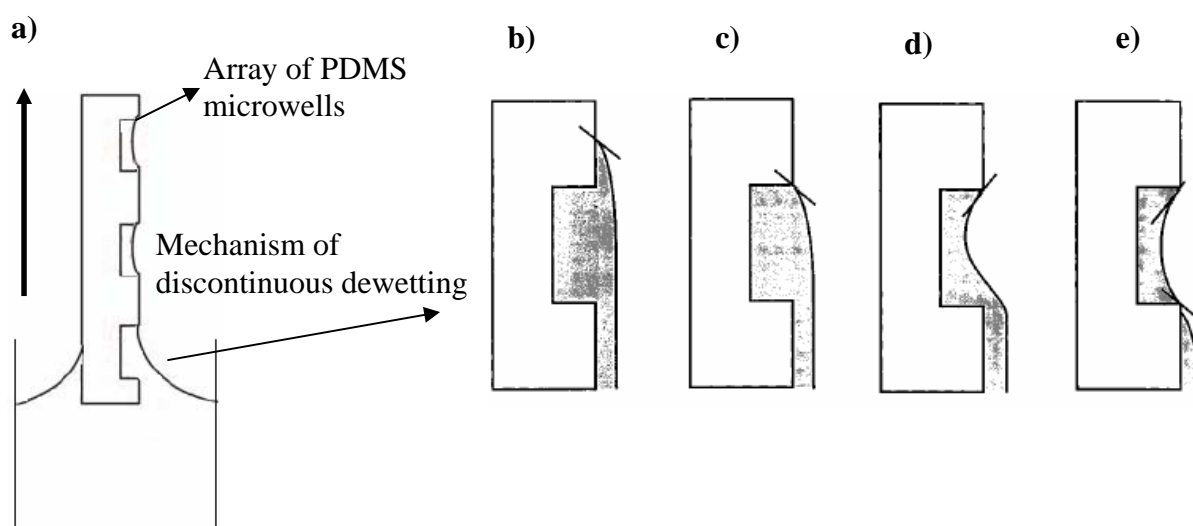
Scheme 5.2: Schematic illustration of the method of discontinuous dewetting and its mechanism. **(a)** Discontinuous dewetting: a large array of microwells is filled synchronously with liquid as it is pulled from a bulk solution. **(b)** Bulk liquid dewets on the surface with the receding contact angle (dewetting contact angle). **(c)** When reaching the top edge of the well, the contact angle suddenly changes and pins the droplet at the edge. **(d)** The droplet attaches to the end of the well as the bulk liquid recedes. **(e)** When the bulk liquid terminates the connection with the well, liquid is left behind [Jackman98].

By using the basic principles of the discontinuous dewetting phenomena, the mechanism of the selective adsorption of TMV particles can be described as in Scheme 5.3. TMV suspension is directly applied to the Ox-PDMS stamp surface. During drying of the TMV suspension, because of the dewetting of the ink solvent (water), the edge of the stamp structure is selectively inked by the TMV suspension (a liquid wedge formation). After complete evaporation of the water, TMV particles are selectively placed at the edges of the stamp structure, to be precise, at the bottom close to the steep slope of the positive relief features. In addition, selectively adsorbed TMV rods self assemble end-to-end. Of course, some TMV particles can be found far from the edge of the stamp structure as well.
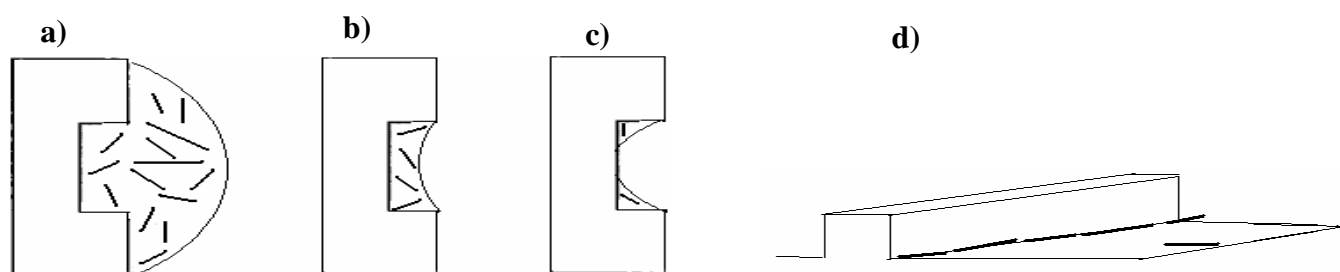
Scheme 5.3: Schematic representation of the assembly of TMV particles at edges within the recessed region of a stamp structure. **(a)** Inking of an (oxidized, thus hydrophilic) stamp with TMV suspension (side-view) **(b)** Dewetting of the ink solution during drying **(c)** Selective inking of the edges, formation of a liquid wedge **(d)** Assembled TMV particles at the edge, from one of the two wedges in (c) (top-view).

In order to prove that discontinuous dewetting plays an important role in line formation at the edges, we changed several experimental parameters, such as the solvent and the chemical nature of the stamp surface. A good method is to change the solvent water "stepwise" by using water-solvent mixtures with decreasing water content. We chose water-ethanol mixtures since the characteristics of pure ethanol on wet oxidized and pristine (hydrophobic) PDMS (very low contact angle) are

known. Contact angles on PDMS surface were measured. The solid-liquid interfacial energies were calculated with the *Young equation* [Owens69]:

Mixtures (v/v)	Measured-γ_{lv} (mN/m)	Measured-contact angle θ on PDMS (degrees)	Calculated-γ_{sl} (mN/m) on PDMS	Measured-contact angle θ on Ox-PDMS (degrees)	Calculated-γ_{sl} (mN/m) on Ox-PDMS
Water	72.60	112	48.2	0…10	-13.6…-12.5
Water-Ethanol (75:25)	41.30	87	18.8	0…10	17.7…18.3
Water-Ethanol (50:50)	28.52	68	10.3	0…10	30.5…30.9
Water-Ethanol (25:75)	25.30	55	6.5	0…10	33.7…34.1
Ethanol	22.52	32	1.9	0…10	36.5…36.8

Table 6.1: Interfacial energies of ethanol-water mixtures on PDMS surface. Calculated and measured values are indicated. Liquid-vapor interfacial energies are measured using *pendant-drop method*. Solid-liquid interfacial energies of the mixtures were calculated using the *Young equation*.

$$\gamma_{sl} = \gamma_{sv} - \gamma_{lv} \cos \theta \qquad\qquad (6.1)$$

A detailed explanation of equation (6.1) can be found in reference [Owens69]. Note that in all cases wetting (low contact angle) is favoured by low interfacial free energy (solid-liquid), high solid free energy (solid-vapor), and low liquid surface free energy (liquid-vapor) [Owens69]. The interfacial energies (γ_{sv}) for PDMS and ox-PDMS are ~21 mN/m and ~59 mN/m, respectively. [Jackman98] For the measurements of the interfacial energies of the liquids (γ_{lv}) we used a Dataphysics OCAH 230, which calculates the interfacial energy of a liquid (γ_{lv}) from the shape parameters of a liquid droplet, using the *pendant-drop method* [Jennings98]. The measured values for all the mixtures are given in Table 6.1. In addition, contact angles of all the mixtures on PDMS were measured, giving the desired interfacial energies (Table 6.1). After comparing these values for water-ethanol mixtures, it is clear that if the amount of ethanol in the mixture increases, the wetting behaviour of the mixture on PDMS improves.

In the same way, solid-liquid energies of ethanol and water can be calculated on Ox-PDMS (used in TMV line formation at the edges). However, because of the 'hydrophobic recovery' of the Ox-PDMS (see chapter 6.3.3) and the low contact angles of the liquids (ethanol and water), the same contact angle measurement like in the case of PDMS (not oxidized) is difficult to perform. All mixtures have contact angles below 15° immediately after oxidation of PDMS (as shown by the negative value for water, one has to be cautious to interpret these results for small ethanol fractions); but the exact value (even if it were 20°) has not much influence on the calculated γ_{sl}. It is, however, obvious that, even if the contact angle on Ox-PDMS decreases with increasing ethanol amounts, γ_{sl} increases, but only to very moderate values, determined by the small changes of γ_{lv} at high ethanol fractions. In other words, the mixture can be expected to wet the entire surface at ethanol fractions below 50%. Contrary to an expected change in wetting at intermediate ethanol fractions, in TMV suspensions with <75% ethanol used for inking the stamp surface, we observe dewetting and selective placement of virions within the recesses of the stamp structure, Figure 5.5a. Above 75% ethanol, the discontinuous dewetting begins to fail because the ethanolic suspension tends to coat (wet) the entire stamp surface. Therefore, randomly adsorbed TMV particles covering the entire surface were observed by AFM scanning, Figure 5.5b [Jackman98]. Note that now TMV particles do not show any selective assembly at all at the edges within the recessed region of the stamp structure. This result means that the Young equation can clearly not be applied here, because it gives the wrong trend and is unable to predict the sudden change at 75% ethanol.

It is likely that Ox-PDMS requires a more realistic treatment of its surface structure that is in fact combined of hydrophobic PDMS patches and hydrophilic "SiO$_x$-like" parts. Clearly, the latter is responsible for TMV binding, but our results suggest that patches of pure PDMS determine the wetting behavior ad thus the possibility to bring TMV to the surface. Moreover, TMV should be slightly mobile on pure PDMS (as on graphite).
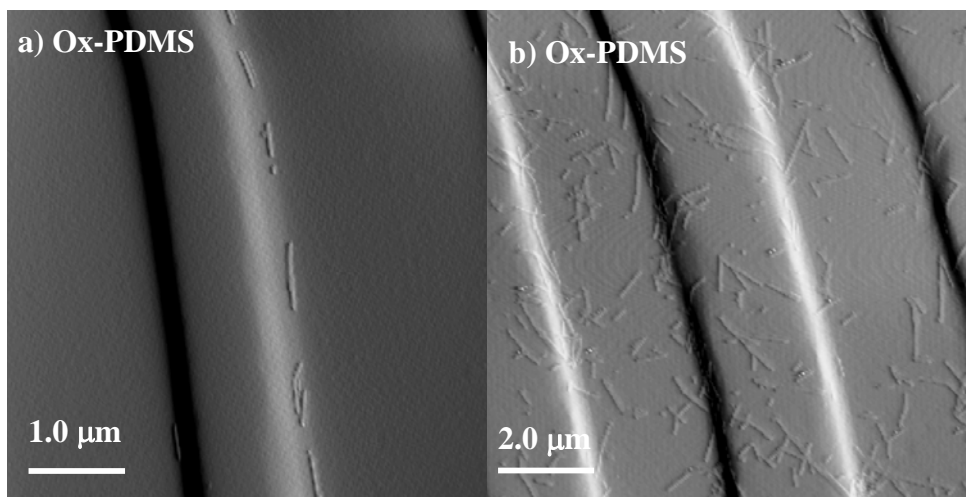
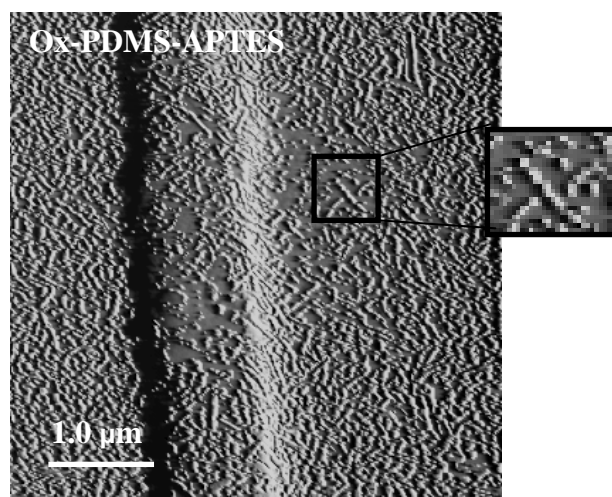**Figure 5.5:** AFM image (non-contact mode, error signal) of TMV particles on an oxygen plasma treated positive structured stamp surface from 0.2 mg/ml ethanolic suspensions of TMV. **(a)** End-to-end assemblies of TMV particles, generated by using 10% ethanolic suspension of TMV, can be discernible at the edges within the recessed region of the stamp structures. **(b)** Randomly adsorbed TMV particles generated by using 75% ethanolic suspension of TMV.

Furthermore, in order to show that the chemical nature of the stamp surface also plays an important role in dewetting, a chemical modification of the stamp surface with APTES was performed. The PDMS stamp was oxidized with an oxygen plasma and then immediately contacted for 2 minutes with APTES in pure water. APTES is covalently linked to the hydroxyl groups on the surface, and an amine-terminated surface is produced [Xia98,Dozel01]. Thereafter, a 0.2 mg/ml TMV suspension was applied to the surface, followed by drying with an argon stream. Again, blow-drying with an argon stream removes most of the TMV particles by expelling a large part of the suspension without drying. Figure 5.6 shows an AFM image of the APTES-modified stamp structure, which contains TMV particles covering the entire surface.

Figure 5.6: AFM image (non-contact mode, error signal) of the TMV particles on an APTES modified positive structured Ox-PDMS stamp surface from a 0.2 mg/ml virus suspension. The width of the stamp structure is around one micrometer. TMV particles cover the entire surface showing no selective adsorption at the edges within the recessed and raised regions of the stamp structure. The inset shows the enlarged part of the image in which TMV particles are discernible.

It is obvious that the chemical nature of the stamp surface affects the wetting behavior of the inking solvent. Selective adsorption of the TMV particles was lost due to the strong interaction (i.e. hydrogen bonding) between the APTES monolayer and the water. Therefore, TMV particles are adsorbed on the whole surface (see also chapter 6.5 for further discussion).

6.3.2 Edge Printing of Virus Particles

The selectively adsorbed virions observed at the edges within the recessed region of the positive stamp structures (Figure 5.3b) can be transferred by μCP to solid substrates, although only the raised regions of the stamp structure contact a flat solid surface. AFM observations revealed that many (but not all, see below) selectively placed TMV particles on the stamp were also aligned and assembled on the oxidized silicon substrates, Figure 5.7. The measured heights vary from 10 to 15 nm, which shows that the virions are not destroyed during printing [Knez04a].
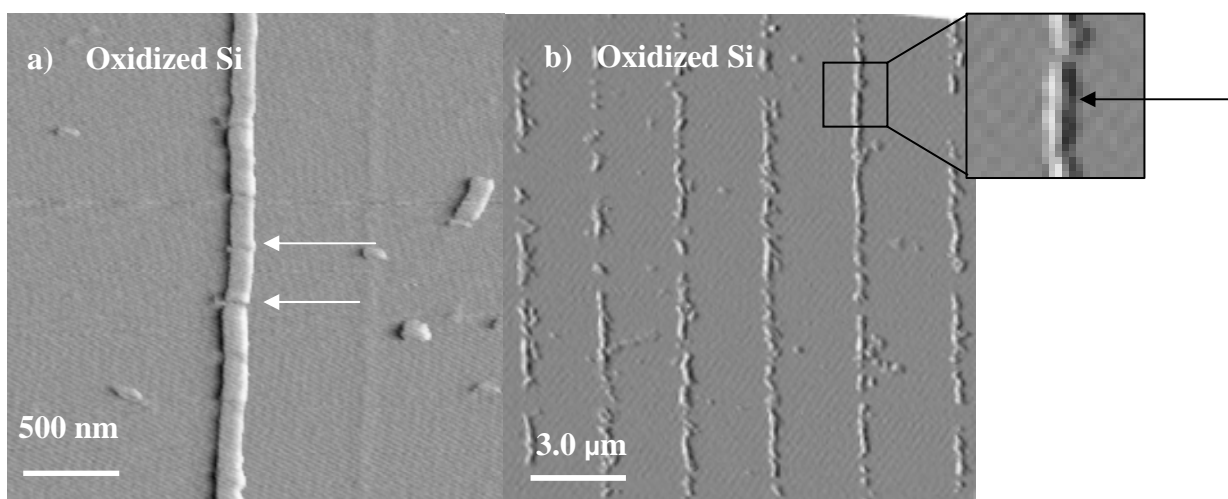
Figure 5.7: AFM images (non-contact mode, error signal) of the end-to-end assemblies of TMV particles, formed by printing on oxidized silicon wafers. The height of the virions is 10 nm [Knez04a]. **(a)** The gaps between individual, 300 nm long virus particles are clearly discernible. White arrows indicate the position of the gaps between the TMV rods. **(b)** Large area patterning (inset: zoomed-in region); the arrow indicates a gap in the printed virion line.

To gain more insight, we tested the mobility of virions on an Ox-PDMS surface by AFM: We never observed any mobility, see Figure 5.2. We note that virions can show some mobility, but only on hydrophobic surface (such as carbon) at elevated temperatures [Boes03]. Since the plasma easily reaches all recesses, the whole stamp surface, including the steep slopes of the relief structure, is hydrophilic. However, the printing of end-to-end assembled lines should involve transport of TMV particles from the edges of the stamp structure, see Scheme 5.4. We propose transport via a meniscus of adsorbed water, similar to the mechanism of dip-pen nanolithography (AFM tip side faces) or edge transfer lithography in µCP (stamp edges) [Cherniavskaya02,Piner99]. For this, one has to assume that the stamp was not completely dried or cannot be kept completely dry (air humidity). The water wedges (Scheme 5.4a) can now provide a way to move virions to a flat surface in contact with the stamp, certainly aided by capillary forces. If this mechanism is operating, one would not expect a complete transfer. Indeed, repeated printing experiments without reinking,

followed by AFM scanning of the stamp showed that TMV particles still reside at the edges within the recessed region of the stamp structure (see Figure 5.8). The transferred amount was so small that imaging on the solid substrate was not attempted.

a) After Inking   **b)** During Printing
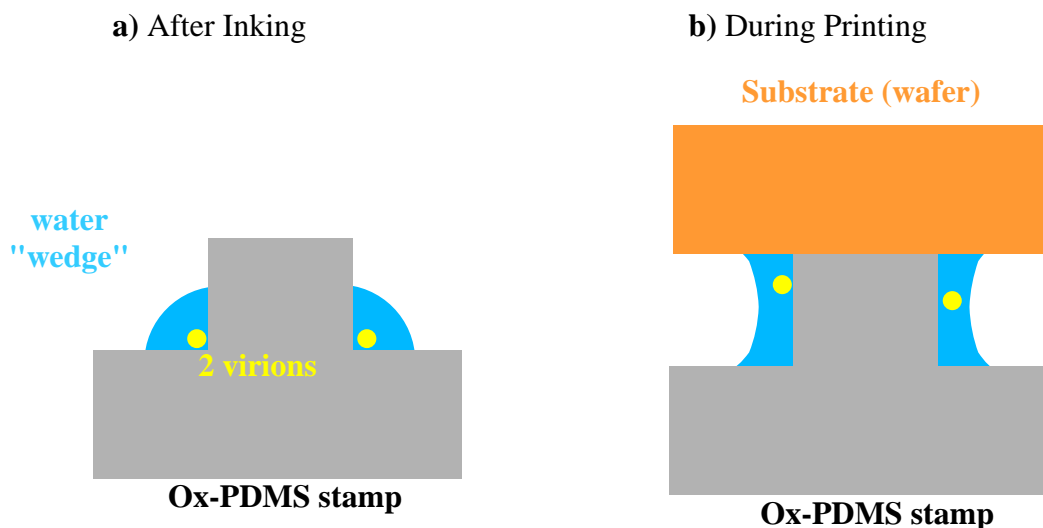
Scheme 5.4: Schematic representation of the transfer of virions in a water 'wedge'. **(a)** After dewetting of an ink on an Ox-PDMS stamp structure (side-view) **(b)** Transport of the virions via meniscus of adsorbed water from an Ox-PDMS stamp structure to a substrate.

The printed TMV lines on the solid substrate show a subtle difference to the lines on the stamps: They consist of multiple subunits with lengths of ~300 nm each, which perfectly matches the length of a single virion, separated by nm-sized gaps, Figure 5.7a. We ascribe these gaps to the aggregation of the virions. This means that the transport mechanism in the wedge can only operate for small units, which is sensible in view of the lower diffusion coefficient of end-to-end assembled virions. During capillary transport and probably also during drying of some remaining water, the transferred virions can interact with each other, while being confined to the stamp edges as in Scheme 5.3c. Similar to the enhanced end-to-end aggregation on the stamp due to complementary interactions between the ends of the helical structure, TMV particles again assemble linearly [Butler99,Lu96], but not perfectly. The lines appear slightly bent, but much longer than on the stamps. The reason is likely that here single virions have to interact – there is no elongated template

available. In contrast, end-to-end assembly in suspension or on stamps (see above) results in straight lines of 600-1500 nm length [Nedoluzhko01,Butler99], and the gaps can usually not be resolved in AFM images (only in TEM experiments, which have much higher lateral resolution than AFM). For example, in Figure 5.2a each virus particle consists of two TMV particles (presumably end-to-end assembled already in suspension), but no gap is resolved.
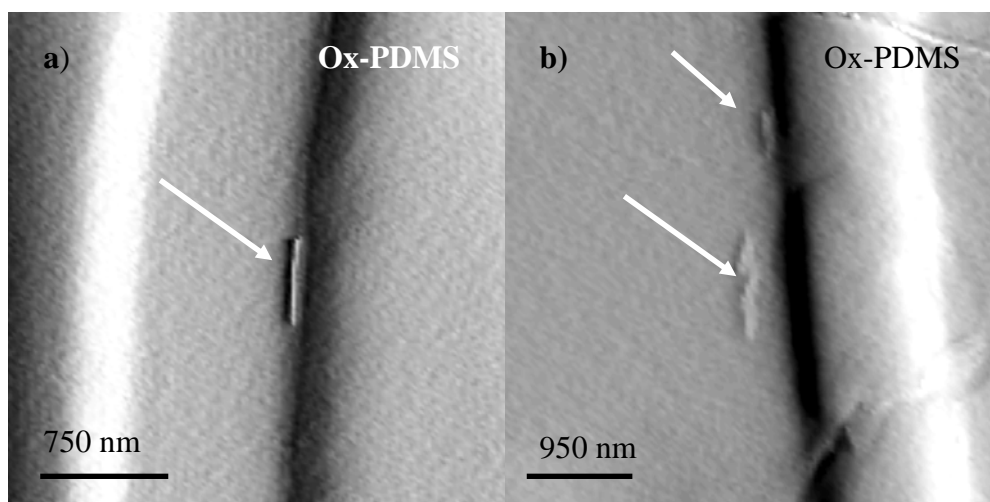

Figure 5.8: AFM images (non-contact mode, error signal) of TMV particles at edges within a recessed region of a stamp structure after repeated printing. Arrows indicate the virus particles. **(a)** After second printing, ~600 nm TMV rod at the edge **(b)** After third printing, ~900 nm and ~300 nm TMV rods at the edge.

In conclusion, μCP from *micrometer*-wide stamp structures can form *nanoscale* "chemical" patterns, i.e. the difference between the simple chemistry of the oxidized Si substrate and the complex reactivity of the virions can be exploited. The widths of the linear features in most cases do not exceed ~100 nm, which after subtraction of the AFM tip size corresponds to a maximum width of ~30 nm, corresponding to the width of a slightly flattened single virion.

6.3.3 Stamp Chemistry and ''Hydrophobic Recovery''

As it has been mentioned in previous section, the stamp chemistry plays an important role in the printing and alignment of the TMV particles on different surfaces. Therefore, the effects of an oxygen plasma treatment on the selective placement of TMV particles at the edges within the recessed region of the stamp structures were tested. For such experiments the static contact angles of water droplets on the Ox-PDMS surfaces were measured after various plasma exposure times. Pristine PDMS surfaces showed a contact angle of ~108°, characteristic for hydrophobic surfaces such as methyl-terminated molecular layers or polymers. After one-second oxygen plasma exposure, the surface is still hydrophobic, showing similar contact angles, and it is still impossible to adsorb virions on such surfaces [Knez04a]. After 2 seconds, the surface is becoming already very hydrophilic (contact angle ~10^0). Since contact angles below 10° are very hard to measure, we can assume complete hydrophilicity, comparable to clean glass or silica surfaces. On a technical note, it is impracticable to adjust plasma times or energies more finely in the TePla 100 machine, since the plasma energy is not measured, and because the spatial and temporal intensity shows slight variations (flickering). However, the produced surface is completely oxidized: There is not much difference in contact angles between 2 and 30 seconds plasma exposure, see Figure 5.9. The oxygen can be present in various chemical groups, all resulting in hydrophilicity. Thermodynamically, attachment to Si is preferred, resulting finally in a layer of silica (Si-O-Si and Si-OH groups). Taking this as a good approximation for the following discussion, supported by the observed crack formations after AFM scanning at high forces (Figure 5.2b), we note that also other structures such as hydroxymethyl groups should be formed.
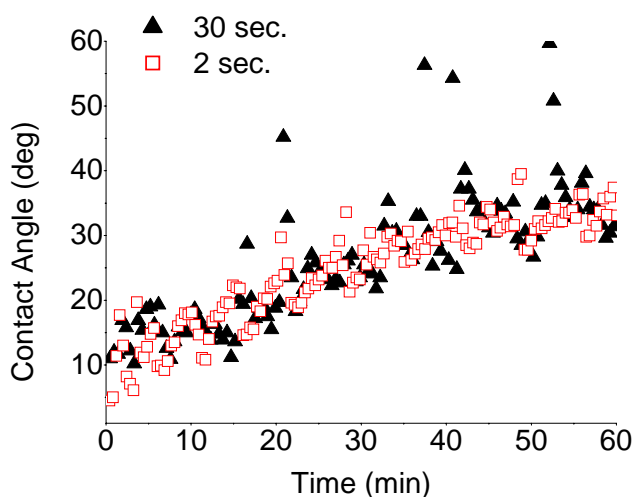
Figure 5.9: Contact angle as a function of the aging time of Ox-PDMS surfaces in air after exposure to 2 and 30 seconds of an oxygen plasma. Approximately two measurements were done for each minute of aging.

Ox-PDMS has been shown to represent a good ink transfer medium when using it as a template for patterning [Xia97]. However, some problems have been reported, especially that the hydrophilicity is slowly lost after oxygen plasma treatments. This change from a hydrophilic to a hydrophobic surface is called 'hydrophobic recovery' [Hilborg98,Hillborg00,Hillborg01]. The evolution of the contact angles with aging time in air is described in detail in Figure 5.9. It is believed that migration of low molecular mass PDMS and reorientation of hydrophilic groups from the surface into the bulk (e.g. by rotation around sigma bonds) replace hydroxyl groups by methyl groups in the surface region [Hilborg98,Hillborg01]. This mechanism is based on the very low glass transition temperature of PDMS (-123 ^{0}C), which is indicative for the very flexible nature of the backbone of the polymer [Hilborg98], but also for the mobility of at least the shorter chains. The recovery is suppressed when the oxidized stamps are stored in water [Donzel01]. Therefore, we stored Ox-PDMS in water before performing contact angle measurements, whenever measurements required more than some minutes.

The most important consequences are that the low contact angles of water on Ox-PDMS correlate perfectly with selective TMV transfer from positive features when the stamp was completely dried (chapter 6.3, first part), and with selective adsorption of TMV particles at the edges within the recessed region of the stamp structures in case of deliberate incomplete drying (see chapter 6.3.1).

6.4 Parallel Assembly of TMV Particles

Directional mechanical forces have already been applied to place DNA [Deng03] and nanowires [Huang01] in an aligned form on surfaces. In fact, the use of such forces has a much longer history, e.g. for the orientation of liquid crystals, and for the orientation of structures, e.g. of biological nature. Orientational mechanical forces have not been applied to deliberately orient shorter objects (in the submicrometer length scale) like TMV with its 300 nm length; however, liquid crystals and fibers of TMV and other virions show a high degree of alignment at very high concentrations of the respective suspensions.
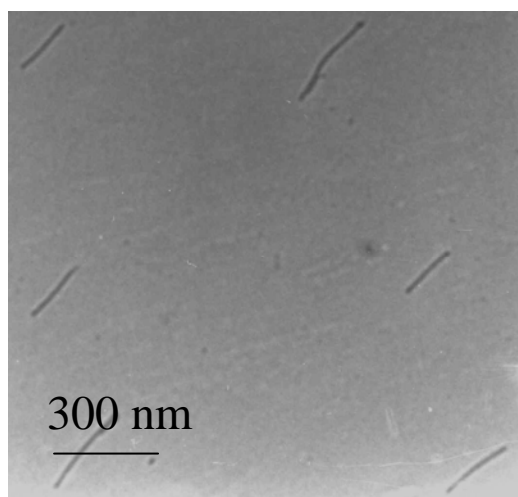
Figure 5.10: TEM micrograph of TMV particles assembled in parallel by applying lateral forces in the direction of liquid flow during adsorption on the carbon-coated polymer surface of a TEM grid.

Figure 5.10 shows an example for TMV assembled in parallel on a carbon-coated TEM grid. For such a parallel assembly of TMV rods, a 20 µl of 10 mg/ml TMV suspension (relatively high

concentration, but far below that required for forming liquid crystals) was placed on a carbon-coated Cu-TEM grid for 1 min, after which the droplet was removed by a filter paper touching the grid on one side. The capillary flow into the paper during drying generated the liquid flow, and no other forces were required (no argon stream drying). Before contacting the TMV suspension with the grid surface, the surface was activated with ethanol in order to increase the interaction between the carbon coated grid and the TMV particles. This treatment, together with the carbon coating, appears to be ideally suited for adsorbing a huge variety of biological objects. The reasons are not quite obvious; one can presume a mixture of hydrophobic graphitic areas and hydrophilic (oxygen-functionalized) areas, which are wetted by ethanol.
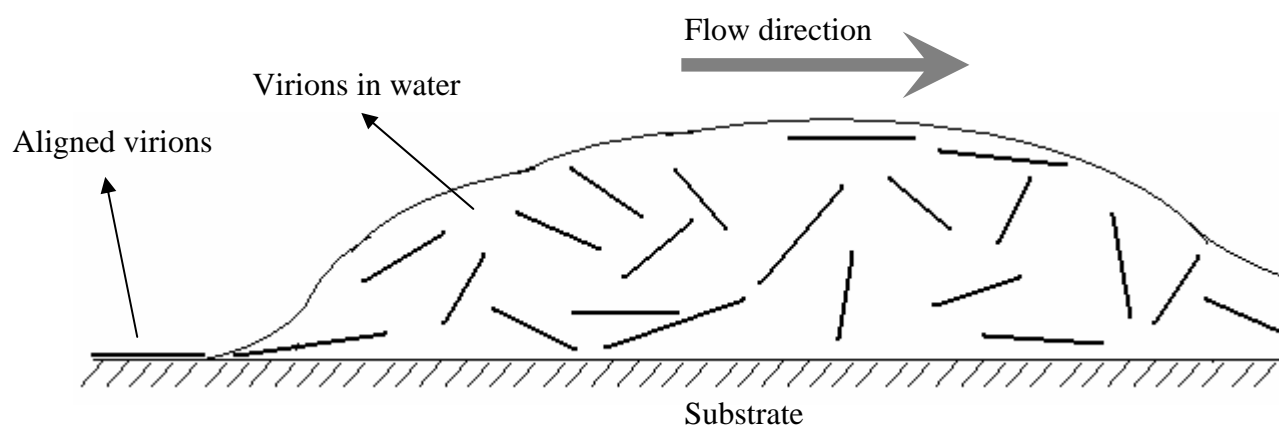
Scheme 5.5: Schematic representation of the alignment of the virions by directional mechanical forces. When a droplet of TMV solution on a surface is removed in one direction (by contacting it with a filter paper), the surface tension at the moving air-water interface is sufficient to stretch the virions along the flow direction of the droplet.

All TMV particles were aligned in the direction of the liquid flow, although the particles are separated by large distances, so that side-to-side interactions cannot operate. However, we tested that a similar alignment is not possible for surfaces in which interaction between the virions and the substrate surface is too strong or too weak, for example, mica, Ox-PDMS, and oxidized silicon

surfaces (that bind TMV very well [Knez04a]), or PDMS. These observations allow some considerations for the mechanism.

The alignment of the virions in the direction of the liquid flow, firstly, may start with an attachment of only one end of the virion, since this is much more likely than the immediate contact of the complete virion (Scheme 5.5) – this becomes clear from considering a rod tumbling in a solution. Subsequently, the virion is free to rotate around the pivotal point for some time before desorption or complete attachment. We believe that the surface tension at the moving air-water interface is stretching the TMV molecules in the direction of the liquid flow [Nakao03]. This phenomenon should also operate at the three-phase boundary (air/water/substrate) where some virions attach with only one end. The rotation is now suppressed by the directional force, such that finally the virions are adsorbed on the surface, aligned with the direction of the liquid flow. A high mobility of TMV on surfaces would mean that during or after adsorption, TMV can reorient. This should only be observed on hydrophobic surfaces where TMV adsorbs in very low quantity [Boes03]. The mobility on hydrophilic surfaces is very low [Knez04a], so that the orientational order remains.

6.5 Selective Assembly of TMV Particles

Preparing arrays of virus particles at individual feature sites [Vega05] on non-conductive substrates like silicon oxide is of great importance for measuring the physical properties of small assemblies or even single virions. In the case of low surface coverage, also single metallized virus particles could be easily accessed. In order to determine optimal feature sizes for the assembly of single virus particle, we studied, first for pristine TMV, a series of electron beam lithography (EBL) patterned templates of 3-aminopropyltriethoxysilane (APTES) with varied dimensions of (length x width) 4µm x 4µm to 4µm x100 nm.
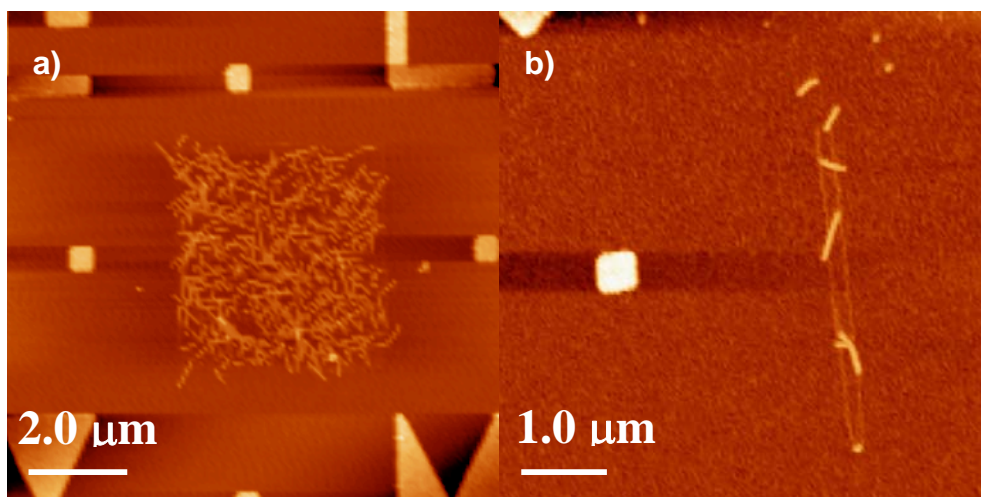
Figure 5.11: AFM images (non-contact, topography) of TMV particles assembled on predefined patterns of APTES template (bright large patches: coordinate markers) **(a)** large area (square) patterning **(b)** small area (rectangle) patterning.

These templates were incubated in TMV suspension and TMV particles selectively adsorbed on amine-terminated surfaces. Under the conditions studied, APTES templates with feature dimensions greater than 4µm x 200 nm were suitable for the selective adsorption of virus particles, Figure 5.11. The feature with 4µm x 200 nm was the smallest APTES template, on which individual TMV particles were discernible (Figure 5.11b). Instead of having a lot of virions in the same place like in Figure 5.11a, having a few virions in a very small region like in Figure 5.11b would be very useful in electrical contacting of the mineralized virions (Chapter 4). Virions adsorbed in well-defined areas appear to avoid contacting the surface outside the area. After generating very small templates, manipulation of single virions [Vega05] might be able to provide data on adhesion. Furthermore, certain collective properties such as magnetism depend sensitively on the number and orientation of the particles; a few cobalt-metallized virions arranged in this way would provide important insights in nanoscale magnetization phenomena such as phase transitions or domain boundaries.

Note that the results show 100% selectivity; there are no virions on the bare substrate. The silicon oxide surfaces used were not cleaned with the known RCA procedure and therefore the non-oxidized surface show hydrophobic behavior. It is very difficult to adsorb virions on such surfaces [Knez04a]. Cleaning with the RCA procedure might remove the coordinate markers on the chip due to the harsh conditions (ultrasonic treatment). However, even for a clean oxidized silicon, one should find good selectivity: The APTES features show not only hydrophilic character, but their amine functional groups attach more strongly to TMV: A protonated APTES surface is reported to have a pKa of approximately 4, therefore it is expected that the APTES species would be fully deprotonated at the working pH of ~7 [Vezenov97]. On the contrary, TMV has an isoelectric point at a pH value of about 3.5, and thus TMV particles are negatively charged at the working pH. Negatively charged TMV particles interact with the APTES monolayer via hydrogen bonding. This is different in the case of mica surface, which has a strong negative charge (one charge per ~0.468 nm^2) [Nishimura95]. However, after pretreatment with the (Mg^{2+}) ions solution, the cations are fixed on the negatively charged mica surface and therefore negatively charged TMV particles at neutral pH can be fixed onto the positively charged Mg^{2+}-mica surface. Vega and coworkers relied on thiohexadecanoic acid (MHA) nanotemplates (feature dimensions of 350 x 110 nm^2) on gold passivated with a monolayer of 11-thioundecyl-penta(ethylene glycol) [Vega05] (the passivation process minimizes the nonspecific binding of the virus particles). The carboxylic acid groups of MHA were coordinated to Zn^{2+} ions, whose coordination chemistry is essential for the virus particle assembly (TMV does not assemble on MHA without zinc ions). Here we demonstrate that assembly of virus particles on APTES is possible without adding metal ions. In addition, assembly of the virus particles on non-conductive surfaces (silicon oxide) could be advantageous for applications based on the electrical conductivity of metallized virus particles. Furthermore, the APTES templates can be chemically modified [Knez04a] with glutaraldehyde to yield an aldehyde group that could form an imine linkage with the amine functional groups on the outer surface of the virions, thereby even covalently linking them to the surface.

6.6 Conclusions

Based on the above experimental results, the following conclusions can be drawn from this part of the work:

(a) Microcontact printing of TMV particles on a variety of surfaces is possible if the chemistry of the surface of the siloxane-printing stamp is well controlled (introducing silica and/or hydroxyl groups by an oxygen plasma treatment). In this case, patterns can be filled with randomly arranged TMV particles. Unpatterned regions are completely free of virions.

(b) Careful control of the experimental parameters allows selective adsorption of TMV particles at the edges within the recessed region of a stamp structure. Such particles are composed of end-to-end assembled virions; the assemblies show enhanced lengths up to several μm, compared to simply adsorbed structures. The selective adsorption and orientation of the virions originates from discontinuous dewetting phenomena that place the TMV rods at the edges. In contrast to the adsorption of virions on flat surfaces, these virions appear to be mobile, allowing a rapid transfer of the structure to flat surfaces, which is likely based on some remaining water. About 30 nm wide linear patterns (single virion width) were printed from micrometer-sized stamp structures, thus proving a new simple principle for nanostructuring.

(c) By using directional mechanical forces it is possible to align TMV particles during their adsorption from a droplet of suspension. This method is known for long molecules such as DNA and nanowires; it is also working surprisingly well for shorter molecules like TMV.

(d) Finally, the selective assembly of virus particles on submicrometer scale amine-coated regions on a silicon oxide surface was shown. The method can be applied as a first step for addressing single nanoobjects, e.g. for electrical contacting.

In summary, TMV particles can be organized in mesoscale structures on surfaces with various simple and/or elegant surface-patterning techniques. These meso-and nanoscale patterns of TMV particles might be used as functional units in future nano-and optoelectronics in combination with various methods of mineralizing TMV particles. More generally, the structuring methods might be also used for other large molecules, and even for nanoobjects such as inorganic clusters.

CHAPTER 7

Conclusions

The work explained in this thesis is focused on using TMV as a bionanotemplate to synthesize metal and metaloxide nanostructures at different locations of the virus. The elemental composition of the synthesized nanomaterials is analyzed on the nanoscale. Furthermore, TMV particles are printed and aligned on a variety of surfaces. Combination of the printing and alignment processes with mineralization of TMV is expected to expand its functionality in nanoscience.

Based on the experimental results described in the chapters 4-6, the following conclusions can be drawn:

It has been shown that a variety of different materials can be deposited on the specific locations (within the central channel, on the outer surface as well as at the ends) of the TMV particles in a very controlled way by using electroless deposition (ELD) method. New Ni and Cu ELD baths compatible with the TMV particles (but also other pH-sensitive substrates) were developed in order to produce Ni and Cu nanowires within the central channel of the TMV. Energy filtering transmission electron microscopy (EFTEM) experiments for Ni, Co, and Cu nanowires showed that the nanowires within the central channel of TMV particles consist solely of the corresponding expected elements in the ELD baths. The sensitivities for cobalt and nickel are higher than for copper in the elemental maps since copper spectra do not possess sharp "white lines" in the energy

loss spectra, and the Cu $L_{2,3}$ edge is located at higher energy than that of cobalt and nickel. Moreover, high resolution TEM (HRTEM) imaging of the nickel nanowires within the central channel of the virions showed crystalline structures with regularly spaced lattice planes. In the same way, the structure of other nanowires within the virus central channel could be investigated using HRTEM. Besides that as a first step for contacting nanowires inside the virus particles, electrical transport measurements on TMV rods adsorbed on silicon oxide surfaces were performed. It has been shown that TMV rods are insulators at room temperature and in vacuum (4-6x10^{-5}mbar). In the future, contacting nanowires within the central channel of the virions could be performed in a similar way.

Like Co, Ni, and Cu nanowires, it is possible to generate alloy nanowires within the central channel of the virus. Instead of using one metal ion source in the ELD bath, two or more of them produce alloy nanowires. For example, using Co and Fe in the same ELD bath, CoFe alloy nanowires with a chemical composition of about 90:10 Co:Fe within the central channel of TMV particles were produced. It is believed that it is possible to generate other alloy nanowires by varying the ELD bath formulations. The literature contains a quite large number of ELD baths that can produce bulk alloys. However, attention must be paid to the compatibility of the ELD baths with the TMV particles, because the virions can be destroyed by harsh conditions of such as high pH values or very strong reductants. In the future, after isolation of the metallized virions, magnetic properties of the individual Ni, Co, and CoFe nanowires within the central channel of the virus could be obtained using superconducting quantum interference device (SQUID). Alternatively, without isolation of the nanowires, magnetic properties of a single nanowire (local magnetic properties) could be obtained by using spin polarized scanning electron microscopy (SPSEM) or magnetic force microscopy (MFM) techniques.

A similar electroless process can deposit ZnO on the outer surface of the TMV particles from a nitrate-containing bath. The deposited material has been confirmed to be composed of Zn and O

with a chemical composition of about 70:30 Zn:O. The large deviation from the expected value (50:50) is attributed to the broad zinc peak in the electron energy loss spectrum. It is believed that in the future ZnO could be also produced within the central channel of the TMV. One can for example use other catalysts rather than Pd (II) in the activation of the virions or change the ZnO deposition rate by changing the concentration of the ingredients in the ELD baths. The ZnO deposition mechanism is based on the presence of nitrate, but has not been fully understood. Experiments showed that nitrite is not present at the beginning of the deposition reaction (30 min). Therefore, the nitrate present at the beginning of the ELD reaction must be further reduced to other species like NO. In addition, a new ZnO growth mechanism based on the experimental observations was suggested. Cathodoluminescence measurements from the ZnO rods containing TMV cores on carbon coated TEM grid has shown that ZnO deposited on the outer surface of the virus has a band gap energy of ~3.36 eV, which correlates with the bulk value.

6 nm gold nanoparticles (Au-nps) were selectively attached to the ends of the TMV particles and size-enhanced by electroless deposition of gold. It is believed that the heterocylic aromatic bases of the RNA of TMV interact with the Au-np surface (replacing citrate molecules on the Au-np surface). In this way, without using any antibodies or crosslinking agents, still excellent selectivity has been achieved. In other experiment, an enzyme removed the coat protein of the TMV particles and successive incubation with 6 nm gold sols generated self-assembled Au-nps around the TMV-RNA. Therefore, RNA plays an important role in assembly of Au-nps at the ends of the virus. In addition, the assembled Au-nps were size-enhanced by electroless deposition of gold, which results in generation of dumbbell-shaped structures.

Microcontact printing of the TMV particles on a variety of surfaces has been achieved when the chemistry of the surface of the siloxane-printing stamp is well controlled (introducing hydroxyl groups with an oxygen plasma treatment). In this case, patterns can be filled with randomly arranged TMV particles. Moreover, selective adsorption of end-to-end assembled TMV particles was obtained at the edges within the recessed region of the stamp structure by carefully controlling

the experimental parameters. Selective assembly of the virions is attributed to the dewetting of the inking solvent on the stamp surface. These assembled virions were also transferred to the SiO_2 surfaces. Therefore, it is shown that, TMV molecules can be printed and aligned simultaneously.

Directional mechanical forces generated aligned TMV rods in the central direction of the liquid flow on solid surfaces. These forces have been applied for long molecules such as DNA and nanowires; however, this is also working for shorter molecules like TMV. In another experiment, TMV particles were selectively assembled on aminopropyltriethoxysilane (APTES) templates on silicon oxide surfaces, which might be very useful for measuring the electrical properties of the metallized virus particles.

Bibliography

[Adamson73] A. W. Adamson, *A Textbook of Physical Chemistry,* Academic Press, (New York and London, 1973).

[Alim05] K. A. Alim, V. A. Fonoberov, and A. A. Balandin, *Appl. Phys. Lett.* **86,** 053103 (2005).

[Alivisatos96] A. P. Alivisatos, *Science* **271,** 933 (1996).

[Andricacos98a] P. C. Andricacos, and N. Robertson, *IBM J. Res. Develop.* **42,** 671 (1998).

[Andricacos98] P. C. Andricacos, C. Uzoh, J. O. Dukovic, J. Horkans, and H. Deligianni, *IBM. J. Res. Develop.* **42,** 567 (1998).

[Barr78] T. L. Barr, *J. Phys. Chem.* **82,** 1801 (1978).

[Baeuerlein00] E. Baeuerlein, *Biomineralization,* Wiley-Vch, (Weinheim, 2000).

[Belin05] T. Belin, and F. Epron, *Mater. Sci. Eng. B* **119,** 105, (2005).

[Berger92] A. Berger, and H. Kohl, *Microsc. Microanal. Microstruct.* **3,** 159 (1992).

[Bernard00] A. Bernard, J. F. Renault, B. Michel, H. R. Bosshard, and E. Delamarche, *Adv. Mater.* **12,** 1067, (2000).

[Biebuyck97] H. A. Biebuyck, N. B. Larsen, E. Delamarche, and B. Michel, *IBM J. Res. Develop.* **41,** 159 (1997).

[Biggs94] S. Biggs, P. Mulvaney, C. F. Zukoski, and F. Grieser, *J. Am. Chem. Soc.* **116,** 9150 (1994).

[Binnig86] G. Binnig, C. F. Quate, and C. Gerber, *Phys. Rev. Lett.* **56,** 930, (1986).

[Bittner02] A. M. Bittner, X. C. Wu, and K. Kern, *Adv. Funct. Mater.* **12,** 432 (2002).

[Boes03] F. Boes, *Studienarbeit*, (Stuttgart, 2003).

[Bos99] L. Boss, *Phil. Trans. R. Soc. Lond.* **B 354,** 537 (1999).

[Bothner04] B. Bothner, and G. Siuzdak, *ChemBioChem* **5,** 258 (2004).

[Braun98] E. Braun, Y. Eichen, U. Sivan, and G. Ben-Yoseph, *Nature* **391,** 775 (1998).

[Burke92] L. D. Burke, and B. H. Lee, *J. Appl. Electrochem.* **22,** 48 (1992).

[Butler99] P. J. G. Butler, *Phil. Trans. R. Soc. Lond.* **B 354,** 537(1999).

[Calhoun83] D. B. Calhoun, J. M. Vanderkooi, G. V. Woodrow III, and S. W. Englander, *Biochemistry* **22,** 1526 (1983).

[Campbell99] D. J. Campbell, K. J. Beckman, C. E. Calderon, P. W. Doolan, R. M. Ottosen, A. B. Ellis, and G. C. Lisensky, *J. Chem. Educ.* **75,** 537 (1999).

[Cardenas05] M. Cardenas, K. Schillen, D. Pebalk, T. Nylander, and B. Lindman, *Biomacromolecules* **6,** 832 (2005).

[Cardenas06] M. Cardenas, J. Barauskas, K. Schillen, J. L. Brennan, M. Brust, and T. Nylander, *Langmuir* **22,** 3294 (2006).

[Cavallini03] M. Cavallini, and F. Biscarini, *Nano Lett.* **3,** 1269 (2003).

[Cherniavskaya02] O. Cherniavskaya, A. Adzic, C. Knutson, B. J. Gross, L. Zang, R. Liu, and D. M. Adams, *Langmuir* **18,** 7029, (2002).

[Chou97] S. Y. Chou, P. R. Kraus, W. Zhang, L. Guo, and L. Zhuang, *J. Vac. Sci. Technol. B* **15,** 2897 (1997).

[Chung05] S. W. Chung, D. S. Ginger, M. W. Morales, Z. Zhang, V. Chandrasekhar, M. A. Ratner, and C. A. Mirkin, *Small* **1,** 64 (2005).

[Cosgrove05] T. Cosgrove, *Colloid Science*, Blackwell Publishing, (Bristol, 2005).

[Culver02] J. N. Culver, *Annu. Rev. Phytopathol.* **40,** 287 (2002).

[Deggelmann94] M. Deggelmann, C. Gaf, M. Haganbüchle, U. Hoss, C. Johner, H. Kramer, C. Martin, and R. Weber, *J. Phys. Chem.* **98,** 364 (1994).

[Demir03] M. Demir, and M. H. B. Stowell, *Nanotechnology* **13,** 541 (2003).

[Deng03] Z. Deng, and C. Mao, Nano Lett. **3,** 1545 (2003).

[Dima03] G. E. Dima, A. C. A. De Vooys, and M. T. M. Koper, *J. Electroanal. Chem.* **554,** 15 (2003).

[Diamand95] Y. Shacham-Diamand, V. Dubin, and M. Angyal, *Thin Solid Films* **262,** 93 (1995).

[Diamand97] Y. Shacham-Diamand, and V. M. Dubin, *Microelectr. Eng.* **33,** 47 (1997).

[Diamand03] Y. Shacham-Diamand, A. Inberg, Y. Sverdlov, V. Bogush, N. Croitoru, H. Moscovich, and A. Freeman, *Electrochim. Acta* **48,** 2987 (2003).

[Donzel01] C. Donzel, M. Geissler, A. Bernard, H. Wolf, B. Michel, J. Hilborn, and E. Delamarche, *Adv. Mater.* **13,** 1164 (2001).

[Drygin98] Y. F. Drygin, O. A. Bordunova, M. O. Gallyamov, and I. V. Yaminsky, *FEBS Lett.* **425,** 217 (1998).

[Dujardin03] E. Dujardin, C. Peet, G. Stubbs, J. N. Culver, and S. Mann, *Nano Lett.* **3,** 413 (2003).

[Egerton96] R. F. Egerton, *Electron Energy-Loss Spectroscopy in the Electron Microscopy,* Plenum Press, (New York and London, 1996).

[Falkner05] J. C. Falkner, M. E. Turner, J. K. Bosworth, T. J. Trentler, J. E. Johnson, T. Lin, and V. L. Colvin, *J. Am. Chem. Soc.* **127,** 5274, (2005).

[Fernandez05] J. R. Fernandez, J. P. Juste, P. Mulvaney, and L. M. L. Marzan, *J. Phys. Chem. B* **109,** 14257 (2005).

[Fink99] H. W. Fink, and C. Schönenberger, *Nature* **398,** 407 (1999).

[Fritz74] J. S. Fritz, and G. H. Schenk, *Quantitative Analytical Chemistry,* Allyn and Bacon, Inc., (Boston, 1974).

[Gallagher83] W. H. Gallagher, and M. A. Lauffer, *J. Mol. Biol.* **170,** 921, (1983).

[Givord03] D. Givord, *Europhys. News* **34,** 6 (2003).

[Grobert01] N. Grobert, M. Mayne, M. Terrones, J. Sloan, R. E. Dunin-Borkowski, R. Kamalakaran, T. Seeger, H. Terrones, M. Rühle, D. R. M. Walton, H. W. Kroto, and J. L. Hutchison, *Chem. Comm.,* 471, (2001).

[Hillborg98] H. Hillborg, and U. W. Gedde, *Polymer* **39,** 1991 (1998).

[Hillborg00] H. Hillborg, J. F. Ankner, U.W. Gedde, G. D. Smith, H. K. Yasuda, and K. Wikström, *Polymer* **41,** 6851 (2000).

[Hillborg01] H. Hillborg, S. Karlsson, and U. W. Gedde, *Polymer* **42,** 8883 (2001).

[Huang01] M. H. Huang, S. Mao, H. Feick, H. Yan, Y. Wu, H. Kind, E. Weber, R. Russo, and P. Yang, *Science* **292,** 1897 (2001).

[Hung86] A. Hung, *J. Electrochem. Soc.* **133,** 1350 (1986).

[Izaki96] M. Izaki, and T. Omi, *Appl. Phys. Lett.* **68,** 2439 (1996).

[Izaki97] M. Izaki, and T. Omi, *J. Electrochem. Soc.* **144,** L3 (1997).

[Izaki00] M. Izaki, and J. Katayama, *J. Electrochem. Soc.* **147,** 210 (2000).

[Jackman98] R. J. Jackman, D. C. Duffy, E. Ostuni, N. D. Willmore, and G. M. Whitesides, *Anal. Chem.* **70,** 2280 (1998).

[Jagannathan93] R. Jagannathan, and M. Krishnan, *IBM. J. Res. Develop.* **37,** 117 (1993).

[Jana01] N. R. Jana, L. Gearheart, and C. J. Murphy, *J. Phys. Chem. B* **105,** 4065 (2001).

[Jennings88] J. W. Jennings, Jr., and N. R. Pallas, *Langmuir* **4,** 959 (1988).

[Juste04] J. P. Juste, L. M. L. Marzan, S. Carnie, D. Y. C. Chan, and P. Mulvaney, *Adv. Funct. Mater.* **14,** 571 (2004).

[Kasap00] S. O. Kasap, *Principles of Electronic Materials and Devices,* McGraw Hill, (Boston, 2000).

[Kang03] J. W. Kang, and H. J. Hwang, *Comput. Mater. Sci.* **27,** 305 (2003).

[Kausche39] G. A. Kaushe, and H. Ruska, *Kolloid Z.* **89,** 21 (1939).

[Kazakova05] O. Kazakova, D. Erts, T. A. Crowley, J. S. Kulkarni, and J. D. Homes, *J. Magn. Magn. Mater.* **286**, 171 (2005).

[Keren02] K. Keren, M. Krueger, R. Gilad, G. B. Yoseph, U. Sivan, and E. Braun, *Science* **297,** 72 (2002).

[Kern90] W. Kern, *J. Electrochem. Soc.* **137,** 1887 (1990).

[Kim04] J. H. Kim, S. H. Ehrman, and T. A. Germer, *Appl. Phys. Lett.* **84,** 1278 (2004).

[Kind98] H. Kind, A. M. Bittner, O. Cavalleri, and K. Kern, *J. Phys. Chem. B* **102,** 7582 (1998).

[Kittel53] C. Kittel, *Introduction to Solid State Physics,* John Wiley & Sons, (London, 1953).

[Klug99] A. Klug, *Phil. Trans. R. Lond. B.* **354,** 531 (1999).

[Knez03] M. Knez, *Ph.D. Thesis,* (Ulm, 2003).

[Knez04] M. Knez, A. M. Bittner, F. Boes, C. Wege, H. Jeske, E. Maiß, and K. Kern, *Nano Lett.* **3,** 1079 (2004).

[Knez04a] M. Knez, M. P. Sumser, A. M. Bittner, C. Wege, H. Jeske, D. M. P. Hoffmann, K. Kuhnke, and K. Kern, *Langmuir* **20,** 441 (2004).

[Knez04b] M. Knez, M. Sumser, A. M. Bittner, C. Wege, H. Jeske, T. P. Martin, and K. Kern, *Adv. Funct. Mater.* **14,** 116 (2004).

[Knez06] M. Knez, A. Kadri, C. Wege, U. Gösele, H. Jeske, and K. Nielsch, *Nano Lett.*, 2006, *In press.*

[Kolb97] D. M. Kolb, R. Ullmann, and T. Will, *Science* **275,** 1097 (1997).

[Krämer95] J. L. C. Krämer, N. Garcia, P. G. Mochales, and P. A. Seran, *Surf. Sci.* **342,** L1144 (1995).

[Kumar93] A. Kumar, and G. M. Whitesides, *Appl. Phys. Lett.* **63,** 2002 (1993).

[Lallemand04] F. Lallemand, L. Ricq, M. Wery, P. Bercot, and J. Pagetti, *Surf. Coat. Technol.* **179,** 314 (2004).

[Larson97] I. Larson, D. Y. C. Chan, C. J. Drummond, and F. Grieser, *Langmuir* **13,** 2429 (1997).

[Leapman82] R. D. Leapman, L. A. Grunes, and P. L. Fejes, *Phys. Rev. B* **26,** 614, (1982).

[Leapman91] R. D. Leapman, and J. A. Hunt, *Microsc. Microanal. Microstruct.* **2,** 231, (1991).

[Lee05] S. Y. Lee, E. Royston, J. N. Culver, and M. T. Harris, *Nanotechnology* **16,** S435 (2005).

[Lewis96] D. B. Lewis, and G. W. Marshall, *Surf. Coat. Technol.* **78,** 150 (1996).

[Lu96] S. Lu, G. Stubbs, and J. N. Culver, *Virology* **225,** 11 (1996).

[Lussi05] J. W. Lussi, C. Tang, P. A. Kuenzi, U. Staufer, G. Csucs, J. Vörös, G. Danuser, J. A. Hubbell, and M. Textor, *Nanotechnology* **16,** 1781 (2005).

[Mackay96] K. M. Mackay, R. A. Mackay, and W. Henderson, *Introduction to Modern Inorganic chemistry,* Stanley Thornes (Publishers) Ltd, (Cheltenham, 1996)

[Mallory90] G. O. Mallory, and J. B. Hajdu, *Electroless Plating: Fundamentals and Applications,* American Electroplaters and Surface Finishers Society, (Florida, 1990).

[Mao04] C. Mao, D. J. Solis, B. D. Reiss, S. T. Kottmann, R. Y. Sweeney, A. Hayhurst, G. Georgiou, B. Iverson, and A. M. Belcher, *Science* **303,** 213 (2004).

[Mertig98] M. Mertig, R. Kirsch, and W. Pompe, *Appl. Phys.* **A 66,** S723 (1998).

[Mertig02] M. Mertig, L. C. Ciacchi, R. Seidel, and W. Pompe, *Nano Lett.* **2,** 841 (2002).

[Michel02] R. Michel, J. W. Lussi, G. Csucs, I. Reviakine, G. Danuser, B. Ketterer, J. A. Hubbell, M. Textor, and N. D. Spencer, *Langmuir* **18,** 3281 (2002).

[Monson03] C. F. Monson, and A. T. Woolley, *Nano Lett.* **3,** 359 (2003).

[Mori02] K. Mori, K. Yamaguchi, T. Hara, T. Mizugaki, K. Ebitani, and K. Kaneda, *J. Am. Chem. Soc.* **124,** 11572 (2002).

[Mori04] K. Mori, T. Hara, T. Mizugaki, K. Ebitani, and K. Kaneda, *J. Am. Chem. Soc.* **126,** 10657 (2004).

[Myung01] N. V. Myung, and K. Nobe, *J. Electrochem. Soc.* **148,** C136 (2001).

[Nakao03] H. Nakao, M. Gad, S. Sugiyama, K. Otobe, and T. Ohtani, *J. Am. Chem. Soc.***125,** 7162, (2003).

[Nakahara83] S. Nakahara, and Y. Okinaka, *Acta Metal.* **31,** 713 (1983).

[Nakai01] H. Nakai, T. Homma, I. Komatsu, and T. Osaka, *J. Phys. Chem. B* **105,** 1701 (2001).

[Nakanishi05] T. Nakanishi, Y. Masuda, and K. Koumoto, *J. Crystal Growth* **284,** 176 (2005).

[Namba89] K. Namba, R. Pattanayek, and G. Stubbs, *J. Mol. Biol.* **208,** 307 (1989).

[Nedoluzhko01] A. Nedoluzhko, and T. Douglas, J. *Inorg. Biochem.* **84,** 233 (2001).

[Nishimura95] S. Nishimura, P. J. Scales, H. Tateyama, K. Tsunematsu, and T. W. Healy, *Langmuir* **11,** 291 (1995).

[Okahata98] Y. Okahata, T. Kobayashi, K. Tanaka, and M. Shimomura, *J. Am. Chem. Soc.* **120,** 6165 (1998).

[Ostmann06] T. K. Ostmann, C. Jördens, and K. Baaske, *Appl. Phys. Lett.* **88,** 102102 (2006).

[Owens69] D. K. Owens, and R. C. Wendt, *J. Appl. Poly. Sci.* **13,** 1741 (1969).

[Piner99] D. Piner, J. Zhu, F. Xu, S. Hong, and C. A. Mirkin, *Science* **283,** 661(1999).

[Pompe99] T. Pompe, A. Fery, S. Herminghaus, A. Kriele, H. Lorenz, and J. P. Kotthaus, *Langmuir* **15,** 2398 (1999).

[Porath00] D. Porath, A. Bezryadin, S. de Vries, and C. Dekker, *Nature* **403,** 635 (2000).

[Porter02] L. A. Porter, Jr., H. C. Choi, A. E. Ribbe, and J. M. Buriak, *Nano Lett.* **2,** 1067 (2002).

[Pourbaix66] M. Pourbaix, *Atlas of Electrochemical Equilibria in Aqueous Solutions,* National Association of Corrosion Engineers, (Texas, 1966).

[Pradhan99] B. K. Pradhan, T. Kyotani, and A. Tomita, *Chem. Commun.,* 1317 (1999).

[Reches03] M. Reches, and E. Gazit, *Science* **300**, 625 (2003).

[Reiss04] B. D. Reiss, C. Mao, D. J. Solis, K. S. Ryan, T. Thomson, and A. M. Belcher, *Nano Lett.* **4,** 1127 (2004).

[Rellinghaus01] B. Rellinghaus, S. Stappert, E. F. Wassermann, H. Sauer, and B. Spliethoff, *Eur. Phys. J. D* **16,** 249 (2001).

[Richter01] J. Richter, M. Mertig, and W. Pompe, *Appl. Phys. Lett.* **78,** 536 (2001).

[Rodes95] A. Rodes, R. Gomez, J. M. Orts, J. M. Feliu, J. M. Perez, and A. Aldaz, *Langmuir* **11,** 3549 (1995).

[Routier97] S. Routier, J. L. Bernier, J. P. Catteau, P. Colson, C. Houssier, C. Rivalle, E. Bisagni, and C. Bailly, *Bioconjugate Chem.* **8,** 789 (1997).

[Runyan90] W. R. Runyan, and K. E. Bean, *Semiconductor Integrated Circuit Processing Technology,* Addison-Wesley Publishing Company, (Massachusetts, 1990).

[Sadik05] O. A. Sadik, H. Xu, and A. Sargent, *J. Electroanal. Chem.* **583,** 167 (2005).

[Saito98] T. Saito, E. Sato, M. Matsuoka, and C. Iwakura, *J. Appl. Electrochem.* **28**, 559 (1998).

[Saito02] N. Saito, H. Haneda, T. Sekiguchi, N. Ohashi, I. Sakaguchi, and K. Koumoto, Adv. Mater. 14, 418 (2002).

[Sandroff85] C. F. Sandroff, and D. R. Herschbach, *Langmuir* **1,** 131 (1985).

[Sandström03] P. Sandström, M. Boncheva, and B. Akerman, *Langmuir* **19,** 7537 (2003).

[Schlesinger00] M. Schlesinger, and M. Paunovic, *Modern Electroplating,* John Wiley & Sons, Inc., (New York, 2000).

[Schlick05] T. L. Schlick, Z. Ding, E. W. Kovacs, and M. B. Francis, *J. Am. Chem. Soc.* **127,** 3718 (2005).

[Scholthof04] K. G. Scholthof, *Annu. Rev. Phytopathol.* **42,** 13 (2004).

[Seidel04] R. Seidel, L. C. Ciacchi, M. Weigel, W. Pompe, and M. Mertig, *J. Phys. Chem. B* **108,** 10801 (2004).

[Shapiro77] S. M. Shapiro, and S. C. Moss, *Phys. Rev.* **15,** 2726 (1977).

[Shenton99] W. Shenton, T. Douglas, M. Young, G. Stubbs, and S. Mann, *Adv. Mater.* **11,** 253 (1999).

[Siuzdak94] G. Siuzdak, *Proc. Natl. Acad. Sci. USA* **91,** 11290 (1994).

[Srikant98] V. Srikant, and D. R. Clarke, *J. Appl. Phys.* **83,** 5447 (1998).

[Storm01] A. J. Storm, J. van Noort, S. de Vries, and C. Dekker, *Appl. Phys. Lett.* **79,** 3881 (2001).

[Sun00] S. Sun, C. B. Murray, D. Weller, L. Folks, and A. Moser, *Science* **287,** 1989 (2000).

[Sverdlov05] Y. Sverdlov, V. Bogush, H. Einati, and Y. Shacham-Diamand, *J. Electrochem. Soc.* **152,** C631 (2005).

[Takano99] H. Takano, J. R. Kenseth, S. Wong, J. C. O'Brien, and M. D. Porter, *Chem. Rev.* **99,** 2845, (1999).

[Tam85] T. M. Tam, *J. Electrochem. Soc.* **132,** 806 (1985).

[Tans97] S. J. Tans, M. H. Devoret, H. Dai, A. Thess, R. E. Smalley, L. J. Geerligs, and C. Dekker, *Nature* **386,** 474 (1997).

[Thomas02] P. J. Tomas, and P. A. Midgley, *Topics in Catal.* **21,** 109 (2002).

[Tosssaint68] C. J. Toussaint, and G. Vos, *J. Appl. Cryst.* **1,** 187 (1968).

[Vega05] R. A. Vega, D. Maspoch, K. Salaita, and C. A. Mirkin, *Angew. Chem. Int. Ed.* **44,** 6013 (2005).

[Verbeeck04] J. Verbeeck, D. V. Dyck, and G. V. Tendeloo, *Spectrochim. Acta Part B* **59,** 1529 (2004).

[Vezenov97] D. V. Vezenov, A. Noy, L. F. Rozsnyai, and C. M. Lieber, *J. Am. Chem. Soc.* **119,** 2006 (1997).

[Weisenhorn89] A. L. Weisenhorn, P. K. Hansma, T. R. Albrecht, and C. F. Quate, *Appl. Phys. Lett.* **54,** 2651, (1989).

[Whaley00] S. R. Whaley, D. S. English, E. L. Hu, P. F. Barbara, and A. M. Belcher, *Nature* **405,** 665 (2000).

[Whitesides91] G. M. Whitesides, J. P. Mathias, and C. T. Seto, *Science* **254,** 1312 (1991).

[Williams96] D. B. Williams, and C. B. Carter, *Transmission Electron Microscopy,* Plenum Press, (New York and London, 1996).

[Wu02] X. C. Wu, A. M. Bittner, and K. Kern, *Langmuir* *18,* 4984 (2002).

[Xia98] Y. Xia, and G. M. Whitesides, *Angew.Chem.Int.Ed*. **37,** 550 (1998).

[Yi05] H. Yi, S. Nisar, S. Y. Lee, M. A. Powers, W. E. Bentley, G. F. Payne, R. Ghodssi, G. W. Rubloff, M. T. Harris, and J. N. Culver, *Nano Lett.* **5,** 1931 (2005).

[Yokoshima00] T. Yokoshima, D. Kaneko, M. Akahori, H. S. Nam, and T. Osaka, *J. Electroanal. Chem.* **491,** 197 (2000).

[Zaitlin00] M. Zaitlin, A. A. B. *Description of Plant Viruses* **8,** 370 (2000).

[Zenhausern92] F. Zenhausern, M. Adrian, R. Emch, M. Taborelli, M. Jobin, and P. Descounts, *Ultramicroscopy* **42-44,** 1168 (1992).

[Zhou02] H. Zhou, H. Alves, D. M. Hofmann, W. Kriegseis, and B. K. Meyer, *Appl. Phys. Lett.* **80,** 210 (2002).

[Zitoun02] D. Zitoun, M. Respaud, M. C. Fromen, and M. J. Casanove, *Phys. Rev. Lett.* **89,** 037203-1 (2002).

List of Publications

Publications related to this thesis are as follows:

(1) A. M. Bittner, X. C. Wu, **S. Balci**, M. Knez, A. Kadri, and K. Kern, ''Bottom-up synthesis and top-down organization of semiconductor and metal clusters on surfaces.'' *Eur. J. Inorg. Chem.*, 3717 (2005).

(2) **S. Balci,** A. M. Bittner, K. Hahn, C. Scheu, M. Knez, A. Kadri, C. Wege, H. Jeske, and K. Kern, ''Copper nanowires within the central channel of tobacco mosaic virus particles.'' *Electrochim. Acta,* (2006) *in print.*

(3) **S. Balci,** K. Noda, A. M. Bittner, S. Sahakalkan, A. Kadri, C. Wege, H. Jeske, and K. Kern, ''Self-assembly of metal-virus-metal structures'' *will be submitted.*

(4) **S. Balci,** D. Leinberger, M. Knez, A. M. Bittner, F. Boes, A. Kadri, C. Wege, H. Jeske, and K. Kern, ''Printing and aligning mesoscale patterns of tobacco mosaic viruses on surfaces.'' *will be submitted.*

(5) **S. Balci,** A. M. Bittner, K. Hahn, A. Kadri, C. Wege, H. Jeske, and K. Kern, ''Virus templated synthesis of CoFe alloy nanowires'' *in preperation.*

(6) **S. Balci,** A. M. Bittner, K. Hahn, A. Kadri, C. Wege, H. Jeske, and K. Kern, ''Electroless deposition of ZnO onto tobacco mosaic virus'' *in preperation.*

Acknowledgements

Curriculum Vitae

Name: Sinan BALCI

Date of Birth: May 15, 1977

Nationality: Republic of Turkey

1996-2000   "Bachelor of Science" studies in chemistry at the Middle East Technical University, Ankara, Turkey.

2000-2002   "Master of Science" studies in chemistry at the Bilkent University, Ankara, Turkey.

2002-2006   PhD student in the group of Prof. Dr. K. Kern at the Max Planck Institute for Solid State Research, Stuttgart, Germany, PhD thesis: "Metal and metaloxide nanostructures on and in plant viruses".